Charles University in Prague
Faculty of Mathematics and Physics

DOCTORAL THESIS

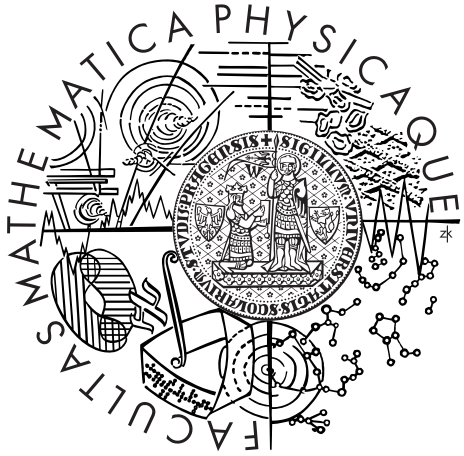

Daniel Božík

Giant monopole resonances in deformed nuclei

Institute of particle and nuclear physics

Supervisor of the doctoral thesis: Jan Kvasil
Study programme: Physics
Specialization: Nuclear physics

Prague 2015

Foremost I would like to thank my supervisor Jan Kvasil for leading my disertation, for his insights and being always available for a discussion. I would also like to thank Valentin Nesterenko from JINR Dubna and his numerous ideas and advices, especially concerning the study of monopole resonances. I also thank Wolfgang Kleinig from JINR Dubna for a lot of technical help with Skyax programs and their implementation and correction for monopole resonances, and Petr Vesely for discussions and help resulting from his experience with the SRPA theory and programs.

I declare that I carried out this doctoral thesis independently, and only with the cited sources, literature and other professional sources.

I understand that my work relates to the rights and obligations under the Act No. 121/2000 Coll., the Copyright Act, as amended, in particular the fact that the Charles University in Prague has the right to conclude a license agreement on the use of this work as a school work pursuant to Section 60 paragraph 1 of the Copyright Act.

In Prague date 14.5.2015 signature of the author

Název práce: Gigantické monopólové rezonance v deformovaných jádrech

Autor: Daniel Božík

Katedra: Ústav částicové a jaderné fyziky

Vedoucí disertační práce: prof. RNDr. Jan Kvasil, DrSc., ÚČJF, MFF UK

Abstrakt: Skúmanie gigantických monopólových rezonancií je dôležité, pretože existuje priama súvislosť medzi nimi a nestlačiteľnosťou jadrovej matérie. Jej význam vzrastá spolu s novými experimentálnymi dátami z experimentov TAMU a RCNP, ktoré sa získali v posledných rokoch. Súčasná práca skúma gigantické monopólové rezonancie v sadách sférických (Pb, Sn, Zr) a deformovaných (Sm, Mo, Cd) jadier. Výpočty boli robené v rámci HFB + SRPA metódy, ktorá bola vyvinutá na MFF UK v spolupráci s JINR v Dubne a Univerzitou v Erlangen. Ako prví sme v rámci mikroskopickej teórie potvrdili double-peak štruktúru GMR silovej funkcie a jej súvislosť s E0-E2 väzbou. Ukázali sme dôležitosť používania silových funkcií pri skúmaní GMR.

Klíčová slova: HFB, SRPA, gigantická monopólová rezonancia

Title: Giant monopole resonances in deformed nuclei

Author: Daniel Božík

Department: Institute of particle and nuclear physics

Supervisor: prof. RNDr. Jan Kvasil, DrSc., ÚČJF, MFF UK

Abstract: The study of giant monopole resonances is important, because of its direct connection to the incompressibility of the nuclear matter, and its importance has risen with new experimental data obtained in recent years from the experiments TAMU and RCNP. The current work brings a study of the giant monopole resonances for chains of spherical (Pb, Sn, Zr) as well as deformed (Sm, Mo, Cd) isotopes. The calculations were carried out within the HFB + SRPA method, which was developed at MFF UK in cooperation with JINR Dubna and the University of Erlangen. We were as first able to confirm, from the microscopic theory, the appearance of a double-peak structure of GMR strength functions for deformed nuclei, and its connection with E0-E2 coupling. We showed the importance of using strength functions in the study of GMR.

Keywords: HFB, SRPA, giant monopole resonances

Contents

Introduction

The subject of this thesis is the theoretical analysis of the giant monopole (E0) resonance in spherical and deformed nuclei using the separable version of the random-phase approximation (SRPA) starting with the Skyrme effective interaction between nucleons. The SRPA method was developed in the IPNP MFF UK in the collaboration with the LTP JINR Dubna and University of Erlangen [1]. This approach involves the solution of the Hartree-Fock equations together with the Bardeen-Cooper-Schrieffer (BCS) equations and in the next step the obtained quasiparticle basis is used for the construction of the separable (factorized) residual interaction. The separable form of the residual interaction is obtained in terms of the multi-dimensional response function method when the nucleus is excited by the set of external single particle operators (fields). The separable residual interaction enables to rewrite the RPA equations into the simple form of the algebraic system equations of very low dimension and in such a way to avoid the construction and diagonalization of huge matrices which is the case in the standard nonseparable RPA. This is important especially for heavier nuclei where the dimensions of the configuration basis are high. The SRPA approach was successfully used in the last decade for the systematic analysis of the giant electric E1 and magnetic M1 dipole resonances (see e.g. [2, 3]) and for the analysis of the toroidal nature of low-lying E1 excitations in nuclei [4, 5]. It should be pointed out that the SRPA method is fully self-consistent, that means the separable residual interaction has not brought any new free model parameters and the only parameters of the approach are those of the effective Skyrme nucleon-nucleon interaction.

The main aim of this work is the systematic analysis of the isoscalar giant monopole resonance (GMR). During last decades the GMR was a subject of intense studies, see e.g. [6, 7] (and citations therein) for recent reviews and discussions. The reason is that the GMR provides a valuable information on the nuclear incompressibility [8, 9] because the energy centroid of the GMR can be directly related to the incompressibility modulus K_A [9] and this modulus belongs to the bulk properties used for the determination of the energy functional (or effective nucleon-nucleon interaction) parameters. For the infinite nuclear matter the commonly accepted value for the incompressibility is $K = 230 - 240$ MeV, confirmed by relativistic as well as non-relativistic mean field models [10]. However, despite many efforts, the description of the GMR still suffers from some persisting problems. For example, the mean field models with $K = 230-240$ MeV reproduce the GMR experimental data in heavy and medium nuclei like ^{208}Pb and ^{144}Sm [11, 12] but fail to describe more recent GMR experiments for lighter nuclei like Sn and Cd isotopes [13, 14, 15, 16, 17], which request a lower incompressibility (see e.g. discussion in [6, 7, 18, 19]. In other words, none of the modern self-consistent models, relativistic or non-relativistic, can simultaneously describe the GMR in all mass regions. This problem has been already analyzed from different sides. It was shown that GMR centroids can be somewhat changed by varying the symmetry energy at constant K [20]. Different Skyrme forces and pairing options (surface, volume and mixed) were inspected [7, 18, 19]. Hartree-Fock-Bogoliubov (HFB) and HF+BCS methods were compared [21]. All these attempts have

partly conformed the description but not solved the problem completely.

The other problem of the GMR is the experimental data themselves. The modern experimental data are mainly delivered by two groups: Texas A&M University (TAMU) [11, 13, 22] and Research Center for Nuclear Physics (RCNP) at Osaka University [12, 14, 15, 16, 17]. Both groups use $(\alpha, \alpha^{'})$ reaction and multipole decomposition prescription to extract the E0 contribution from the cross section. However, these groups provide noticeably different results and this should be also taken into account in the analysis of the above problem [7, 23].

The situation with the GMR in deformed nuclei is even more vague. Though there is an evident progress in experiment studies, e.g. soft Mo [24] and deformed Sm [12, 22] isotopes, the self-consistent mean field+RPA models are yet at very beginning, which is explained by a need to deal with a huge configuration space. So the theoretical results on GMR in deformed nuclei are now mainly reduced to early inconsistent studies based on phenomenological mean field [25, 26, 27]. More than three decades ago, two main deformation effects have been predicted [25, 26, 27] and observed [28, 29] in the GMR: i) broadening the resonance and ii) onset of two-peak structure due to a coupling of the GMR with the $\mu = 0$ branch of the giant quadrupole resonance (GQR). In this thesis these results are revisited by using a modern Skyrme+RPA approach [23].

Another problem and question concerning the comparison of the theoretical results with the experimental data is connected with the fact that this comparison has been performed only with respect to the GMR centroids (see e.g. [7]). In this thesis not only centroids but the whole energy distribution of the E0 strength in the GMR are compared with the experimental data.

All the problems mentioned above and the aspects of the GMR are analyzed in this thesis using the self-consistent BCS+SRPA method. We study the influence of different Skyrme parametrizations (with different incompressibilities K, different isoscalar masses) on the position and (mainly) the shape of the GMR.

The thesis is organized as follows: short introduction into the topic is followed by theoretical introduction, in which we will explain the main features of the Skyrme HF-BCS method and separable RPA. Introduction into giant resonances will be followed by a brief discussion of experimental methods used to determine GMR strengths. In the results section will be presented a methodological study of GMR within HF-BCS+SRPA model intertwined with study of a new SV set of Skyrme functional parametrizations.

1. Theoretical outline

The starting point of our BCS+SRPA approach is the Skyrme effective interaction between nucleons in the nuclear medium. This effective interaction belongs to the family of so called realistic semi-phenomenological effective interactions where the form of these interactions is justified by theoretical consideration but the corresponding expressions involve free parameters. These parameters are usually fixed by fitting the bulk properties (usually bind energy, radius, incompressibility) of selected double-magic nuclei to their experimental values (see e.g. [30]). Besides the Skyrme interaction [31, 32] Gogny interaction [33] and relativistic mean field theory [34] are widely used. During the last decades there were determined many parametrizations for each effective interaction. Each such parametrization had to fit to the above mentioned bulk properties of selected nuclei and besides that, it was fitted to other additional nuclear properties characteristic for a given paper where it was introduced. Therefore, for instance, for the Skyrme effective interaction nowadays we have several tens of parametrizations (see e.g. [35, 36]).

The Skyrme effective interaction was introduced in 1959 [31]. The leading terms of this interaction were obtained as the coordinate representation of the simplest contact non-local potential written in the linear momentum space as follows

$$V(\boldsymbol{p}_i, \boldsymbol{p}_j) = V_0 + V_1(\boldsymbol{p}_i^2 + \boldsymbol{p}_j^2) + V_2 \boldsymbol{p}_i \cdot \boldsymbol{p}_j \tag{1.1}$$

where V_0, V_1 and V_2 are free parameters. We obtain a leading Skyrme interaction term if we transform this interaction into coordinate representation and add a spin dependence through the spin-exchange operator $\hat{P}_\sigma = \frac{1}{2}(1 + \boldsymbol{\sigma}_i \boldsymbol{\sigma}_j)$. In the original papers with the Skyrme interaction (see e.g. [31, 32]) the spin-orbital term and three-body contact interaction (to reproduce nuclear saturation effect) were also added. Later (e.g. [30]) it was shown that a three-body contact interaction can be substituted by a two-body density dependent interaction $V_{dens}(\boldsymbol{r}_i, \boldsymbol{r}_j) = V_4 \delta(\boldsymbol{r}_i - \boldsymbol{r}_j) \rho^\alpha \left(\frac{\boldsymbol{r}_i + \boldsymbol{r}_j}{2}\right)$, where $\rho(\boldsymbol{r})$ is the local density. The modern version of the Skyrme effective interaction in the coordinate representation, used in the RPA calculations is following

$$\begin{aligned}
\mathcal{V}_{ij}^{(Sk)} =& \mathcal{V}_{Sk}(\boldsymbol{r}_i, \boldsymbol{r}_j) = \\
=& t_0 \left(1 + \kappa_0 \hat{P}_\sigma\right) \delta(\boldsymbol{r}_i - \boldsymbol{r}_j) + \frac{1}{2} t_1 \left(1 + \kappa_1 \hat{P}_\sigma\right) \left[\overleftarrow{k'}^2 \delta(\boldsymbol{r}_i - \boldsymbol{r}_j) + \delta(\boldsymbol{r}_i - \boldsymbol{r}_j) \overrightarrow{k}^2\right] + \\
&+ t_2 \left(1 + \kappa_2 \hat{P}_\sigma\right) \overleftarrow{k'} \cdot \delta(\boldsymbol{r}_i - \boldsymbol{r}_j) \overrightarrow{k} + \frac{1}{6} t_3 \left(1 + \kappa_3 \hat{P}_\sigma\right) \delta(\boldsymbol{r}_i - \boldsymbol{r}_j) \rho^\alpha \left(\frac{\boldsymbol{r}_i + \boldsymbol{r}_j}{2}\right) + \\
&+ \mathrm{i} t_4 (\boldsymbol{\sigma}_i + \boldsymbol{\sigma}_j) \cdot \overleftarrow{k'} \times \delta(\boldsymbol{r}_i - \boldsymbol{r}_j) \overrightarrow{k}.
\end{aligned} \tag{1.2}$$

In (1.2) the derivative $\overrightarrow{k} = \frac{\overrightarrow{\nabla}_i - \overrightarrow{\nabla}_j}{2\mathrm{i}}$ acts on the right and $\overleftarrow{k} = -\frac{\overleftarrow{\nabla}_i - \overleftarrow{\nabla}_j}{2\mathrm{i}}$ acts on the left. The constants t_0, t_1, t_2, t_3, t_4, κ_0, κ_1, κ_2, κ_3, α are arbitrary parameters adjusted to reproduce experimental data. The way of their determination will be discussed later. In the coordinate representation the non-locality of the Skyrme interaction is caused by the derivatives $\overrightarrow{k}$ and $\overleftarrow{k'}$. Skyrme interaction (1.2) is always used only in the particle-hole channel. There were attempts in the past

to use it also for the particle-particle channel (see [37]) but it lead to unrealistic pairing properties. Therefore the particle-particle part of the effective interaction is usually added phenomenologically by an additional term, which will be described later.

Instead of using the direct application of the effective interaction (1.2) in the HFB or BCS method, the so-called energy functional methods are applied in the current nuclear physics for the determination of the mean field and the residual interaction.

1.1 Nuclear Energy Density Functional

Energy functional is defined as an expectation value of the total Hamiltonian in the Slater determinant

$$\begin{aligned} E &= \langle \Psi | \hat{H} | \Psi \rangle = \\ &= \int \mathrm{d}^3 r_1 \mathrm{d}^3 r_2 \ldots \mathrm{d}^3 r_A \, \psi^*_{\alpha_1,\alpha_2,\ldots,\alpha_A}(\boldsymbol{r}_1,\ldots,\boldsymbol{r}_A) \, H \psi_{\alpha_1,\alpha_2,\ldots,\alpha_A}(\boldsymbol{r}_1,\ldots,\boldsymbol{r}_A) \end{aligned} \tag{1.3}$$

with Slater determinant in coordinate basis

$$\psi_{\alpha_1,\alpha_2,\ldots,\alpha_A}(\boldsymbol{r}_1,\ldots,\boldsymbol{r}_A) = \langle \boldsymbol{r}_1 \ldots \boldsymbol{r}_A | \Psi \rangle = \frac{1}{\sqrt{A!}} \det \begin{bmatrix} \phi_{\alpha_1}(\boldsymbol{r}_1) & \phi_{\alpha_2}(\boldsymbol{r}_1) & \cdots & \phi_{\alpha_A}(\boldsymbol{r}_1) \\ \vdots & & & \vdots \\ \vdots & & & \vdots \\ \phi_{\alpha_1}(\boldsymbol{r}_A) & \phi_{\alpha_2}(\boldsymbol{r}_A) & \cdots & \phi_{\alpha_A}(\boldsymbol{r}_A) \end{bmatrix} \tag{1.4}$$

where $\phi_{\alpha_i}(\boldsymbol{r})$ are single-particle wave functions.

In (1.3) $\hat{H}$ is the total Hamiltonian

$$\hat{H} = \hat{T} + \hat{V} \tag{1.5}$$

where $\hat{T}$ is a kinetic energy operator and $\hat{V}$ is an interaction operator. If the interaction operator $\hat{V}$ depends only on the coordinates of individual nucleons (i.e., it does not depend on spins of nucleons or on the derivatives of their coordinates), the functional (1.3) is dependent only on the local density $\rho(\boldsymbol{r})$ and the Hartree-Fock single-particle basis can be obtained using the Hohenberg-Kohn theorem [38] by minimizing the $E[\rho]$ with respect to the local density $\rho(\boldsymbol{r})$ (using the local density approximation one usually obtains Kohn-Sham equation (see [39]) which is in the case of the contact interaction equivalent to the HF equation).

Since the Skyrme interaction (1.2) depends on the Pauli spin matrices and on the derivatives of the coordinates, it is obvious that the final Skyrme energy functional is not a simple function of the local density $\rho(\boldsymbol{r})$, but it also depends on its derivatives and on the densities of the spin variables.

In order to construct the full Skyrme energy functional we introduce a set of non-local densities

$$\begin{aligned} \text{Density} \qquad & \rho(\boldsymbol{r},\boldsymbol{r'}) = \sum_{\sigma} \langle \Psi | a^{\dagger}_{\boldsymbol{r'}\sigma} a_{\boldsymbol{r}\sigma} | \Psi \rangle \\ \text{Spin-density} \qquad & \boldsymbol{s}(\boldsymbol{r},\boldsymbol{r'}) = \sum_{\sigma\sigma'} \langle \Psi | a^{\dagger}_{\boldsymbol{r'}\sigma'} a_{\boldsymbol{r}\sigma} | \Psi \rangle \langle \sigma' | \hat{\boldsymbol{\sigma}} | \sigma \rangle \end{aligned} \tag{1.6}$$

where $a^{\dagger}_{\boldsymbol{r}\sigma}$, $a_{\boldsymbol{r}\sigma}$ are creation and annihilation operators of a nucleon in the space coordinate $\boldsymbol{r}$, with the spin projection σ. The remaining non-local densities are defined as derivatives of the densities (1.6)

$$\begin{aligned} \text{Kinetic density} \qquad & \tau(\boldsymbol{r},\boldsymbol{r'}) = \boldsymbol{\nabla} \cdot \boldsymbol{\nabla'} \rho(\boldsymbol{r},\boldsymbol{r'}) \\ \text{Spin-kinetic density} \qquad & \boldsymbol{T}(\boldsymbol{r},\boldsymbol{r'}) = \boldsymbol{\nabla} \cdot \boldsymbol{\nabla'} \boldsymbol{s}(\boldsymbol{r},\boldsymbol{r'}) \\ \text{Current density} \qquad & \boldsymbol{j}(\boldsymbol{r},\boldsymbol{r'}) = \frac{1}{2\mathrm{i}} \left(\boldsymbol{\nabla} - \boldsymbol{\nabla'} \right) \rho(\boldsymbol{r},\boldsymbol{r'}) \\ \text{Tensor density} \qquad & J_{ij}(\boldsymbol{r},\boldsymbol{r'}) = \frac{1}{2\mathrm{i}} \left(\nabla_i - \nabla'_i \right) s_j(\boldsymbol{r},\boldsymbol{r'}) \end{aligned} \tag{1.7}$$

where the derivative $\boldsymbol{\nabla}$ acts on $\boldsymbol{r}$ and the derivative $\boldsymbol{\nabla'}$ acts on $\boldsymbol{r'}$. The corresponding local densities are then

$$\rho(\boldsymbol{r}) = \rho(\boldsymbol{r},\boldsymbol{r'})|_{\boldsymbol{r}=\boldsymbol{r'}} = \rho(\boldsymbol{r},\boldsymbol{r}) \tag{1.8}$$

and accordingly for other densities.

For the subsequent considerations it is important to determine the symmetries of all the densities above with respect to the time-reversion. Since the space coordinates do not change and the spin and momentum operators do change sign with respect to the inversion of time, we can easily find the symmetries given in the Table 1.1.

J	$T^{-1}JT$	time-even/odd
ρ	+	even
s	-	odd
τ	+	even
T	-	odd
j	-	odd
J	+	even

Table 1.1: Time-reversion symmetries of the Skyrme densities

The energy functional of the total Hamiltonian

$$\hat{H} = \hat{T} + \hat{V}_{Sk} + \hat{V}_{Coul} + \hat{V}_{pair} \tag{1.9}$$

consists of the kinetic energy, Skyrme interaction, Coulomb interaction among protons and the pairing term

$$E = E_{kin} + E_{Sk} + E_{Coul} + E_{pair} \tag{1.10}$$

The kinetic term of the energy functional is

$$E_{kin} = \langle\Psi| \sum_{i=1}^{A} \left(-\frac{\hbar^2}{2m}\Delta_i \right) |\Psi\rangle = \frac{\hbar^2}{2m} \int \mathrm{d}^3 r\, \tau(\boldsymbol{r}) \tag{1.11}$$

the Coulomb interaction gives

$$E_{Coul} = \frac{e^2}{2} \int \mathrm{d}^3 r \mathrm{d}^3 r' \, \frac{\rho_p(\boldsymbol{r})\rho_p(\boldsymbol{r'})}{|\boldsymbol{r} - \boldsymbol{r'}|} - \frac{3}{4}\left(\frac{3}{\pi}\right)^{1/2} e^2 \int \mathrm{d}^3 r\, \rho_p^{4/3}(\boldsymbol{r}) \tag{1.12}$$

where $\rho_p(\boldsymbol{r})$ is the proton local density. The derivation of the Skyrme part is described in the paper of Vautherin and Brink [32] so we give only the final expression

$$\begin{aligned}
E_{Sk} &= \langle\Psi| \sum_{i<j} \mathcal{V}_{ij}^{(Sk)} |\Psi\rangle = \\
&= \frac{1}{2} \int \mathrm{d}^3 r_1 \mathrm{d}^3 r_2 \, \rho(\boldsymbol{r_1}) \mathcal{V}_{Sk}(\boldsymbol{r}_1, \boldsymbol{r}_2) \rho(\boldsymbol{r_2}) - \frac{1}{2} \int \mathrm{d}^3 r_1 \mathrm{d}^3 r_2 \, \rho(\boldsymbol{r_2}, \boldsymbol{r_1}) \mathcal{V}_{Sk}(\boldsymbol{r}_1, \boldsymbol{r}_2) \rho(\boldsymbol{r_1}, \boldsymbol{r_2}) \approx \\
&\approx \int \mathrm{d}^3 r \left(\frac{1}{2} t_0 \left[\left(1 + \frac{1}{2}\kappa_0 \right) \rho^2 - \left(\kappa_0 + \frac{1}{2} \right) \sum_{q=n,p} \rho_q^2 \right] + \frac{1}{2} t_0 \left[\frac{1}{2}\kappa_0 \boldsymbol{s}^2 - \frac{1}{2} \sum_{q=n,p} \boldsymbol{s}_q^2 \right] - \right. \\
&- \frac{1}{16} t_1 \left(1 + \frac{1}{2}\kappa_1 \right) \left[3\rho\Delta\rho - 4(\rho\tau - \boldsymbol{j}^2) \right] + \frac{1}{16} t_1 \left(\frac{1}{2} + \kappa_1 \right) \sum_{q=n,p} \left[3\rho_q \Delta\rho_q - 4(\rho_q \tau_q - j_q^2) \right] - \\
&- \frac{1}{16} t_1 \kappa_1 \left[\frac{3}{2} \boldsymbol{s} \Delta \boldsymbol{s} - 2 \left(\boldsymbol{s} \cdot \boldsymbol{T} - \boldsymbol{J}^2 \right) \right] + \frac{1}{16} t_1 \sum_{q=n,p} \left[\frac{3}{2} \boldsymbol{s}_q \Delta \boldsymbol{s}_q - 2 \left(\boldsymbol{s}_q \cdot \boldsymbol{T}_q - \boldsymbol{J}_q^2 \right) \right] + \\
&+ \frac{1}{16} t_2 \left(1 + \frac{1}{2}\kappa_2 \right) \left[\rho\Delta\rho + 4(\rho\tau - \boldsymbol{j}^2) \right] + \frac{1}{16} t_2 \left(\frac{1}{2} + \kappa_2 \right) \sum_{q=n,p} \left[\rho_q \Delta\rho_q - 4 \left(\rho_q \tau_q - j_q^2 \right) \right] + \\
&+ \frac{1}{16} t_2 \kappa_2 \left[\frac{1}{2} \boldsymbol{s} \cdot \Delta \boldsymbol{s} + 2 \left(\boldsymbol{s} \cdot \boldsymbol{T} - \boldsymbol{J}^2 \right) \right] + \frac{1}{16} t_2 \sum_{q=n,p} \left[\frac{1}{2} \boldsymbol{s}_q \cdot \Delta \boldsymbol{s}_q + 2 \left(\boldsymbol{s}_q \cdot \boldsymbol{T}_q - \boldsymbol{J}_q^2 \right) \right] + \\
&+ \frac{1}{12} t_3 \left[\left(1 + \frac{1}{2}\kappa_3 \right) \rho^2 - \left(\kappa_3 + \frac{1}{2} \right) \sum_{q=n,p} \rho_q^2 \right] \rho^\alpha + \frac{1}{12} t_3 \left[\frac{1}{2}\kappa_3 \boldsymbol{s}^2 - \frac{1}{2} \sum_{q=n,p} \boldsymbol{s}_q^2 \right] \rho^\alpha - \\
&\left. - \frac{1}{12} t_4 \left[(\nabla \times \boldsymbol{j}) \cdot \boldsymbol{s} + \rho \nabla \cdot \boldsymbol{J} \right] - \frac{1}{12} t_4 \sum_{q=n,p} \left[(\nabla \times \boldsymbol{j}_q) \cdot \boldsymbol{s}_q + \rho_q \nabla \cdot \boldsymbol{J}_q \right] \right).
\end{aligned} \tag{1.13}$$

The densities without the lower index q denote the total nuclear density, e.g.

$$\rho(\boldsymbol{r}) = \rho_p(\boldsymbol{r}) + \rho_n(\boldsymbol{r}) \tag{1.14}$$

In the equation (1.13) we also introduced the following notations for the tensor density

$$\boldsymbol{J}^2(\boldsymbol{r}) = \sum_{ij} J_{ij}(\boldsymbol{r}) J_{ij}(\boldsymbol{r})$$
$$\boldsymbol{\nabla} \cdot \boldsymbol{J}(\boldsymbol{r}) = \sum_{ijk} \epsilon_{ijk} \nabla_i J_{jk}(\boldsymbol{r}) \tag{1.15}$$

The last part of the energy functional (1.10) is the pairing functional E_{pair} which comes from the particle-particle channel. As we have already mentioned, the particle-particle channel has to be treated separately of the Skyrme interaction (which acts in the particle-hole channel). Therefore we have to introduce also the pairing part of the functional E_{pair} independently of the Skyrme part E_{Sk}. Firstly we introduce the pairing density

$$\kappa(\boldsymbol{r}) = \sum_{i \in occ} \langle \Psi | a_i^\dagger a_{\bar{i}}^\dagger | \Psi \rangle = \sum_{i \in occ} \phi_i(\boldsymbol{r}) \phi_{\bar{i}}(\boldsymbol{r}) \tag{1.16}$$

The index i goes through all occupied states and $\bar{i}$ denotes the time-reversion of the state i. The pairing potential is then introduced as following (see e.g. [35])

$$E_{pair} = \frac{1}{4} \sum_{g=n,p} V_g^{(pair)} \int \mathrm{d}^3 r \, \kappa_g^2(\boldsymbol{r}) \tag{1.17}$$

This energy corresponds to the particle-particle channel of the zero-range (delta) interaction. The constants V_q are fitted to the nuclear pairing properties (experimental values of the pairing gap energies) uniquely for each parametrization of the set t_0, t_1, t_2, t_3, t_4, κ_0, κ_1, κ_2, κ_3, α.

The expressions (1.11), (1.12), (1.13), (1.17) determine the total energy functional (1.10) - $E(\rho, \tau, \boldsymbol{s}, \boldsymbol{j}, \boldsymbol{J}, \boldsymbol{T}, \kappa)$ as a functional of the densities ρ, τ, $\boldsymbol{s}$, $\boldsymbol{j}$, $\boldsymbol{J}$, $\boldsymbol{T}$ and κ and from these expressions we can see that the total Skyrme energy functional can be written as the spatial integral of the energy density $\mathcal{H}(\boldsymbol{r})$:

$$E(\rho, \tau, \boldsymbol{s}, \boldsymbol{j}, \boldsymbol{J}, \boldsymbol{T}, \kappa) = \int \mathrm{d}^3 r \, \mathcal{H}(\rho, \tau, \boldsymbol{s}, \boldsymbol{j}, \boldsymbol{J}, \boldsymbol{T}, \kappa) \tag{1.18}$$

1.2 HF and BCS

The HF (or HF+BCS) single-particle basis, which is a set of eigen-states of the hamiltonian $\hat{h}$ (mean field Hamiltionian), can be obtained by searching for the minimum of the energy functional E (see (1.3), (1.18)) with respect to the variations of the single-particle function $\phi_i(\boldsymbol{r})$. This variational principle can be expressed as following

$$\delta \left(E - \sum_i e_i \sum_{\sigma \pm 1} \phi_i^*(\boldsymbol{r}, \sigma) \phi_i(\boldsymbol{r}, \sigma) \right) = 0 \tag{1.19}$$

where E is the energy functional (1.18) and the second term in (1.19) represents the additional normalization condition of the single-particle wave functions. In (1.19) we add the index $\sigma = \pm 1$ for a single-particle spin projection variable.

It is known that the Lagrange multiplier e_i represents the single-particle energy corresponding to the single-particle state i. In our case the energy functional (1.18) depends on the single-particle wave functions $\phi_i(\boldsymbol{r},\sigma)$ through the densities $J_\alpha(\boldsymbol{r}) = \rho,\, \tau,\, \boldsymbol{s},\, \boldsymbol{j},\, \boldsymbol{T},\, \kappa$ (index α enumerates these densities).

Variational principle (1.19) yields the following HF equations

$$\begin{aligned}\sum_\alpha \frac{\partial \mathcal{H}(\boldsymbol{r})}{\partial J_\alpha(\boldsymbol{r})}\frac{\partial J_\alpha(\boldsymbol{r})}{\partial \phi_i(\boldsymbol{r},\sigma)} &= e_i \phi_i^*(\boldsymbol{r},\sigma)\\ \sum_\alpha \frac{\partial \mathcal{H}(\boldsymbol{r})}{\partial J_\alpha(\boldsymbol{r})}\frac{\partial J_\alpha(\boldsymbol{r})}{\partial \phi_i^*(\boldsymbol{r},\sigma)} &= e_i \phi_i(\boldsymbol{r},\sigma)\end{aligned} \tag{1.20}$$

or

$$\langle i|\hat{h}_{HF}|j\rangle = e_i \delta_{ij}$$

with

$$\hat{h}_{HF} = \int \mathrm{d}^3 r \sum_\alpha \left(\frac{\partial}{\partial J_\alpha(\boldsymbol{r})}\int \mathrm{d}^3 r'\, \mathcal{H}(\boldsymbol{r'})\right)\hat{J}_\alpha(\boldsymbol{r}) \tag{1.21}$$

where $\hat{J}_\alpha(\boldsymbol{r})$ for different α are the corresponding density operators:

$$\begin{aligned}\hat{\rho}(\boldsymbol{r}) &= \sum_{ij} \phi_i^\dagger(\boldsymbol{r})\phi_j(\boldsymbol{r}) a_i^\dagger a_j\\ \hat{\tau}(\boldsymbol{r}) &= \sum_{ij} \left(\boldsymbol{\nabla}\phi_i^\dagger(\boldsymbol{r})\right)\cdot\left(\boldsymbol{\nabla}\phi_j(\boldsymbol{r})\right) a_i^\dagger a_j\\ \hat{\boldsymbol{J}}(\boldsymbol{r}) &= -\frac{\mathrm{i}}{2}\sum_{ij}\left[\phi_i^\dagger(\boldsymbol{r})\left(\boldsymbol{\nabla}\times\boldsymbol{\sigma}\right)\phi_j(\boldsymbol{r}) - \left(\left(\boldsymbol{\nabla}\times\boldsymbol{\sigma}\right)\phi_i^\dagger(\boldsymbol{r})\phi_j(\boldsymbol{r})\right)\right] a_i^\dagger a_j\\ \hat{\boldsymbol{j}}(\boldsymbol{r}) &= \frac{\mathrm{i}}{2}\sum_{ij}\left[\left(\boldsymbol{\nabla}\phi_i^\dagger(\boldsymbol{r})\right)\phi_j(\boldsymbol{r}) - \phi_i^\dagger(\boldsymbol{r})\left(\boldsymbol{\nabla}\phi_j(\boldsymbol{r})\right)\right] a_i^\dagger a_j\\ \hat{\boldsymbol{s}}(\boldsymbol{r}) &= \sum_{ij}\phi_i^\dagger(\boldsymbol{r})\hat{\boldsymbol{\sigma}}\phi_j(\boldsymbol{r}) a_i^\dagger a_j\\ \hat{\boldsymbol{T}}(\boldsymbol{r}) &= \sum_{ij}\left(\boldsymbol{\nabla}\phi_i^\dagger(\boldsymbol{r})\right)\boldsymbol{\sigma}\cdot\left(\boldsymbol{\nabla}\phi_j(\boldsymbol{r})\right) a_i^\dagger a_j\end{aligned} \tag{1.22}$$

expressed in terms of the single-particle creation and annihilation operators $a_i^\dagger$, a_i.

The substitution of (1.22) and (1.18) into (1.21) gives the HF equations in the following form

$$\int \mathrm{d}^3 r \sum_{q=n,p}\left(U_q(\boldsymbol{r})\hat{\rho}_q(\boldsymbol{r}) + B_q(\boldsymbol{r})\hat{\tau}_q(\boldsymbol{r}) + \boldsymbol{W}_q(\boldsymbol{r})\cdot\hat{\boldsymbol{J}}_q(\boldsymbol{r})\right)|i\rangle = e_i|i\rangle \tag{1.23}$$

with the Dirac ket notation $\phi_i(\boldsymbol{r}) = \langle \boldsymbol{r}|i\rangle$, where

$$\begin{aligned} U_q(\boldsymbol{r}) =& b_0\rho(\boldsymbol{r}) - b'_0\rho_q(\boldsymbol{r}) + b_1\tau(\boldsymbol{r}) - b'_1\tau_q(\boldsymbol{r}) - b_2\Delta\rho(\boldsymbol{r}) + b'_2\Delta\rho_q(\boldsymbol{r}) + \\ &+ b_3\frac{\alpha+2}{2}\rho^{\alpha+1}(\boldsymbol{r}) - \frac{2}{3}b'_3\rho^{\alpha}(\boldsymbol{r})\rho_q(\boldsymbol{r}) - \frac{\alpha}{3}b'_3\rho^{\alpha-1}(\boldsymbol{r})\sum_{q'=n,p}\rho^2_{q'}(\boldsymbol{r}) - \\ &- b_4\boldsymbol{\nabla}\cdot\boldsymbol{J}(\boldsymbol{r}) - b'_4\boldsymbol{\nabla}\cdot\boldsymbol{J}_q(\boldsymbol{r}) + e^2\delta_{qp}\left[\int \mathrm{d}^3r'\,\frac{\rho_q(\boldsymbol{r})}{|\boldsymbol{r}-\boldsymbol{r'}|} - \left(\frac{3}{\pi}\right)^{1/3}\rho_q^{1/3}(\boldsymbol{r})\right], \end{aligned} \tag{1.24}$$

$$B_q(\boldsymbol{r}) = \frac{\hbar^2}{2m} + b_1\rho(\boldsymbol{r}) - b'_1\rho_q(\boldsymbol{r}), \tag{1.25}$$

$$\boldsymbol{W}_q(\boldsymbol{r}) = b_4\boldsymbol{\nabla}\rho(\boldsymbol{r}) + b'_4\boldsymbol{\nabla}\rho_q(\boldsymbol{r}) - \tilde{b}_4\boldsymbol{J}(\boldsymbol{r}) - \tilde{b}'_4\boldsymbol{J}_q(\boldsymbol{r}) \tag{1.26}$$

Where we introduced a new set of Skyrme parameters, which are related to the previous set of parameters t_0, t_1, t_2, t_3, t_4, κ_0, κ_1, κ_2, κ_3, α by the following relations:

$$\begin{aligned} b_0 &= t_0\left(1+\frac{1}{2}x_0\right) & \tilde{b}_0 &= \frac{1}{2}t_0x_0 \\ b'_0 &= t_0\left(\frac{1}{2}+x_0\right) & \tilde{b}'_0 &= \frac{1}{2}t_0 \\ b_1 &= \frac{1}{4}\left[t_1\left(1+\frac{1}{2}x_1\right)+t_2\left(1+\frac{1}{2}x_2\right)\right] & \tilde{b}_2 &= \frac{1}{8}\left[\frac{3}{2}t_1x_1-\frac{1}{2}t_2x_2\right] \\ b'_1 &= \frac{1}{4}\left[t_1\left(\frac{1}{2}+x_1\right)-t_2\left(\frac{1}{2}+x_2\right)\right] & \tilde{b}'_2 &= \frac{1}{8}\left[\frac{3}{2}t_1+\frac{1}{2}t_2\right] \\ b_2 &= \frac{1}{8}\left[3t_1\left(1+\frac{1}{2}x_1\right)-t_2\left(1+\frac{1}{2}x_2\right)\right] & \tilde{b}_3 &= \frac{1}{8}t_3x_3 \\ b'_2 &= \frac{1}{8}\left[3t_1\left(\frac{1}{2}+x_1\right)+t_2\left(\frac{1}{2}+x_2\right)\right] & \tilde{b}'_3 &= \frac{1}{8}t_3 \\ b_3 &= \frac{1}{4}t_3\left(1+\frac{1}{2}x_3\right) & \tilde{b}_4 &= \frac{1}{8}(t_1x_1+t_2x_2) \\ b'_3 &= \frac{1}{4}t_3\left(\frac{1}{2}+x_3\right) & \tilde{b}'_4 &= -\frac{1}{8}(t_1-t_2) \\ b_4 &= \frac{1}{2}t_4 & b'_4 &= \frac{1}{2}t_4. \end{aligned} \tag{1.27}$$

We can see that the time-odd densities do not contribute to the HF equation (1.23), which is consistent with the fact that the single-particle mean field Hamiltonian is time-even.

In the derivation of the expression (1.23) we did not treat the pairing correlations. Since in this work we study mainly the axially deformed open-shell nuclei, in which the pairing correlations are important, we should take them into account. As was already mentioned, within the Skyrme functional we treat the particle-hole and the particle-particle parts of the interaction independently. This enables us to solve the HF equations (1.23) first and then in the second step

to use the standard BCS method with the pairing interaction corresponding to (1.17). Actually to take into account the pairing part of the energy functional we used the modified BCS method. The modification consists in the fact that in the each iteration during solving the HF equation the BCS equations are also solved. After this iteration process we obtain the BCS solution: the single-particle states and energies as well as the Bogoliubov amplitudes U_i and V_i, the Fermi energies μ_q and the corresponding gap energies Δ_i

$$U_i^2 = \frac{1}{2}\left[1 + \frac{e_i - \mu}{\left((e_i-\mu)^2 + \Delta_i^2\right)^{1/2}}\right] \quad V_i^2 = \frac{1}{2}\left[1 - \frac{e_i - \mu}{\left((e_i-\mu)^2 + \Delta_i^2\right)^{1/2}}\right] \tag{1.28}$$

$$\Delta_i = -\frac{1}{4}\sum_j \frac{V_{\bar{i}i\bar{j}j}}{\left((e_i-\mu)^2 + \Delta_i^2\right)^{1/2}} \tag{1.29}$$

with the quasiparticle creation and annihilation operators given by Bogoliubov transformation

$$\begin{aligned} \alpha_i^\dagger &= U_i\, a_i^\dagger + V_i a_{\bar{i}} \\ \alpha_i &= U_i\, a_i + V_i a_{\bar{i}}^\dagger \end{aligned} \tag{1.30}$$

In the quasiparticle formalism the BCS mean field Hamiltonian has the diagonal form (see e.g. [30])

$$\hat{h}_{BCS} = \langle BCS|\hat{H}|BCS\rangle + \sum_{\nu>0} E_\nu \left(\alpha_\nu^\dagger \alpha_\nu + \alpha_{\bar{\nu}}^\dagger \alpha_{\bar{\nu}}\right) \tag{1.31}$$

where $E_\nu = \sqrt{(e_i-\mu)^2 + \Delta_i^2}$ is the quasiparticle energy.

Since most of the isotopes studied in this work are deformed, it should be explained, what is meant by "nuclear deformation". From the point of view of the microscopic models there is no such thing as a sharp edge of the nucleus. However, in the models based on the density functional techniques (e.g. Skyrme Hartree-Fock), we can introduce the equipotential surfaces of the static mean field, and the nuclear deformation means the deformation of these equipotential surfaces. A general surface can be expressed in the form of Dirichlet decomposition

$$R(\theta,\phi) = R_0\left(1 + \sum_{l=1}^{\infty}\sum_{m=-l}^{+l} \alpha_{lm} Y_{lm}(\theta,\phi)\right) \tag{1.32}$$

where $R(\theta,\phi)$ is the distance between the origin of the coordinate system (center of mass of the nucleus) and the point on the mean field equipotential surface in the direction given by angles θ, ϕ in spherical coordinates. In (1.32) $Y_{lm}(\theta,\phi)$ are the spherical harmonics, R_0 is the mean radius and the α_{lm} are the deformation parameters. In this work we focus only on the nuclei axially quadrupole deformed (or rather we look at them as if they were deformed only axially), which means $\alpha_{20} = \beta \neq 0$ and all other α_{lm} ($l \geq 0$) are zero[1]. This quadrupole deformation parameter β is unambiguously connected with the mass quadrupole moment

[1]It is possible to prove that all α_{1m} values are zero because they are related to the translations of the nucleus as a whole. The parameter α_{00} specifies the compressibility of the nucleus but since it is possible to include it in the value of the mean radius R_0, we do not discuss it in more detail.

$\langle BCS|\hat{M}_{20}|BCS\rangle$ ($\hat{M}_{20} \equiv \sum_{i=1}^{A} r_i^2 Y_{20}(\hat{r}_i)$).

Since there is a problem in solving the HF selfconsistent equations (1.23) if the solution has different symmetry from the initial single particle basis (see e.g. [30]), instead of the standard HF variational principle (1.19), we use the so called constrained HF method. This method is based on the fact that in addition to the normalization condition (second term in (1.19)) we also use a constraint which requires that in each step the quadrupole moment $\langle BCS|\hat{M}_{20}|BCS\rangle$ is given a fixed value Q_0. That means that instead of (1.19) we use the constrained HF condition

$$\delta\left(E - \sum_i e_i \sum_{\sigma\pm 1} \phi_i^*(\boldsymbol{r},\sigma)\phi_i(\boldsymbol{r},\sigma) - C\left(\langle BCS|\hat{M}_{20}|BCS\rangle - Q_0\right)\right) = 0 \quad (1.33)$$

where C is a constant, a value of which is given by a requirement to fulfill the condition $Q_0 = \langle BCS|\hat{M}_{20}|BCS\rangle$ (given by the deformation parameter β) during the iteration process. In practice we find the deformation of the nucleus by solving the HF equation (1.33) on a grid of β parameter values in some interval $\beta \in < \beta_{min}, \beta_{max} >$ and the equilibrium deformation corresponds to the minimum of the total energy $E = \langle BCS|\hat{H}|BCS\rangle$ in this grid.

As we mentioned above, nowadays there are many Skyrme interaction parametrizations (see e.g. [35]). Corresponding parameters were obtained by fitting the global properties of selected nuclei to experimental data. Usually these properties are: binding energy per nucleon, compressibility of the nuclear matter, nuclear radii. This fitting was practically always performed for doubly magic spherical nuclei. During the last two decades the original parametrizations were (see [35]) modified many times in order to describe a concrete nuclear property (with subsequent refitting to global properties of double-magic nuclei). In this way we have today a lot of parametrizations describing the global characteristics of double magic nuclei approximately on the same level. One of the tasks of current nuclear physics is to find the parametrization of Skyrme (or Gogny or relativistic mean field) interaction (or a parametrization of the corresponding energy functional) which is able to describe a broad variety of nuclear properties (not only the bulk properties of double-magic nuclei). The greatest deal of nuclear properties is, however, connected with the residual interaction and in order to describe these properties we have to go beyond the mean field. In the next section we discuss random phase approximation (RPA) and time dependent Hartree-Fock approach as two examples of methods going beyond the mean field.

1.3 Random phase approximation

The method, which is mostly used for the description of the excited states of the nucleons, is the random phase approximation (see e.g. [30]). It is the method intended to go beyond the mean field approximation and to include into calculations residual interaction. If we have a mean field, i.e., a single particle states and corresponding energies: $a_i^\dagger$ and ϵ_i, we can construct an ansatz for the full hamiltonian simply as

$$|\nu\rangle = \left(\sum_{mi} c_{mi}^{(\nu)} a_m^\dagger a_i + \sum_{mnij} c_{minj}^{(\nu)} a_m^\dagger a_i a_n^\dagger a_j + \dots \right) |BCS\rangle, \tag{1.34}$$

that is, all one-particle, two-particle, etc., excitations of the mean-field ground state. In the notation of [30] indices denote: m, n - states over Fermi level, and i, j - states below Fermi level. This should cover whole Hilbert space of the problem, and solving Schroedinger equation with residual interaction and the ansatz (1.34) would yield the spectrum of full Hamiltonian. This problem is, however, unsolvable. We can consider the first approximation, where we take only one-particle excitations. This is called the Tamm-Dancoff approximation (TDA) and its main drawback is, that it does not make correlations of the ground state. This problem is solved within the RPA method. The RPA method involves approximatively the correlations in the ground state. Its ansatz is a linear combination of the particle-hole creation as well as annihilation operator

$$|\nu\rangle = \sum_{mi} \left(\psi_{mi}^{(\nu)} a_m^\dagger a_i - \phi_{mi}^{(\nu)} a_i^\dagger a_m \right) |RPA\rangle \tag{1.35}$$

where $a_m^\dagger$ and a_i are single-quasiparticle creation and annihilation operators, solutions of the HF problem. $|\nu\rangle$ form an RPA spectrum, with an RPA ground state $|RPA\rangle$ which will be defined later. In the case when the pairing correlations are taken into account and quasiparticle creation and annihilation operators are introduced then the expression (1.35) can be equivalently written as

$$|\nu\rangle = \sum_{q=n,p} \sum_{\overline{\omega}} \left(\psi_{\overline{\omega}}^{(\nu,q)} \hat{b}_{\overline{\omega}}^\dagger - \phi_{\overline{\omega}}^{(\nu,q)} \hat{b}_{\overline{\omega}} \right) |RPA\rangle \tag{1.36}$$

where $b_{ij}^\dagger$, $b_{\overline{ij}}^\dagger$, $b_{i\overline{j}}^\dagger$ are two-quasiparticle quasi-boson operators

$$b_{ij}^\dagger = \alpha_i^\dagger \alpha_j^\dagger \qquad b_{\overline{ij}}^\dagger = \alpha_{\overline{i}}^\dagger \alpha_{\overline{j}}^\dagger \qquad b_{i\overline{j}}^\dagger = \alpha_i \alpha_{\overline{j}}^\dagger \tag{1.37}$$

In the quasi-boson approximation they fulfill the commutation relations

$$\begin{aligned} \langle RPA| \left[b_{ij}, b_{i'j'}^\dagger \right] |RPA\rangle &\approx \delta_{ii'}\delta_{jj'} - \delta_{ij'}\delta_{ji'} \\ \langle RPA| \left[b_{\overline{ij}}, b_{\overline{i'j'}}^\dagger \right] |RPA\rangle &\approx \delta_{ii'}\delta_{jj'} - \delta_{ij'}\delta_{ji'} \\ \langle RPA| \left[b_{i\overline{j}}, b_{i'\overline{j'}}^\dagger \right] |RPA\rangle &\approx \delta_{ii'}\delta_{jj'} \end{aligned} \tag{1.38}$$

which are the same, as would be in the BCS ground state $|BCS\rangle$.

For the RPA state $|\nu\rangle$ we can define the so-called phonon operator (which creates the lowest excitations)

$$\hat{O}_\nu^\dagger = \sum_{q=n,p} \sum_{\overline{\omega}} \left(\psi_{\overline{\omega}}^{(\nu,q)} \hat{b}_{\overline{\omega}}^\dagger - \phi_{\overline{\omega}}^{(\nu,q)} \hat{b}_{\overline{\omega}} \right) \tag{1.39}$$

with

$$\hat{O}_\nu^\dagger |RPA\rangle = |\nu\rangle \qquad \hat{H}|\nu\rangle = \hbar\omega_\nu |\nu\rangle \tag{1.40}$$

and $\hat{O}_\nu|RPA\rangle = 0$ for $\forall\nu$, which defines the RPA ground state. The RPA equations of motion are given by the oscillator approximation

$$\left[\hat{H}, \hat{O}^\dagger_\nu\right] |RPA\rangle = \hbar\omega_\nu \hat{O}^\dagger_\nu |RPA\rangle \tag{1.41}$$

where we set the energy of the RPA ground state for convenience equal to 0. Now we multiply this equation by arbitrary bra, in the form $\langle RPA|\delta\hat{O}$. This yields equation (due to the properties of annihilation operators on the RPA ground state)

$$\langle RPA| \left[\delta\hat{O}, \left[\hat{H}, \hat{O}^\dagger_\nu\right]\right] |RPA\rangle = \hbar\omega_\nu \langle RPA| \left[\delta\hat{O}, \hat{O}^\dagger_\nu\right] |RPA\rangle \tag{1.42}$$

Finally from the equation (1.42) and its complex conjugate with the right choice of the operator $\delta\hat{O}$ we get the RPA equations

$$\left[\hat{H}, \hat{O}^\dagger_\nu\right] = \hbar\omega_\nu \hat{O}^\dagger_\nu; \qquad \left[\hat{H}, \hat{O}_\nu\right] = -\hbar\omega_\nu \hat{O}_\nu; \qquad \left[\hat{O}_\nu, \hat{O}^\dagger_{\nu'}\right] = \delta_{\nu\nu'} \tag{1.43}$$

The phonon amplitudes $\psi^{(\nu,q)}_{\varpi}$, $\phi^{(\nu,q)}_{\varpi}$ and phonon energies $\hbar\omega_\nu$ can be found from the RPA equation (1.43) where $\hat{H}$ is the total Hamiltonian (in our case (1.9)). These RPA equations can be transformed (see [30]) into the diagonalization of large matrices, whose dimensions are given by the number of two-quasiparticle states involved in the configuration space. However, this number is huge for heavier nuclei, mainly if we wish to calculate RPA spectra for deformed nuclei. Hence the standard RPA approach is rarely used for heavier deformed nuclei. Therefore in the IPNP MFF UK (in collaboration with University of Erlangen and JINR Dubna) the so-called separable random phase approximation (SRPA) was developed. The brief description of this method follows .

1.4 Separable RPA

We start with the response theory ansatz. This assumes that the excitations of the nucleus can be produced by the action of a set of external hermitian single particle operators $(\hat{Q}_k,\ \hat{P}_k)$ $(k = 1, \ldots, N)$ where

$$\begin{array}{lll} \hat{Q}^\dagger_k = \hat{Q}_k & \hat{T}^{-1}\hat{Q}_k\hat{T} = \hat{Q} & \hat{P}^\dagger_k = \hat{P}_k \\ \hat{P}_k = \mathrm{i}\left[\hat{H}, \hat{Q}_k\right] & \hat{T}^{-1}\hat{P}_k\hat{T} = -\hat{P} & \hat{Q}_k = \mathrm{i}\left[\hat{H}, \hat{P}_k\right] \end{array} \tag{1.44}$$

where $\hat{T}$ is the time-reverse transformation. As a result of the action of these exciting operators $(\hat{Q}_k,\ \hat{P}_k)$, the system (nucleus) vibrates around its ground state $|BCS\rangle$.

Vibrations of the nucleus, caused by the external modes (1.44), are described by the time-dependent BCS vacuum $|BCS(t)\rangle$ which is related to the equilibrium BCS vacuum $|BCS\rangle$ (see (1.31)) by the time-dependent shift transformation (see e.g. [40]):

$$|BCS(t)\rangle = \prod_{q=n,p}\prod_{k=1}^{N} \mathrm{e}^{-\mathrm{i}(q_{kq}(t)-\langle q_{kq}\rangle)\hat{Q}_{kq}}\mathrm{e}^{-\mathrm{i}p_{kq}(t)\hat{P}_{kq}}|BCS\rangle \tag{1.45}$$

where $q_{k\tau}(t) - \langle q_{k\tau}\rangle$ and $p_{k\tau}(t)$ are periodical vibration amplitudes

$$\begin{aligned} q_{kq}(t) - \langle q_{kq}\rangle &= \langle BCS(t)|\hat{Q}_{kq}|BCS(t)\rangle - \langle BCS|\hat{Q}_{kq}|BCS\rangle = \\ &= \overline{q}_{kq}\cos\omega t \\ p_{kq}(t) &= \langle BCS(t)|\hat{P}_{kq}|BCS(t)\rangle = \overline{p}_{kq}\sin\omega t \end{aligned} \tag{1.46}$$

The SRPA supposes vibrations with small amplitudes. Therefore we can use the Taylor expansion of (1.45) up to the linear order in amplitudes $q_{kq}(t) - \langle q_{kq}\rangle$, $p_{kq}(t)$, and we obtain for time-dependent densities and currents $J_\tau^{(\alpha)}(\boldsymbol{r},t)$ (see (1.22)) the following expressions

$$\begin{aligned} J_q^{(\alpha)}(\boldsymbol{r},t) &= \langle BCS|\hat{J}^\alpha(\boldsymbol{r})|BCS\rangle + \delta J_q^{(\alpha)}(\boldsymbol{r},t) = \\ &= J_q^{(\alpha)}(\boldsymbol{r}) + \delta J_q^{(\alpha)}(\boldsymbol{r},t) \end{aligned} \tag{1.47}$$

with

$$\begin{aligned} \delta J_q^{(\alpha)}(\boldsymbol{r},t) &= \langle BCS(t)|\hat{J}_q^{(\alpha)}(\boldsymbol{r})|BCS(t)\rangle - \langle BCS|\hat{J}_q^{(\alpha)}(\boldsymbol{r})|BCS\rangle \approx \\ &\approx -\mathrm{i}\sum_{qk}\Big((q_{kq}(t) - \langle q_{kq}\rangle)\langle BCS|\left[\hat{P}_{kq}, \hat{J}_q^{(\alpha)}(\boldsymbol{r})\right]|BCS\rangle + \\ &\quad + p_{kq}(t)\langle BCS|\left[\hat{Q}_{kq}, \hat{J}_q^{(\alpha)}(\boldsymbol{r})\right]|BCS\rangle\Big) \end{aligned} \tag{1.48}$$

Similarly for the time-dependent (vibrating) BCS mean field (see (1.21)) up to the linear order in $q_{kq}(t) - \langle q_{k\tau}\rangle$, $p_{kq}(t)$ we have

$$\begin{aligned} \delta\hat{h}_{BCS}(\boldsymbol{r},t) &= \sum_{\alpha',q'}\frac{\partial\hat{h}_{BCS}(\boldsymbol{r})}{\partial J_{q'}^{(\alpha')}(\boldsymbol{r}')}\delta J_{q'}^{(\alpha')}(\boldsymbol{r}',t) = \\ &= \int \mathrm{d}^3r' \sum_{\substack{\alpha q \\ \alpha' q'}}\left[\frac{\partial^2\mathcal{E}}{\partial J_q^{(\alpha)}(\boldsymbol{r})\partial J_{q'}^{(\alpha')}(\boldsymbol{r}')}\right]\delta J_{q'}^{(\alpha')}(\boldsymbol{r}',t)\hat{J}_q^{(\alpha)}(\boldsymbol{r}) = \\ &= \sum_{qk}\Big((q_{kq}(t) - \langle q_{kq}\rangle)\hat{X}_{kq}(\boldsymbol{r}) + p_{kq}(t)\hat{Y}_{kq}(\boldsymbol{r})\Big) \\ \delta\hat{H}_{BCS}(t) &= \int \mathrm{d}^3r\,\delta\hat{h}_{BCS}(\boldsymbol{r},t) \end{aligned} \tag{1.49}$$

where we introduced following operators

$$\hat{X}_{kq}(\boldsymbol{r}) = \sum_{q'} \hat{X}^{q'}_{kq}(\boldsymbol{r}) =$$

$$= \mathrm{i} \int \mathrm{d}^3 r' \sum_{\substack{\alpha_+,\alpha'_+ \\ q'}} \left[\frac{\partial^2 \mathcal{E}}{\partial J^{(\alpha_+)}_q(\boldsymbol{r}) \partial J^{(\alpha'_+)}_{q'}(\vec{r}')} \right] \langle BCS| \left[\hat{P}_{kq'}, \hat{J}^{(\alpha'_+)}_{q'}(\boldsymbol{r}') \right] |BCS\rangle \hat{J}^{(\alpha_+)}_q(\boldsymbol{r})$$

$$\hat{Y}_{kq}(\boldsymbol{r}) = \sum_{q'} \hat{Y}^{q'}_{kq}(\boldsymbol{r}) =$$

$$= \mathrm{i} \int \mathrm{d}^3 r' \sum_{\substack{\alpha_-,\alpha'_- \\ q'}} \left[\frac{\partial^2 \mathcal{E}}{\partial J^{(\alpha_-)}_q(\boldsymbol{r}) \partial J^{(\alpha'_-)}_{q'}(\boldsymbol{r}')} \right] \langle BCS| \left[\hat{Q}_{kq'}, \hat{J}^{(\alpha'_-)}_{q'}(\vec{r}') \right] |BCS\rangle \hat{J}^{(\alpha_-)}_q(\boldsymbol{r}) \tag{1.50}$$

where α_+ enumerates T-even densities ($\hat{T}^{-1}\hat{J}^{(\alpha_+)}\hat{T} = \hat{J}^{(\alpha_+)}$) and α_- enumerates T-odd densities ($\hat{T}^{-1}\hat{J}^{(\alpha_-)}\hat{T} = -\hat{J}^{(\alpha_-)}$). Finally we gain

$$\begin{aligned} \hat{X}_{kq} &= \int \mathrm{d}^3 r\, \hat{X}_{kq}(\boldsymbol{r}) & \hat{T}^{-1}\hat{X}_{kq}\hat{T} &= \hat{X}_{kq} \\ \hat{Y}_{kq} &= \int \mathrm{d}^3 r\, \hat{Y}_{kq}(\boldsymbol{r}) & \hat{T}^{-1}\hat{Y}_{kq}\hat{T} &= -\hat{Y}_{kq} \end{aligned} \tag{1.51}$$

For time-dependent variations of operators $\hat{X}_{kq}$ and $\hat{Y}_{kq}$ we have (similarly as in (1.48) for $\delta J^{(\alpha)}_q(\boldsymbol{r}, t)$)

$$\begin{aligned} \langle \delta \hat{X}_{kq}(t) \rangle &= \langle BCS(t)|\hat{X}_{kq}|BCS(t)\rangle - \langle BCS|\hat{X}_{kq}|BCS\rangle = \\ &= \sum_{k'q'} (q_{k'q'}(t) - \langle q_{kq}\rangle) \kappa^{-1}_{kq,k'q'} \\ \langle \delta \hat{Y}_{kq}(t) \rangle &= \langle BCS(t)|\hat{Y}_{kq}|BCS(t)\rangle - \langle BCS|\hat{Y}_{kq}|BCS\rangle = \\ &= \sum_{k'q'} p_{k'q'}(t) \eta^{-1}_{kq,k'q'} \end{aligned} \tag{1.52}$$

where we introduced the so-called strength matrices $\kappa^{-1}_{kq,k'q'}$ and $\eta^{-1}_{kq,k'q'}$

$$\kappa^{-1}_{kq,k'q'} = \kappa^{-1}_{k'q',kq} \equiv \mathrm{i}\langle BCS| \left[\hat{P}_{k'q'}, \hat{X}_{kq}\right] |BCS\rangle =$$
$$= \int \mathrm{d}^3r \int \mathrm{d}^3r' \sum_{\alpha_+\alpha'_+} \langle BCS| \left[\hat{P}_{kq}, \hat{J}^{(\alpha_+)}_q(\boldsymbol{r})\right] |BCS\rangle \left[\frac{\partial^2 \mathcal{E}}{\partial J^{(\alpha_+)}_q(\boldsymbol{r}) \partial J^{(\alpha'_+)}_{q'}(\boldsymbol{r}')}\right]$$
$$\langle BCS| \left[\hat{P}_{k'q'}, \hat{J}^{(\alpha'_+)}_{q'}(\boldsymbol{r}')\right] |BCS\rangle$$
$$\eta^{-1}_{kq,k'q'} = \eta^{-1}_{k'q',kq} \equiv \mathrm{i}\langle BCS| \left[\hat{Q}_{k'q'}, \hat{P}_{kq}\right] |BCS\rangle =$$
$$= \int \mathrm{d}^3r \int \mathrm{d}^3r' \sum_{\alpha_-\alpha'_-} \langle BCS| \left[\hat{Q}_{kq}, \hat{J}^{(\alpha_-)}_q(\boldsymbol{r})\right] |BCS\rangle \left[\frac{\partial^2 \mathcal{E}}{\partial J^{(\alpha_-)}_q(\boldsymbol{r}) \partial J^{(\alpha'_-)}_{q'}(\boldsymbol{r}')}\right]$$
$$\langle BCS| \left[\hat{Q}_{k'q'}, \hat{J}^{(\alpha'_-)}_{q'}(\boldsymbol{r}')\right] |BCS\rangle \tag{1.53}$$

For the determination of the vibration amplitudes $\overline{q}_{kq}$ and $\overline{p}_{kq}$ (see (1.46)) and corresponding vibration frequencies ω we use the time-dependent-Hartree-Fock-Bogoliubov (TDHFB) method starting from the Thouless theorem for the vibrating $|HFB(t)\rangle$ (or in our case $|BCS(t)\rangle$) vacuum:

$$|BCS(t)\rangle_\nu = \mathrm{e}^{\sum\limits_{\overline{\omega}=ij,\overline{ij},i\overline{j}} c^{(\nu)}_{\overline{\omega}}(t) b^\dagger_{\overline{\omega}}} |BCS\rangle \approx \left(1 + \sum_{\overline{\omega}=ij,\overline{ij},i\overline{j}} c^{(\nu)}_{\overline{\omega}}(t) b^\dagger_{\overline{\omega}}\right) |BCS\rangle \tag{1.54}$$

where

$$c^{(\nu)}_{\overline{\omega}}(t) = c^{(\nu)+}_{\overline{\omega}} \mathrm{e}^{\mathrm{i}\omega_\nu t} + c^{(\nu)-}_{\overline{\omega}} \mathrm{e}^{-\mathrm{i}\omega_\nu t}$$

and where $b^\dagger_{ij}$, $b^\dagger_{\overline{ij}}$, $b^\dagger_{i\overline{j}}$ are two-quasiparticle quasi-boson operators (see (1.37))

Using TDHFB equation

$$\mathrm{i}\hbar \frac{\mathrm{d}}{\mathrm{d}t} |BCS(t)\rangle_\nu = \left[\hat{h}_{BCS} + \delta\hat{h}_{BCS}(t)\right] |BCS(t)\rangle_\nu \tag{1.55}$$

we express amplitudes $c^\pm_{\overline{\omega}}$ in terms of $\overline{q}_{kq}$ and $\overline{p}_{kq}$ and then, substituting into (1.54) we determine ${}_\nu\langle BCS|\delta\hat{X}_{kq}|BCS\rangle_\nu$ and ${}_\nu\langle BCS|\delta\hat{Y}_{kq}|BCS\rangle_\nu$. By comparison of these expectation values with the previous ones (see (1.52)) we finally obtain the system of equations for unknown amplitudes $\overline{q}_{kq}$, $\overline{p}_{kq}$:

$$\sum_{q'k'} \left[\overline{q}^{(\nu)}_{k'q'} \left[F^{(XX)}_{k'q',kq} - \kappa^{-1}_{k'q',kq}\right] + \overline{p}^{(\nu)}_{k'q'} F^{(XY)}_{k'q',kq}\right] = 0$$
$$\sum_{q'k'} \left[\overline{q}^{(\nu)}_{k'q'} F^{(YX)}_{k'q',kq} + \overline{p}^{(\nu)}_{k'q'} \left[F^{(YY)}_{k'q',kq} - \eta^{-1}_{k'q',kq}\right]\right] = 0 \tag{1.56}$$

where we introduced following matrices

$$F^{(AA)}_{kq,k'q'}(\hbar\omega) = \sum_{\overline{q}} \sum_{\substack{\overline{\omega}\in\overline{q} \\ \overline{\omega}=ij,i\overline{j},\overline{ij}}} \frac{\varepsilon_{\overline{\omega}}\langle\overline{\omega}|\hat{A}^{\overline{q}}_{k'q'}|\rangle\langle\overline{\omega}|\hat{A}^{\overline{q}}_{kq}|\rangle}{\varepsilon^2_{\overline{\omega}} - \hbar^2\omega^2}$$
$$F^{(AB)}_{k'q',kq}(\hbar\omega) = F^{(BA)}_{kq,k'q'}(\hbar\omega) = \sum_{\overline{q}=n,p} \sum_{\substack{\overline{\omega}\in\overline{q} \\ \overline{\omega}=ij,i\overline{j},\overline{ij}}} \frac{\hbar\omega\langle\overline{\omega}|\hat{A}^{\overline{q}}_{k'q'}|\rangle\langle\overline{\omega}|\hat{B}^{\overline{q}}_{kq}|\rangle}{\varepsilon^2_{\overline{\omega}} - \hbar^2\omega^2} \tag{1.57}$$

where $\hat{A}$, $\hat{B} = \hat{X}_{kq}$ or $\hat{Y}_{kq}$. In (1.57) $\langle\overline{\omega}|\hat{A}_{k\tau}|\rangle$ ($\overline{\omega} = ij, i\overline{j}, \overline{ij}$) are two-quasiparticle matrix elements of given operator $\hat{A}$, and $\varepsilon_{\overline{\omega}}$ are two-quasiparticle energies:

$$\varepsilon_{\overline{\omega}} = \begin{cases} E_i + E_j & \text{for } \overline{\omega} = ij \\ E_i + E_{\overline{j}} & \text{for } \overline{\omega} = i\overline{j} \\ E_{\overline{i}} + E_{\overline{j}} & \text{for } \overline{\omega} = \overline{ij} \end{cases} \tag{1.58}$$

It should be noted that the matrix of the equation system (1.56) is hermitian (real and symmetric). The dimension of the equation system (1.56) is $4N$ where N is the number of excited fields $(\hat{Q}_k, \hat{P}_k)$ $(k = 1, \ldots, N)$ - see (1.44). The index ν in (1.56) enumerates all solutions of the equation system (1.56). The condition of solvability of the equation system (1.56) is that the determinant of its matrix is zero

$$\det F(\omega_\nu) = 0 \tag{1.59}$$

where F is the matrix of the system (1.56). Equation (1.59) gives energies $\hbar\omega_\nu$ of all TDHFB solutions.

It can be shown that the equation system (1.56) for unknown $\overline{q}^{(\nu)}_{k\tau}$ and $\overline{p}^{(\nu)}_{k\tau}$ is the same as the one obtained from the standard static RPA equations (1.43) if we take the RPA Hamiltonian in the form

$$\hat{H}_{RPA} = \hat{h}_{BCS} + \hat{V}^{(SRPA)}_{res} \tag{1.60}$$

where $\hat{h}_{BCS}$ is the BCS mean field (1.21) and $\hat{V}^{(SRPA)}_{res}$ is the separable residual RPA interaction

$$\hat{V}^{(SRPA)}_{res} = \sum_{kq} \sum_{\substack{k'q' \\ k,k'=1,\ldots,N}} \left(\kappa_{kq,k'q'} \hat{X}^{(1)}_{kq} \hat{X}^{(1)}_{k'q'} + \eta_{kq,k'q'} \hat{Y}^{(1)}_{kq} \hat{Y}^{(1)}_{k'q'} \right) \tag{1.61}$$

where $\hat{X}^{(1)}_{kq}$, $\hat{Y}^{(1)}_{kq}$ is a two-quasiparticle part of the corresponding operators $\hat{X}_{kq}$ and $\hat{Y}_{kq}$ (parts involving only $\alpha^\dagger\alpha^\dagger$ and $\alpha\alpha$ terms in their quasiparticle representation expressions).

Two-quasiparticle amplitudes $\psi^{(\nu,q)}_{\overline{\omega}}$ and $\phi^{(\nu,q)}_{\overline{\omega}}$ (see (1.39)) in the phonon creation operator $\hat{Q}^\dagger_\nu$ (see (1.39)) are related to the solutions $\overline{q}_{kq}$ and $\overline{p}_{kq}$ in the TDHFB equation system (1.56) by following relations

$$\psi_{\overline{\omega}}^{(\nu,q)} = 4\xi_{\overline{\omega}} \frac{\sum\limits_{q'k'} \overline{q}_{k'q'}^{(\nu)} \langle \overline{\omega}|\hat{X}_{k'q'}^{q}|\rangle - \mathrm{i} \sum\limits_{q'k'} \overline{p}_{k'q'}^{(\nu)} \langle \overline{\omega}|\hat{Y}_{k'q'}^{q}|\rangle}{\varepsilon_{\overline{\omega}} - \hbar\omega_{\nu}}$$
$$\varphi_{\overline{\omega}}^{(\nu,q)} = 4\xi_{\overline{\omega}} \frac{\sum\limits_{q'k'} \overline{q}_{k'q'}^{(\nu)} \langle \overline{\omega}|\hat{X}_{k'q'}^{q}|\rangle + \mathrm{i} \sum\limits_{q'k'} \overline{p}_{k'q'}^{(\nu)} \langle \overline{\omega}|\hat{Y}_{k'q'}^{q}|\rangle}{\varepsilon_{\overline{\omega}} + \hbar\omega} \tag{1.62}$$

where

$$\xi_{\overline{\omega}} = \begin{cases} \frac{1}{4} & \text{for } \overline{\omega} = ij \\ \frac{1}{4} & \text{for } \overline{\omega} = \overline{ij} \\ \frac{1}{2} & \text{for } \overline{\omega} = i\overline{j} \end{cases} \tag{1.63}$$

So, practical recipe for the description of nuclear excitations in the framework of our HF-BCS + SRPA approach is following

- At first we solve the HF variational problem (1.33) self-consistently with BCS problem (1.28). As a result we obtain HF single-particle basis (i.e. single-particle states $|i\rangle = a_i^{\dagger}|\rangle$ with corresponding single-particle energies e_i) with the corresponding occupation quasiparticle amplitudes U_i and V_i and quasiparticle energies E_i (see (1.28)).

- In the next step we choose the exciting modes ($\hat{Q}_k,\ \hat{P}_k$)$(k = 1, \ldots, N)$ adequately to the type and multipolarity of the investigated excitations.

- Then we construct the matrix F of the RPA system of equations (1.56) and by solving this equation system we obtain the unknown $\overline{q}_{(\nu)}^{kq}$, $\overline{p}_{(\nu)}^{kq}$ with corresponding phonon energies $\hbar\omega_{\nu}$. The structure, that means amplitudes $\psi_{\overline{\omega}}^{(\nu,q)}$ and $\varphi_{\overline{\omega}}^{(\nu,q)}$ (see (1.39)), of each one-phonon state $|\nu\rangle \equiv \hat{O}_{\nu}^{\dagger}|RPA\rangle$ is then given by (1.62).

It should be pointed out here that the SRPA phonons obtained by solving the equation system (1.56) with (1.59) and (1.62) should be the same as the solution of the standard RPA equations if the appropriate choice of the set of exciting field $(\hat{Q}_k,\ \hat{P}_k)$ $(k = 1, \ldots, N)$ is used. Not good choice of these operators can cause that some of the standard RPA solutions is not obtained by the SRPA approach, or more precisely, some of the standard RPA solutions are not sufficiently excited to be seen in the excitation transition of given type and multipolarity described by the SRPA.

1.5 Strength function

For the transitions (corresponding to the electromagnetic transition operators $M_{\lambda\mu}^{(Z)}$ of the type Z ($Z = el$, mag) of the nucleus from ground state to the excited states $|\nu\rangle$ we define energy weighted strength function:

$$S_k(Z\lambda\mu; E) = \sum_\nu B(Z\lambda\mu;\, |RPA\rangle \to |\nu\rangle)(\hbar\omega_\nu)^k \delta(E - \hbar\omega_\nu)$$
$$= \sum_\nu (\hbar\omega_\nu)^k \left|\langle\nu|\hat{M}^{(Z)}_{\lambda\mu}|RPA\rangle\right|^2 \delta(\hbar\omega_\nu - E). \tag{1.64}$$

In the framework of the RPA the strength function $S_k(Z\lambda\mu;\, E)$ can be further modified using $|\nu\rangle = Q^\dagger_\nu|RPA\rangle$ and $Q_\nu|RPA\rangle = 0$ as follows

$$\begin{aligned} S_k(E) &= \sum_\nu (\hbar\omega_\nu)^k \left|\langle RPA|[\hat{Q}_\nu, \hat{M}]|RPA\rangle\right|^2 \delta(\hbar\omega_\nu - E) \\ &\approx \sum_\nu (\hbar\omega_\nu)^k \left|\langle BCS|[\hat{Q}_\nu, \hat{M}]|BCS\rangle\right|^2 \delta(\hbar\omega_\nu - E) \end{aligned} \tag{1.65}$$

The reason why the strength functions $S_k(E)$ are introduced is the fact that we are often interested in the energy distribution of the transition probability instead of the probability of transitions into particular RPA states. Particularly this is the case of higher excitation energies where the density of states is very high (e.g., giant resonance energy region). The density of states is so big that individual states cannot be experimentally distinguished in any way.

In order to do the comparison with experimental excitation probabilities which are usually energetically smeared by the finite experimental resolution the strength functions (1.65), (1.64) are also "smeared" by the substitution of the delta function by the averaging Lorentz function

$$\xi_\Delta(E - \hbar\omega_\nu) = \frac{1}{\pi}\frac{\Delta/2}{(E - \hbar\omega_\nu)^2 + (\Delta/2)^2}, \tag{1.66}$$

where Δ is the energy averaging interval and the normalization of the Lorentz function is chosen so that

$$\lim_{\Delta\to 0}\frac{1}{\pi}\frac{\Delta/2}{(E - \hbar\omega_\nu)^2 + (\Delta/2)^2} = \delta(\hbar\omega_\nu - E) \tag{1.67}$$

which preserves the integral properties of the strength function.

Such averaging was found to be optimal for the comparison with experiments and a simulation of broadening effects beyond the RPA, namely, escape widths (escape to the continuum) and coupling with complex configuration (two- and more phonon components in the wave functions). The square of the transition matrix elements, $\langle BCS|[\hat{Q}_\nu,\ \hat{M}^{(Z)}_{\lambda\mu}]BCS\rangle$ in (1.65) can be further expressed in terms of the phonon energy $\hbar\omega_\nu$ and two-quasiparticle matrix elements of the operators $\hat{X}^{q'}_{kq}$ and $\hat{Y}^{q'}_{kq}$ as follows (see e.g. [41])

$$\left|\langle RPA|\left[\hat{Q}^\dagger_\nu, \hat{M}^{(Z,\,(1))}_{\lambda\mu}\right]|RPA\rangle\right|^2 = \left|\sum_{kq}\left[\overline{q}^{(\nu)}_{kq} A^{(X)(\lambda\mu)}_{kq;\omega_\nu} + \overline{p}^{(\nu)}_{kq} A^{(Y)(\lambda\mu)}_{kq;\omega_\nu}\right]\right|^2 \tag{1.68}$$

where $\hat{M}^{(X,\,(1))}_{\lambda\mu}$ is the two-quasiparticle part of the transition operator responsible for a given transition of the type Z with the multipolarity λ and the projection μ. In (1.68) we introduced the following symbols:

$$A^{(X)(Z\lambda\mu)}_{kq;\omega_\nu} \equiv 2 \sum_{q'=n,p} \sum_{\substack{\overline{\omega}\in q' \\ \overline{\omega}=ij,\overline{ij},i\overline{j}}} \frac{g_1 \langle\overline{\omega}|\hat{X}^{q'}_{kq}|\rangle \langle\overline{\omega}|\hat{M}^{(Z)}_{\lambda\mu}|\rangle}{\varepsilon^2_{\overline{\omega}} - \hbar^2\omega^2_\nu}$$
$$A^{(Y)(Z\lambda\mu)}_{kq;\omega_\nu} \equiv 2 \sum_{q'=n,p} \sum_{\substack{\overline{\omega}\in q' \\ \overline{\omega}=ij,\overline{ij},i\overline{j}}} \frac{g_2 \langle\overline{\omega}|\hat{Y}^{q'}_{kq}|\rangle \langle\overline{\omega}|\hat{M}^{(Z)}_{\lambda\mu}|\rangle}{\varepsilon^2_{\overline{\omega}} - \hbar^2\omega^2_\nu} \tag{1.69}$$

where $g_1 = \varepsilon_{\overline{\omega}}$, $g_2 = \hbar\omega_\nu$ if $\hat{M}^{(Z)}_{\lambda\mu}$ is the electric transition operator ($Z = el$) and $g_1 = \hbar\omega_\nu$, $g_2 = \varepsilon_{\overline{\omega}}$ if $\hat{M}^{(Z)}_{\lambda\mu}$ is the magnetic transition operator ($Z = mag$). Reduced transition probability (1.68) can be further rewritten as follows (see [42, 41])

$$B(M\lambda\mu;\, |RPA\rangle \to |\nu\rangle) = \left[\sum_{kq}\sum_{k'q'} A^{(Z)\,\dagger}_{kq}(\omega_\nu) F_{kq,k'q'} A^{(Z)}_{k'q'}(\omega_\nu)\right] \left[\frac{\partial}{\partial\omega} \det F\right]^{-1}_{\omega=\omega_\nu} \tag{1.70}$$

where

$$A^{(Z)}_{kq}(\omega) \equiv \begin{pmatrix} A^{(X)(Z\lambda\mu)}_{kq;\omega} \\ \\ A^{(Y)(Z\lambda\mu)}_{kq;\omega} \end{pmatrix}$$
$$F_{kq,k'q'} \equiv \begin{pmatrix} F^{(XX)}_{kq,k'q'} & F^{(XX)}_{kq,k'q'} \\ \\ F^{(YX)}_{kq,k'q'} & F^{(XX)}_{kq,k'q'} \end{pmatrix} \tag{1.71}$$

The expression (1.68) is connected with the probability of the transition to the one particular RPA one-phonon state $|\nu\rangle$. In this thesis we are interested in giant resonances and, as it was mentioned above, giant resonances are formed by thousands of RPA states. Based on the mathematical Cauchy theorem in the paper [41] the method was developed which enables us to determine the strength function $S_k(Z\lambda\mu; E)$ without solving the SRPA equations for each individual state $|\nu\rangle$. The final expression for the strength function for electromagnetic excitation of the type $Z = el$, mag and multipolarity λ with its projection μ reads

$$S_k(Z\lambda\mu; E) = \mathrm{Im}\left[\frac{z^k \sum_{kq}\sum_{k'q'} A^{(Z)\,\dagger}_{kq}(z) F_{kq,k'q'}(z) A^{(Z)}_{k'q'}(z)}{\pi \det F(z)}\right]_{z=E+\mathrm{i}\frac{\Delta}{2}} +$$
$$+ \frac{\Delta}{\pi} \sum_{\substack{\overline{\omega} \\ \overline{\omega}=ij,\overline{ij},i\overline{j}}} \varepsilon^k_{\overline{\omega}} \left|\langle\overline{\omega}|\hat{M}_{Z\lambda\mu}|\rangle\right|^2 \left(\frac{1}{(E-\varepsilon_{\overline{\omega}})^2 + \left(\frac{\Delta}{2}\right)^2} - \frac{1}{(E+\varepsilon_{\overline{\omega}})^2 + \left(\frac{\Delta}{2}\right)^2}\right) \tag{1.72}$$

where the first term is a contribution coming from the residual interaction and the second term is the contribution from the quasiparticle mean field.

For further statistical analysis of the strength functions $S_k(Z\lambda\mu;\ E)$ the moments of these are introduced. The moment $m_k(Z\lambda\mu)$ is defined as the integral of the energy weighted strength function $S_k(Z\lambda\mu;\ E)$ over the whole energy interval (see e.g. [43])

$$m_k(Z\lambda\mu) = \int_0^\infty dE\ S_k(Z\lambda\mu;\ E) \tag{1.73}$$

These moments are known in the literature as so called sum rules. Knowledge of an infinite set of such moments determines, in principle, the strength function $S_0(Z\lambda\mu; E)$. However, this possibility is limited by the convergence of the moment expansion (see [44]). In practice it is is possible to calculate only a few moments. A method for the determination of $S_0(E)$ based on moments m_k is practically useful only when a few moments are able to characterize the whole strength function (e.g. if a resonant phenomena is presented). Using moments (1.73) it is possible to define a set of energies

$$E_{k,\,k-2} \equiv \sqrt{\frac{m_k}{m_{k-2}}} \quad \text{or} \quad E_{k,\,k-1} \equiv \frac{m_k}{m_{k-1}} \tag{1.74}$$

which characterize the energy distribution of $S_0(E)$. If this distribution is sharply peaked at a certain energy then all energies $E_{k,\,k-2}$ and $E_{k,\,k-1}$ coincide. The degree to which they are different reflects the width of the distribution.

The expression (1.73) with $k = 1$ for the general single-particle transition operator $\hat{M}$ and for the general system of the eigen states $|\nu\rangle$ of the Hamiltonian $\hat{H}$ can be also rewritten as (see (1.64))

$$\begin{aligned} m_1(\hat{M}) &= \int_0^\infty dE\ \sum_\nu (E - E_0)\ \left|\langle\nu|\ \hat{M}\ |0\rangle\right|^2 \delta(E - E_\nu) \\ &= \frac{1}{2}\ \langle 0|\ \left[\hat{M},\ [\hat{H},\ \hat{M}]\right]\ |0\rangle \end{aligned} \tag{1.75}$$

where $|0\rangle$ is the ground state, $\hat{H}\ |0\rangle = E_0\ |0\rangle$. It can be shown (see e.g. [43]) that in the case, when the local single-particle operator $\hat{M}$ commutes with the interaction part of the Hamiltonian, the l.h.s. of (1.75) is model independent. That means, for instance, that (1.75) does not change if the expectation value of the double commutator in the l.h.s. of (1.75) is calculated in the $|BCS\rangle$ or $|RPA\rangle$ vacuum.

In the case of the strength functions of electromagnetic transition reduced probabilities $S_0(Z\lambda\mu;\ E)$ the so called giant resonances are observed for E0, E1, E2, M1, ... transitions, which are characterized by a broad peak in the corresponding energy intervals (e.g. in the case of isoscalar GMR this interval is 10-20 MeV for all nuclei). The centroids of these resonances can be estimated by energies $E_{k,\,k-2}$ or $E_{k,\,k-1}$. Usually energies $E_{1,0}$, $E_{1,-1}$, $E_{3,1}$ are used for this purpose. For instance, the analysis and discussion of the GMR performed recently in the paper [7] was based only on the centroid defined as

$$E_{ISGMR} = \frac{m_1(E0)}{m_0(E0)} \tag{1.76}$$

However, as it was already mentioned, it is not sufficient for the relevant analysis of the whole distribution of the E0 strength in the GMR.

2. Giant monopole resonances

2.1 Theoretical description of the GMR in nuclei

This thesis is devoted to the analyses of the GMR in spherical and deformed nuclei. Particular attention is given to the shape of the GMR because this feature of the GMR has not been investigated theoretically up to now. Practically all theoretical analyses of the GMR in the past concerned only the centroids of the monopole resonance which were determined by (1.76) (see e.g. [7, 18, 19, 20]). The theoretical investigation of the GMR in deformed nuclei using self-consistent models has not been performed at all. Therefore in our papers [45, 23, 46] the nowadays GMR data are analyzed using the self-consistent Skyrme+SRPA approach discussed in the previous section. This approach allows to study the shape of giant resonances in the both spherical and axially deformed nuclei.

The GMR, which represents the energy distribution of the isoscalar excitation reduced probability, can be visualized from macroscopic point of view as a radial vibration of the nucleus surface (so called collective breathing mode). Microscopically it is connected with the E0 transition operator $\sum r_i^2 Y_{00}$. The interest of theoretical nuclear physics in the GMR is connected not only with the demand of theoretical interpretation of new experimental data on GMR but mainly with the fact that the GMR is closely related to the incompressibility of the infinite nuclear matter which is one of the basic bulk nuclear properties used fot the determination of parameters of the effective nucleon-nucleon interaction in the nuclear medium. Based on the simple assumption that the GMR in the spherical nuclei can be approximated by one harmonic oscillator radial collective state in the paper [47, 9] the simple direct relationship between the incompressibility modulus K_A of a finite nucleus with a mass A and the energy centroid E_{ISGMR}:

$$E_{cent} = \sqrt{\frac{\hbar^2 K_A}{m \langle r^2 \rangle}}. \tag{2.1}$$

where m is the nucleon mass and $\langle r^2 \rangle$ the mean square radius of the nucleus. This expression allows us to extract the incompressibility K_A of a finite nucleus if we know the GMR centroid energy E_{ISGMR} (from experimental data on the GMR). Systematic study of the incompressibility K_A enables to obtain the incompressibility modulus K_∞ for the infinite nuclear matter which is one of the bulk nuclear quantities used for the fitting of the effective nucleon-nucleon interaction parameters. This can be done, for instance, from the liquid-drop model Weizsäcker-like formula for nuclear incompressibility [9, 19]

$$K_A = K_V + K_S A^{-1/3} + (K_\tau + K_{S,\tau} A^{-1/3}) \frac{(N-Z)^2}{A^2} + K_C \frac{Z^2}{A^{4/3}} \tag{2.2}$$

with volume, surface, symmetry, symmetry-surface and coulomb terms, respectively, where the volume term can be naturally identified with the infinite nuclear matter incompressibility $K_V \approx K_\infty$. So, knowing the finite nucleus incompressibility K_A we can obtain from (2.2) (e.g. by the least square fitting)

the value of $K_\infty = K_V$. This can be done either for K_A determined before from the experimental data on the GMR or for K_A obtained from the analysis of the theoretical GMR centroids (determined by (1.76) and (1.75) or directly from the shape of the theoretical GMR energy distribution).

For the determination of the effective nucleon-nucleon interaction parameters usually the experimental value of the modulus K_∞ is compared with the theoretical one calculated on the level of the mean field using directly the definition of the K_∞ (see e.g. [9])

$$K_\infty = k_F^2 \, \frac{\partial^2 \, (E_{HF}/A)}{\partial \, k_F^2} \tag{2.3}$$

where k_F is the Fermi linear momentum and (E_{HF}/A) is the total mean field energy per nucleon obtained in the framework of the HF approach with the given effective nucleon-nucleon interaction. For instance in the case of the Skyrme effective interaction the expression (2.3) allows to connect the modulus K_∞ directly with the parameters t_0, t_1, t_2, t_3 (see (1.2)) [32]

$$K_\infty = \frac{6}{5} \, \frac{\hbar^2}{2m} \, k_F^2 + \frac{9}{4} t_0 \rho + \frac{15}{8} t_3 \rho^2 + \frac{3}{4} (3t_1 + 5t_2) \rho k_F^2 \tag{2.4}$$

In the case of the GMR the moment $m_1(E0)$ (the energy weighted sum rule EWSR) (see (1.73) is usually compared with the simple estimation

$$m_1(E0) = \frac{\hbar^2}{2m} \, A \, \langle r^2 \rangle \tag{2.5}$$

where $\langle r^2 \rangle = \langle BCS | \, r^2 \, | BCS \rangle$. This estimation was obtained from (1.75) when the E0 transition operator $\sum r_i^2 Y_{00}$ is used as the operator $\hat{M}$ and if the interaction part of the Hamiltonian $\hat{H}$ is neglected in the calculation of the double commutator in the rel. (1.75) - see [43, 48]. However, one should realize that the Skyrme effective interaction is velocity dependent and it cannot be neglected in the calculation of the double commutator in (1.75). Therefore the sum rule (2.5) gives only some rough estimation of the moment $m_1(E0)$. It is used for a simple estimation if the used configuration space is sufficiently big.

2.2 Experimental data on the GMR

The first experimental results for GMR date to 70's, using the (α, α') reaction with energy of α particles around 150 MeV. Although α particles were appropriate for these experiments because of their well defined parity and momentum 0^+ (first excited state is beyond separation energy), there still remained the big problem, how to distinguish between GMR and GQR. This problem was solved, at least partially, by using beams with higher energy 240 MeV and cross section measurements at extremely low angles. Then measurements at various angles allowed to distinguish various giant resonance from isoscalar E0 up to isoscalar E3 using so-called multipole decomposition analysis [12].

Currently there are two main groups, which measure GMR: one is at Texas A&M University (TAMU) and the other at Research Center for Nuclear Physics at Osaka University (RCNP). Even though they use the same experimental method, there is still difference in the strength functions of both these experiments, as

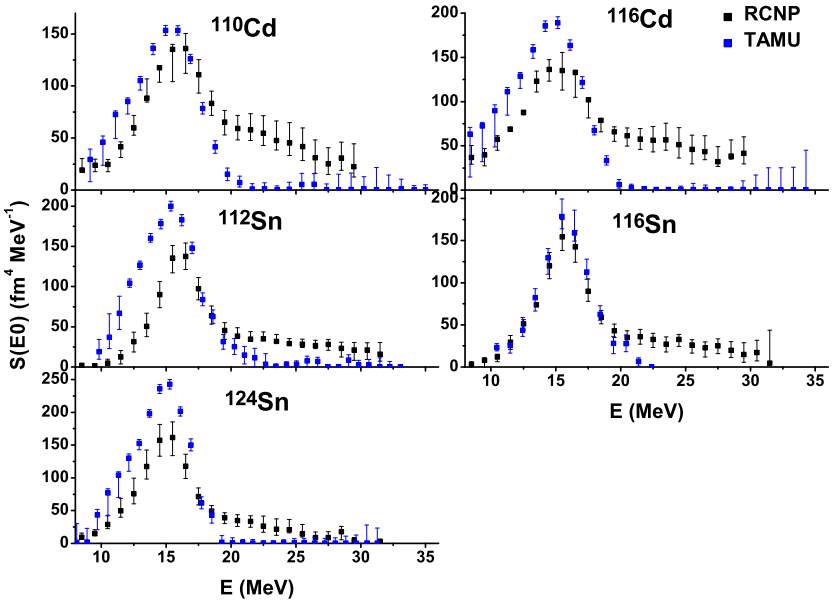

Figure 2.1: Comparison of data from TAMU and RCNP experiments for various spherical nuclei. The data are taken from: RCNP data for Cd[17], Sn[49], TAMU data for Cd[50], ^{116}Sn[22], ^{112}Sn, ^{124}Sn[13]

it can be seen from the mutual comparison of the experimental E0 strength functions for various nuclei, for which the data from both experiments exist. The comparison of experimental E0 strength function distribution obtained by these groups are shown in Fig. 2.1 for selected spherical nuclei. Similar discrepancies can be observed in deformed nuclei as it will be discussed later. The source of discrepancies between both these experimental groups is not known.

Element	Isotopes	Data with references
Zr	$^{90-94}$Zr	TAMU, [51]
Mo	^{92}Mo, $^{96-100}$Mo	TAMU, [51]
Cd	^{110}Cd, ^{116}Cd	TAMU, [50]
	^{106}Cd, $^{110-116}$Cd	RCNP, [17]
Sn	^{116}Sn	TAMU, [22]
	^{112}Sn, ^{124}Sn	TAMU, [13]
	$^{112-124}$Sn	RCNP, [49]
Sm	^{144}Sm, ^{154}Sm	TAMU, [49]
	^{144}Sm, $^{148-154}$Sm	RCNP, [12]
Pb	^{208}Pb	TAMU, [22]

Table 2.1: An overview of data with references for isotopes used in this thesis.

It should be also noted that units in which experimental E0 strength functions are presented in both exp. groups are not same. The RCNP data of the strength function $S_0(E0; E)$ are given in the absolute units: $fm^4\,MeV^{-1}$ while the data of the TAMU group are given relatively with respect to the E0 EWSR value, that means in the fraction of EWSR MeV^{-1}. Since we want to present the comparison of calculated E0 strength functions with corresponding experimental values from

both these groups we renormalized the TAMU data to absolute units $fm^4\,MeV^{-1}$ using the following formula

$$S_0(E0,\,E;\,fm^4\,MeV^{-1}) = S_1(E0,\,E;\,\text{fraction of EWSR}\;MeV^{-1}) \times EWSR \times E^{-1} \tag{2.6}$$

where EWSR value for each nucleus is given by the moment $m_1(E0)$ in (2.5).

In the table 2.1 we present an overview of the experimental data with references for nuclei, used in this thesis.

3. Numerical application of the SRPA

For the numerical application of the BCS+RPA method for the calculation of energies and structure of excited states in the spherical and deformed nuclei including giant resonances described in the previous chapter the chain of codes was made in the IPNP MFF in the collaboration with the University of Erlangen and JINR Dubna. Starting with the Skyrme effective interaction with given parametrization and with the properly chosen set of external exciting single-particle operators $(\hat{Q}_k, \hat{P}_k)$ $(k = 1, \ldots, N)$ (see (1.44)) the SRPA equations (1.56), (1.59), (1.62) are numerically solved. As a result we obtain the structure (that means amplitudes $\psi_{ij}^{(\nu,q)}$ and $\phi_{ij}^{(\nu,q)}$ (see (1.62)) and corresponding energies $\hbar\omega_\nu$ of the phonon creation (Q_ν^+) and annihilation (Q_ν operators of phonons (see (1.39)). The other option is the direct determination of the strength function $S_k(Z\lambda\mu; E)$ (see (1.72) for a given $Z = el, mg$ and multipolarity λ with its projection μ. The individual codes of the above mentioned chain of calculations is described in the Section 3.1.

Since the Hartree-Fock mean field is supposed to be axially symmetric the projection of the angular momentum onto the symmetry axis (the 3-d axis) is a good quantum number (together with parity) for the eigen states of the nuclear Hamiltonian. Therefore solving of the SRPA equation and a subsequent calculation of the strength function can be done separately for each value of the angular momentum projection $K = \mu$ and a parity $\pi = \pm$. The multipolarity projection μ_k and the parity π_k of the starting operators $(\hat{Q}_k,\ \hat{P}_k)$ should be equal to the given K and π for which the SRPA equation is solved. For instance for the case of E0 transitions (excitations) the angular (multipolarity) projection and parity of all exciting operators are always $\mu = 0$ and $\pi = +1$, respectively, and therefore the character of the exciting operators should corresponds to $\mu = 0$ and $\pi = +1$, e.g. operators $\hat{Q}_k = \sum_i f_{\lambda_k}(r_i) Y_{\lambda_k \mu_k = 0}(\theta_i \phi_i)$ with $\lambda_k = 0,\ 2,\ 4, \ldots$ and with different radial dependencies $f_{\lambda_k}(r)$. More detailed discussion of the exciting (input) operators, used for the GMR analysis, is presented in the Subsection 3.2.1.

Since for a practical reason we should cut a number of HF single-particle states and to the configuration space for a subsequent SRPA calculation the influence of the configuration space size on the shape of the GMR is discussed in the Subsection 3.2.2.

In the Subsection 3.2.3 the Lorentz averaging energy interval Δ (see (1.66)) is debated from the point of view of the GMR shape. The Subsection 3.2.4 is devoted to the influence of different choices of the pairing regimes used in the solving of the BCS equations on the E0 strength distribution. The choice of the Skyrme parametrizations used in this thesis is discussed in the Subsection 3.2.5 and the effect of taking into account the time-odd densities and currents in the Skyrme energy functional is analyzed in the Subsection 3.2.6. Finally in the Subsection 3.2.7 the comparison of the SRPA results with ones obtained by the standard (full) RPA is presented.

3.1 Chain of the SRPA codes

The numeric solution of the Skyrme HF+SRPA is in practice carried out in terms of the chain of these subsequent codes:

- `Skyax`
- `Skyax_me`
- `Skyax_srpa`

Since we study, in general, the axially deformed nuclei all the codes mentioned above work with the axial basis of the single-particle wave functions $\phi_i(\vec{r}) = \phi_{ik_i}(\rho, z, \varphi)$, where the coordinate vector $\vec{r}$ is written in the cylindrical coordinate frame $\vec{r} \equiv \rho, z, \varphi$ and the angular momentum projection K_i is a good quantum number for each single-particle state i. For each single-particle state i the corresponding wave function is represented on the 2D mesh of points $(\rho_j,\ z_j)$ $(j = 1, \ldots, n_{mesh})$ (because of the axially symmetry the angle φ_j is irrelevant for the single-particle scheme and in the calculation of all matrix elements it is possible to integrate explicitly over these angles φ_j).

3.1.1 `Skyax` code

The first step of calculation - provided by the code `Skyax` - is a numeric implementation of the Skyrme HF+BCS equations described in the Section 1.2. The only physical inputs for the `Skyax` code are the Skyrme functional parameters t_0, t_1, t_2, t_3, t_4, κ_0, κ_1, κ_2, κ_3, α - see (1.13) , and the parameters $V_p^{(pair)}$, $V_n^{(pair)}$ (see (1.17)) of the pairing part of the functional. The `Skyax` code enables us to use a variety of pairing regimes. The ones used in our calculations are either volume pairing, which is given as:

$$V_{\rm pair}(\boldsymbol{r}, \boldsymbol{r'}) = V_{p,n}\delta(\boldsymbol{r} - \boldsymbol{r'}) \tag{3.1}$$

or surface pairing, which is given as:

$$V_{\rm pair}(\boldsymbol{r}, \boldsymbol{r'}) = V_{p,n}[1 - (\frac{\rho(\boldsymbol{r})}{\rho_0})^{\gamma}]\delta(\boldsymbol{r} - \boldsymbol{r'}) \tag{3.2}$$

where ρ_0 is the additional pairing parameter (usually its value is equal to the mean nucleon density $\rho_0 \approx 0.166$, whereas in the SV parametrization set it is determined within the fitting procedure, which determines also the pairing constants $V_p^{(pair)}$ and $V_n^{(pair)}$).

The output of the HF+BCS calculation are single-particle wave functions $\phi_{ik_i}(\rho, z, \varphi)$ in the HF basis and the Bogoliubov amplitudes U_i and V_i (see (1.30)). Also the total energy of the ground state, $E = \langle BCS|\hat{H}|BCS\rangle$, is computed for a given deformation β (see (1.33) and the text below it).

3.1.2 `Skyax_me` code

After solving the HF+BCS problem with the `Skyax` code and finding the equilibrium deformation β (see the text below (1.33)) in the second step of the calculation

- provided by the code `Skyax_me` - we evaluate the matrix elements of operators $\hat{Q}_k$, $\hat{P}_k$, $\hat{X}^{q'}_{kq}$, $\hat{Y}^{q'}_{kq}$ in the HF-BCS basis corresponding to the set of the input operators ($\hat{Q}_k$, $\hat{P}_k$) ($k = 1, \ldots, N$) used for the subsequent calculation of the transition probabilities and strength functions. The code `Skyax_me` determines also matrix elements of the corresponding transition operator $\hat{M}$ (see (1.64) - (1.75)).

The input in the `Skyax_me` code is the output from the `Skyax` code, and furthermore we have to specify the transition operator $\hat{M}$ and the input exciting operators $\hat{Q}_k$ and $\hat{P}_k$.

3.1.3 `Skyax_srpa` code

In the last step - provided by the code `Skyax_srpa` - the SRPA matrix (1.56), (1.57) is completed. Subsequently we find directly the transition spectrum in the form of the strength function (1.64). Optionally we can also calculate the eigen energies and wave functions of the particular RPA states by the direct solution of the SRPA equation (1.56).

The code `Skyax` was developed by the group of prof. P.-G. Reinhard in the University of Erlangen and was adopted by our group as a starting tool for our calculations. Our group constructed the subsequent codes `Skyax_me` and `Skyax_srpa` which numerically solve the SRPA equations.

The main contribution of this thesis into the system of above mentioned codes was to correct the implementation of the pairing in the codes, to modify the determination of the strength functions by adding the possibility to use energy dependent Lorentz averaging interval $\Delta(E)$ (see (1.66)) - so called double folding - which is discussed in the Subsection 3.2.3. The other contribution consists in the modification of the codes and tuning of inputs for E0 transitions and the GMR. This is discussed in details in the next section.

3.2 Tuning of the SRPA codes

The BCS+SRPA method described in the Chapter 1 is self-consistent method in the sense that the single-particle (or single quasiparticle) mean field and corresponding residual interactions are obtained from the same given Skyrme effective nucleon-nucleon interaction without introducing any new free parameters. The only parameters which are involved in the method are parameters of the effective interaction (which were determined independently before their application in the BCS+SRPA method). However one can find implicitly hidden "parameters" in the numerical application of this method. These are connected with the choice of the exciting (input) operators ($\hat{Q}_k$, $\hat{P}_k$) ($k = 1, \ldots, N$) (1), the size of the configuration space used (2), the size and the form of the Lorentz averaging interval Δ (3), the choice of the pairing regime used in the pairing part of the Skyrme energy functional (4), the choice of the parametrization of the Skyrme interaction (Skyrme energy functional) (5), the importance or unimportance of the taking into account the terms in the Skyrme energy functional involving the time-odd densities and currents (6). Finally it is also necessary to check the SR-

PA method by comparing it with the standard RPA approach. All these features are discussed in the next subsections.

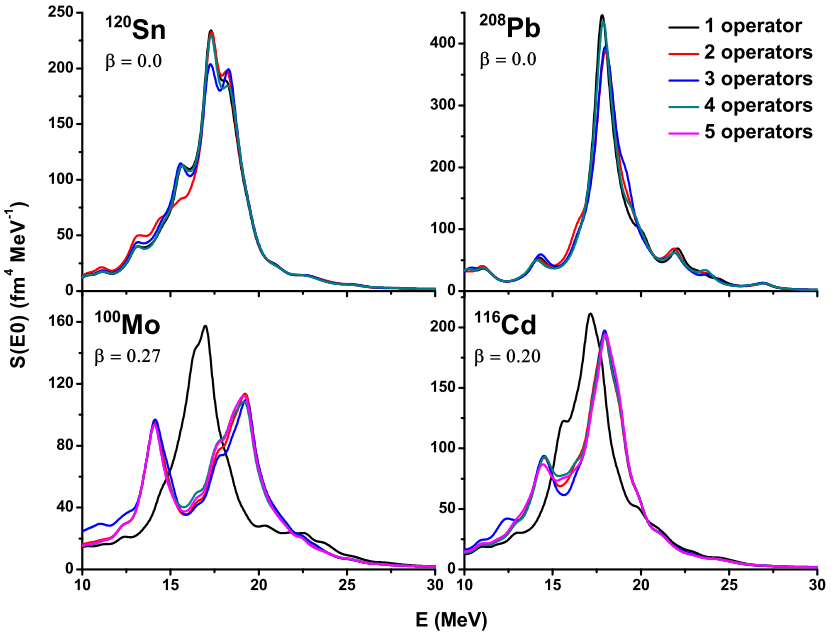

Figure 3.1: E0 strength function with increasing number of input operators in SRPA for ^{120}Sn, ^{208}Pb, ^{100}Mo, ^{116}Cd. Skyrme parametrization used was SLy6, with Lorentz widening parameter $\Delta = 1$ MeV. The increasing sets of input operators are, in this order:
^{120}Sn: $\sum r^2 Y_{00}$, $\sum j_0(0.5z) Y_{00}$, $\sum r^3 Y_{00}$, $\sum j_0(1.0z) Y_{00}$,
^{208}Pb: $\sum r^2 Y_{00}$, $\sum j_0(1.1z) Y_{00}$, $\sum j_0(1.3z) Y_{00}$, $\sum r^6 Y_{00}$,
^{100}Mo: $\sum r^2 Y_{00}$, $\sum r^3 Y_{20}$, $\sum j_0(0.6z) Y_{00}$, $\sum r^3 Y_{00}$, $\sum j_0(0.7z) Y_{00}$,
^{116}Cd: $\sum r^2 Y_{00}$, $\sum r^3 Y_{20}$, $\sum j_0(0.5z) Y_{00}$, $\sum j_0(0.7z) Y_{00}$, $\sum r^2 Y_{20}$,

3.2.1 The choice of the input operators

As it was described in the Section 1.4 the starting point of the SRPA method is the choice of the exciting operators $(\hat{Q}_k,\ \hat{P}_k)$ $(k = 1, \ldots, N)$ for the given type and multipolarity of the transition we want to investigate. We should decide the form and a number of these external fields. In the standard RPA approach such exciting operators are not present and in this sense the SRPA method seems to be more approximate than the standard RPA. However, as it will be shown in the Subsection 3.2.7 for the case of E0 transitions, for each type and multipolarity of transition it is possible to find a set of exciting operators which enables us to obtain a good agreement of the corresponding strength function calculated by the SRPA with that obtained with the standard RPA. One should bear in mind the fact already mentioned in the Chapter 1, that the SRPA approach need not construct huge matrices as it is the case with the standard RPA. Thus, the SRPA approach is suitable for heavy nuclei where configuration spaces of large size are necessary and therefore huge matrices are needed.

The first choice for the input operator for electric transitions would be equal to the form of the transition operator, which in a long-wave approximation of the corresponding electric multipole operator is following:

$$\hat{Q}_1 = r^\lambda(\mathrm{Y}_{\lambda\mu} + \mathrm{Y}^*_{\lambda\mu}) \tag{3.3}$$

for given multipolarity and projections λ and μ. The obvious choices for further input operators would be the following, non-leading terms in the long-wave approximation:

$$\hat{Q}_k = f_k(r)(\mathrm{Y}_{\lambda\mu} + \mathrm{Y}^*_{\lambda\mu}) \tag{3.4}$$

where $f_k(r) = r^{\lambda+2(k-1)}$. The corresponding generalized momentum operator $\hat{P}_k$ can be then taken from the condition $\hat{P}_k = \mathrm{i}[\hat{H}, \hat{Q}_k]$. Of course, the power function $f_k(r) = r^{\lambda+2(k-1)}$ is not the only choice, any reasonable function could be used. The SRPA programs allow, besides the power function, use of the spherical Bessel functions:

$$f_k(r) = j_\lambda(q^k_\lambda r) \tag{3.5}$$

with $q^k_\lambda = a_k \frac{z_\lambda}{R_{diff}}$, where z_λ is the first root of the spherical Bessel function $j_\lambda(z_\lambda) = 0$ and R_{diff} is a diffraction radius of the given nucleus, taken as $R_{diff} = 0.93A^{1/3}$fm. The parameter a_k then takes usually the values of the order of tenths, for E0 transitions it is usually $a_k = 0.4$ and $a_k = 0.6$.

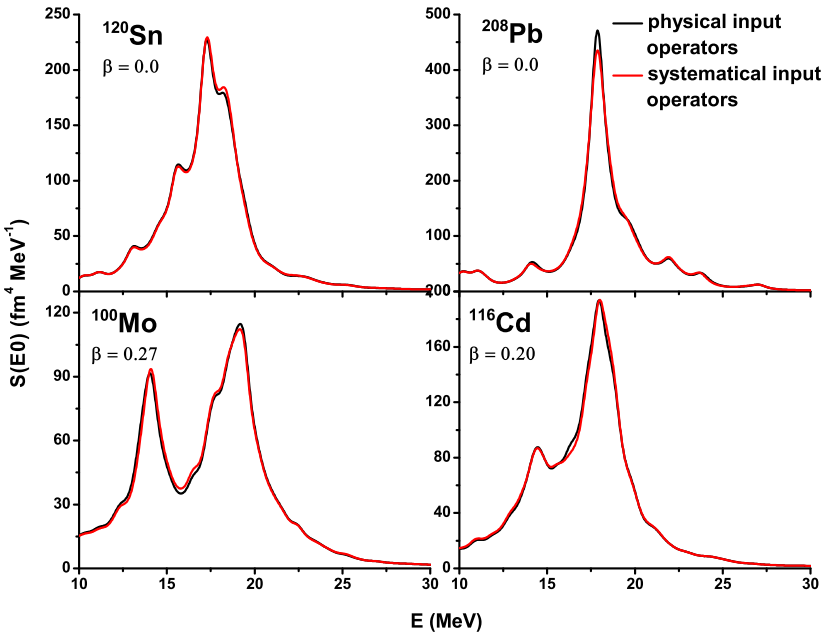

Figure 3.2: Comparison of strengths functions for four different nuclei and two sets of SRPA input operators. The first set is based on intuitive physical arguments, the second set is determined systematically. The first set for spherical nuclei is equal to: $\sum r^2\mathrm{Y}_{00}$, $\sum r^4\mathrm{Y}_{00}$, $\sum \mathrm{j}_0(0.4z)\mathrm{Y}_{00}$, $\sum \mathrm{j}_0(0.6z)\mathrm{Y}_{00}$. The first set for deformed nuclei is the same, with added quadrupole operator $\sum r^2\mathrm{Y}_{20}$. The systematically determined sets are listed in the figure Fig. 3.1. The Skyrme parametrization used in the calculations was SLy6, the Lorentz widening parameter was $\Delta = 1$ MeV.

The basic notion is, that the first operator affects mainly the surface of the nucleus, where most of the collective motion takes part. The following power

operators have more and more effect in the interior of the nucleus. And lastly the spherical Bessel operators are used for more fine-tuned effect on the interior.

The choice of the input operators is generally made more or less intuitively on qualitative basis, choosing the input operators, that we know will be relevant from the long-wave approximation, and excluding those that we know will not be relevant, based on multipolarity or parity exclusion rules, as it was described in the previous paragraphs. However, the next part of this subsection provides a systematic study, which was made to show, that this choice is indeed correct. It also shows, that the SRPA is internally consistent for the small number of input operators - that is, that the strength function saturates after a few input operators are taken into account, and thus, that these give the full information, that we can get from the SRPA.

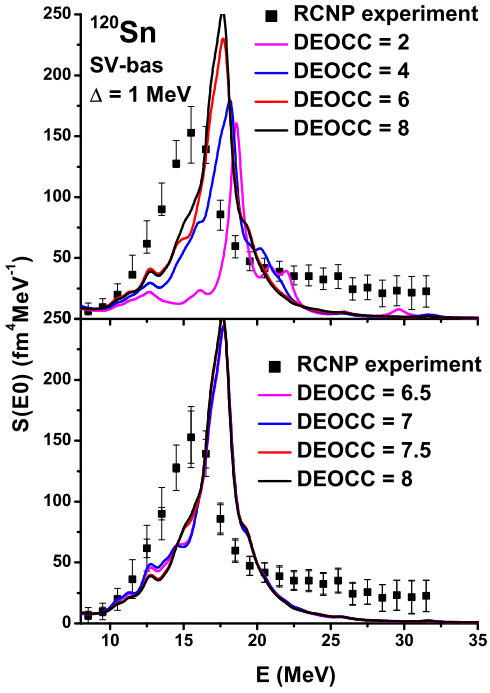

Figure 3.3: Convergence of the E0 strength function for ^{120}Sn. The upper figure has wider range of the parameter DEOCC. The lower figure has values of DEOCC close to the maximum value 8. The input operators used for the calculation are: $\sum r^2 Y_{00}$, $\sum r^4 Y_{00}$, $\sum j_0(0.4z) Y_{00}$, $\sum j_0(0.6z) Y_{00}$. The results are compared with experimental data from RCNP experiment[49]

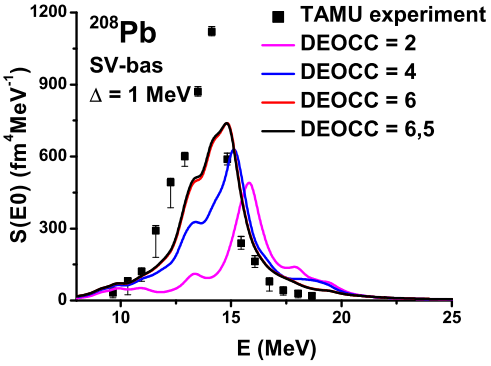

Figure 3.4: Convergence of the E0 strength function for ^{208}Sn. The input operators used for the calculation are: $\sum r^2 Y_{00}$, $\sum r^4 Y_{00}$, $\sum j_0(0.4z) Y_{00}$, $\sum j_0(0.6z) Y_{00}$. The results are compared with experimental data from TAMU experiment[52]

The systematic study worked as follows: we increased gradually number of operators, choosing respectively the one operator, out of a set of all conceivable operators, which made the biggest change with respect to smaller number of operators. The change was determined from the strength functions by the means of χ-square distance. We choose two spherical nuclei - double magic ^{208}Pb and ^{120}Sn and two axially deformed nuclei with different deformations: ^{100}Mo and ^{116}Cd.

The convergence of the strength functions is showed in Fig. 3.1. Comparison of the final strength functions with the strength functions determined with input operators based on heuristical physical arguments, described in previous paragraphs, is in Fig. 3.2. One can see that only a few input operators are sufficient to obtain a convergence.

3.2.2 Influence of the configuration space size

As it was mentioned in the Section 3.1 the Hartree-Fock single-particle wave functions $\phi_i(\vec{r}) = \psi(\rho, z, \varphi)$ are provided by the `Skyax` code in the form of their values in the mesh of points (ρ_k, z_k) $(k = 1, \ldots, n_{mesh})$ together with their single-particle energies e_i. Generally the HF (or BCS) method gives the infinite number of single-paricle (or single-quasiparticle) states. In practice, certainly, we should cut off the number of single-particle (or single-quasiparticle) states i to some finite value N $(i = 1, \ldots, N)$. In the `Skyax` code this cutting off the configuration space is done by the upper energy limit (cut off energy) of the single-particle energies. That means only HF single-particle states with energies e_i up to the cut off energy are provided by the HF calculation and are taking into account in the subsequent SRPA calculation.

The cut-off energy is in the program `Skyax` represented by a parameter DEOCC, in such a way, that

$$\text{energy of s.p. states} < (1.4A^{1/3} + \text{DEOCC}) * 41 * A^{-1/3}\text{MeV}. \qquad (3.6)$$

In the figures Fig. 3.3 and Fig. 3.4 the convergence trend can be observed with increasing cut-off energy for ^{120}Sn and ^{208}Pb nuclei. We see clear convergence within the numerical limits of the `Skyax` and SRPA programs. In the figures are also included experimental results for comparison. Although enlargement of the configuration space improves agreement of the theoretical results with experiment, it is not possible to reach the agreement entirely. Particularly for the soft ^{120}Sn isotope, for which the 'hard' SV-bas parametrization (with $K_\infty = 234$ MeV) is expected to give worse agreement, we see, that even after convergence, the predicted peak is shifted at least 1 MeV to higher energies, compared to the experimental result, and no further increase in configuration space would change this. Similar convergence was obtained also for other nuclei investigated in this thesis.

The discretization of the wave functions is in the program `Skyax` done by defining the wave functions on the points of the rectangular mesh in the (ρ, z) space. The spacing of the mesh, and the number of mesh points is determined in the `Skyax` input separately for ρ and z coordinate. In our calculations we choose the default setting of the `Skyax` program, i.e., 0.7 fm for both ρ and z spacing, and the number of mesh points on the ρ and z axis 35 and 61 respectively. Studies of other multipolarities within our approach showed, that these values provide reliable outputs, and, because their choice does not have as such an impact on the strength function as the choice of the cut-off energy, they present a good compromise between accuracy and the computation time.

3.2.3 Influence of the Lorentz averaging interval

A typical nuclear excitation spectrum for a given type and multipolarity (for instance the excitation in terms of the photoabsorption reaction which is closely connected with the E1 transitions) consists from well separated discrete states (levels) with energies up to first particle emission threshold energies (usually 8-10 MeV). Above the emission threshold energy the density of states becomes higher and higher. Finally the energy density of states is so big that the finite experimental energy resolution makes impossible to see individual levels in the spectrum or in the energy dependence of the strength functions $S_k(Z\lambda\mu;\, E)$ (see (1.64)) of the excitations of given type $Z = el,\, mag$ and multipolarity λ with the projection μ. In the Section 1.4 it was already presented that the experimental smearing of individual levels is in the calculations of the strength function $S_K(Z\lambda\mu;\, E)$ obtained by the substitution of the Dirac's δ-function involved in (1.64) by the Lorentz function ξ_Δ (see (1.66)) which effectively averages the strength function $S_k(Z\lambda\mu;\, E)$ for each energy E in the interval of the width δ.

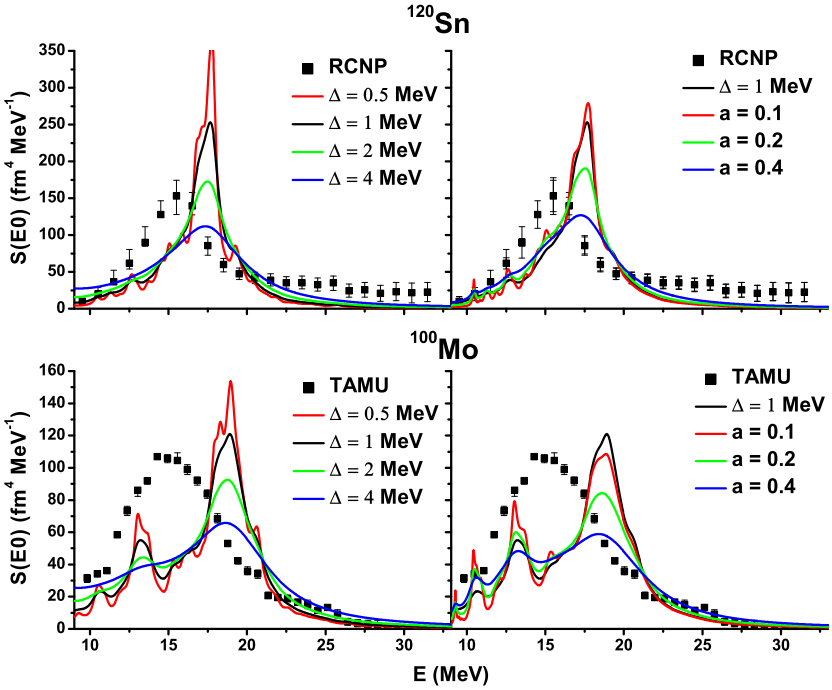

Figure 3.5: GMR strength function for different values of the Lorentz averaging interval Δ and various values of the parameter a in double-folding method for a spherical ^{120}Sn, and deformed ^{100}Mo. Deformation of ^{100}Mo is $\beta = 0.27$. The calculation was done for the parametrization SV-bas, with input operators $\sum r^2 Y_{00}$, $\sum r^4 Y_{00}$, $\sum r^2 Y_{20}$, $\sum j_0(0.4z) Y_{00}$, $\sum j_0(0.6z) Y_{00}$. The experimental data are taken from: Sn[49], Mo[51].

From theoretical point of view the substitution, $\delta(\hbar\omega_\nu - E) \to \xi_\Delta(\hbar\omega_\nu - E)$, in (1.64) or (1.65) simulates some effects not involved in used theoretical approach, in our case the BCS+RPA approach. This approach is restricted to one-phonon states only and it means, as it can be seen from the phonon operator (see (1.39)), the restriction to two-quasi particle configurations only. However it is known (see e.g. [53]) that more complex configuration components in the nucleus excited

states, like two-phonon ones, play an important role in giant resonances (sometime even in low-lying part of the spectrum). The Lorentz averaging of the strength functions $S_k(Y, \lambda\mu;\ E)$ simulates to some extend the taking into account these complex configurations.

The other effect simulated by the Lorentz averaging is connected with so called escape-widths. It is known that in each experiment using the given reaction with given initial channel for obtaining the particular nuclear spectrum always there are open final channels which do not provide information about the investigated spectrum (so called escape channels). Since these escape channels are not usually taken into account by the theory approach used for the description of the spectrum the inaccuracy caused by this leads to additional smearing of the theoretical spectrum. Usually the role of these escape channels increases with the increasing of the excitation energy and therefore the Lorentz averaging width Δ can be expected to increase with the energy as well.

Taking into account both above mentioned effects connected with the complex configurations and with the escape width one can expect the energy dependence of the Lorentz averaging energy interval $\Delta(E)$ in the following form

$$\Delta(E) = \Delta_0 + a(E - E_{threshold)}) \tag{3.7}$$

and the strength distribution $S_k(E)$ is calculated in two steps. First we calculate the strength function (1.65) with a small but fixed value of Δ_0. This gives the strength function $S^{'}(E^{'})$ very closed to the actual RPA one (1.64) but for the equidistant energy grid. In the next step, the strength is additionally folded by using the energy dependent $\Delta(E)$:

$$S_k(E) = \int dE^{'}\ S^{'}_k(E^{'})\, \xi_{\Delta(E)}(E - E^{'}) \tag{3.8}$$

where $\Delta(E)$ is given by (3.7). In our paper [54] this double folding method of the calculation of $S_k(E)$ was used for the dipole E1 strength in the neutron rich tin isotopes. In the case of E1 strength the double folding method improved substantially the agreement of calculated and experimental photoabsorption cross sections. In the case of the E0 strength discussed in this thesis the improvement obtained by the double folding is not so good as it can be seen from the Fig. 3.5 where the dependence of the strength function distribution S(E0) for ^{120}Sm and ^{100}Mo is presented for different values of Δ.

3.2.4 Influence of pairing regimes

In the recent articles there was discussed a possibility of GMR being effected in a major way by pairing correlations. So in this section we will study the effect of volume and surface pairing, compared to a calculation without any pairing. The pairing parameters were fitted for other data, so we will not change these, and we will alter only the pairing modes.

In the figure Fig. 3.6 we compare different pairing settings for a spherical and a deformed nuclei ^{208}Pb and ^{116}Cd. ^{208}Pb, besides being spherical, is also doubly closed-shell, so we would expect no pairing effects at all, which is, to a high accuracy confirmed by our results for both parametrizations SV-bas and SLy6. There is no difference whether we include pairing in our calculations or not. For

a deformed ^{116}Cd, we would expect, based on previous studies of relationship of GMR and pairing effects, a noticeable difference between surface and volume pairing. This, however, was not confirmed, and differences between these two modes are very small, as are differences between any pairing and no pairing at all. Here it should be noted that the inclusion of the pairing for deformed nuclei on the level of the mean field is certainly very important because it gives single-quasiparticle spectrum and in such a way it is important mainly for low lying excitations. However in the giant resonance regions inclusion of the pairing in the residual interaction is not so important which is demonstrated by the figure Fig. 3.6 .

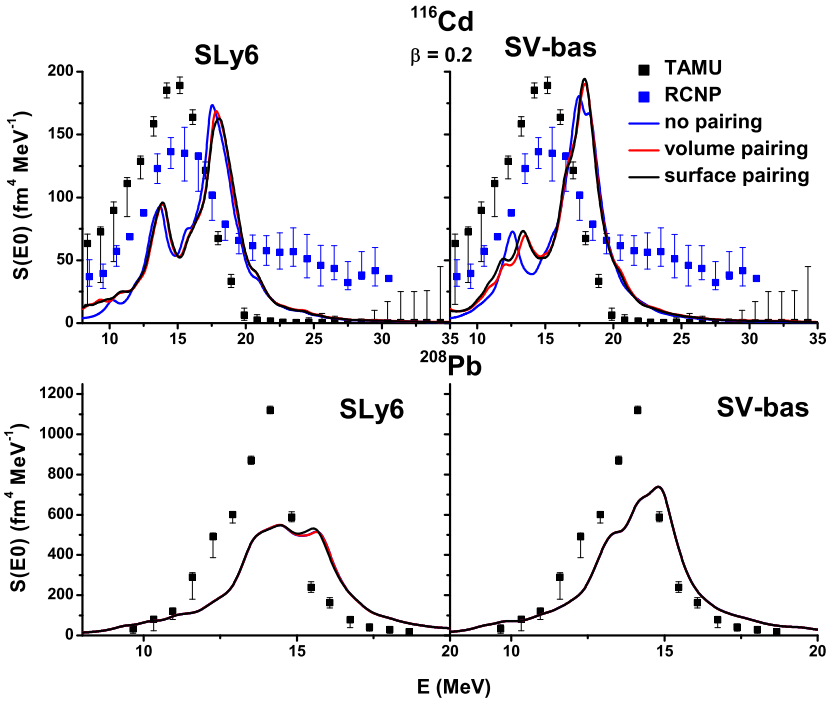

Figure 3.6: Comparison of different pairing settings for spherical ^{208}Pb and deformed ^{116}Cd and for two Skyrme parametrizations: SLy6 and SV-bas. The TAMU data for lead are taken from [52], for cadmium the TAMU data are taken from [50], the RCNP data are taken from [17]. The input operators in both cases were $\sum r^2 Y_{00}$, $\sum r^4 Y_{00}$, $\sum r^2 Y_{20}$, $\sum j_0(0.4z) Y_{00}$, $\sum j_0(0.6z) Y_{00}$. The Lorentz averaging interval is $\Delta = 1$ MeV. The deformation of ^{116}Cd is $\beta = 0.20$.

3.2.5 Influence of the Skyrme effective parametrizations

In this thesis the Skyrme effective interaction is used, which comes with various parametrizations, that had arisen during last 2-3 decades. The original Skyrme interaction parametrizations were obtained by the fitting procedure in order to obtain a good agreement between calculated and experimental values of bulk nuclear properties, like binding energy, nuclear radius, incompressibility, for selected double magic nuclei (see e.g. [32]). Then, in the connection with the effort to describe another different nuclear properties by theoretical approaches with the Skyrme mean field, a lot of additional parametrizations appeared in the literature. Each of these additional parametrizations preserves an agreement in

the above mentioned bulk properties and tries to improve it in the particular property, which is a matter of interest in the given paper. As a result we now have several tens of Skyrme interaction parametrizations giving different values of the nuclear matter characteristics like the effective masses m^*, incompressibility modulus K_∞, symmetry energy a_{sym} [36].

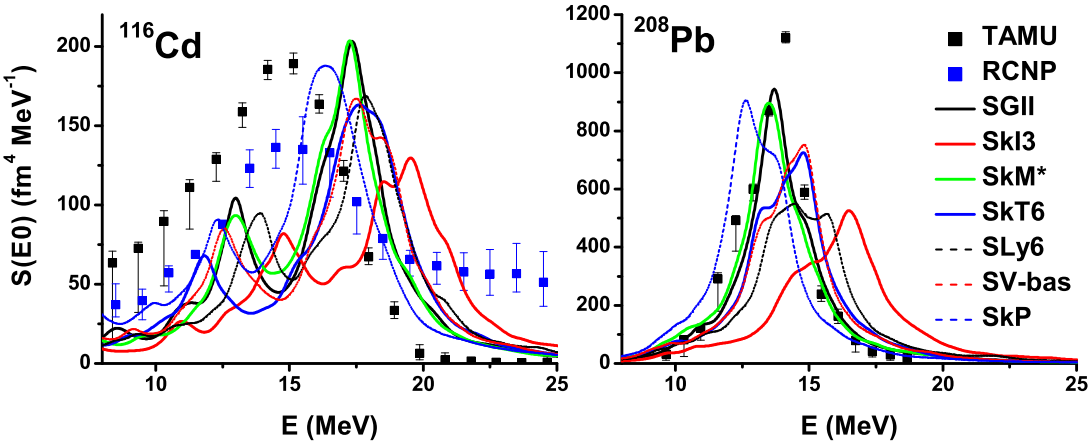

Figure 3.7: Comparison of GMR results for various parametrizations with experimental data. The TAMU data for lead are taken from [52], for cadmium the TAMU data are taken from [50], the RCNP data are taken from [17]. The input operators in both cases were $\sum r^2 Y_{00}$, $\sum r^4 Y_{00}$, $\sum r^2 Y_{20}$, $\sum j_0(0.4z) Y_{00}$, $\sum j_0(0.6z) Y_{00}$. The Lorentz averaging interval is $\Delta = 1$ MeV. The deformation of ^{116}Cd is $\beta = 0.20$.

From the point of view of the GMR the most important Skyrme interaction characteristics is the incompressibility modulus K_∞ as it follows from the character of E0 vibration. In the paper [7] (and also in other papers) the impossibility to describe experimental GMR centroids in lighter nuclei (like Sn or Cd) and heavy nuclei (like Sm or Pb) simultaneously in the framework of one theoretical approach with the same Skyrme parametrization was suggested to explain by different need for the incompressibility K_∞ in the heavier and lighter regions of isotopes. The lighter nuclei (Cd-Sn region) prefer the parametrizations with the lower K_∞ while the parametrizations with the higher K_∞ are better for heavier nuclei (Pb-Sm region). Therefore in this thesis we used different Skyrme parametrizations covering a broad interval of K_∞ (from values $K_\infty \approx 200$ MeV up to $K_\infty \approx 250$ MeV) in order to check this suggestion.

In the figure Fig. 3.7 we see comparison of the GMR given by various standard Skyrme parametrizations, and experimental data. The parametrizations are SGII ($K_\infty = 230$ MeV) [55], SkI3 ($K_\infty = 258$ MeV) [56], SkM* ($K_\infty = 218$ MeV) [57], SkT6 ($K_\infty = 258$ MeV) [58], SLy6 ($K_\infty = 230$ MeV) [59], SV-bas ($K_\infty = 258$ MeV) [36] and SkP ($K_\infty = 202$ MeV) [37]. We can see, that dispersion of the result is quite big so without a comparison with experimental results we would not be able to determine, solely on the basis of the Skyrme interaction calculations, what is the most probable shape or even position of the GMR peak. Moreover, even though for the lead isotope, there are parametrizations, that could reproduce the experimental results quite satisfactorily, for the cadmium isotope, although the SkP parametrization is closest, it is still not downshifted enough

to reproduce the experimental results. So there is no parametrization in the set, which could reproduce the cadmium GMR data, and, consequently, there is no unique parametrization, that could reproduce the GMR data for all nuclei.

Another important finding from the Fig. 3.7 is that no parametrization was able to reproduce even the shape of the strength function for the deformed nucleus. The experimental data reveal the deformation effect only as a widening of the main peak to the width 1-2 MeV. On the other hand the two-peak structure of the strength function is quite dominant for all parametrizations, and even though we know from Fig. 3.5 that this is to some extent dependent on the settings of the Lorentz averaging, and we can flatten out the two-peak structure using the double folding method, we see in Fig. 3.5, that although double folding flattens the strength function, it preserves the distance of the two peaks as the width of the resulting peak. In our case we can see, that even with double folding, we would get a peak with width about 4-5 MeV, way beyond the experimental results.

In spite of the facts concerning not good description of the GMR using different Skyrme parametrizations given above one can extract two conclusions from the comparison given in the Fig. 3.7: (1) the theory predicts two peak character of the GMR for deformed nuclei (^{116}Cd has the equilibrium deformation $\beta = 0.20$), (2) the GMR in the lighter nucleus ^{116}Cd is better described by the parametrization SkP with the lower value $K_\infty = 202$ MeV while the heavier nucleus ^{208}Pb need the parametrizations with $K_\infty \approx 220 - 230$ MeV. Both these conclusions are described in more details in the Chapter 4.

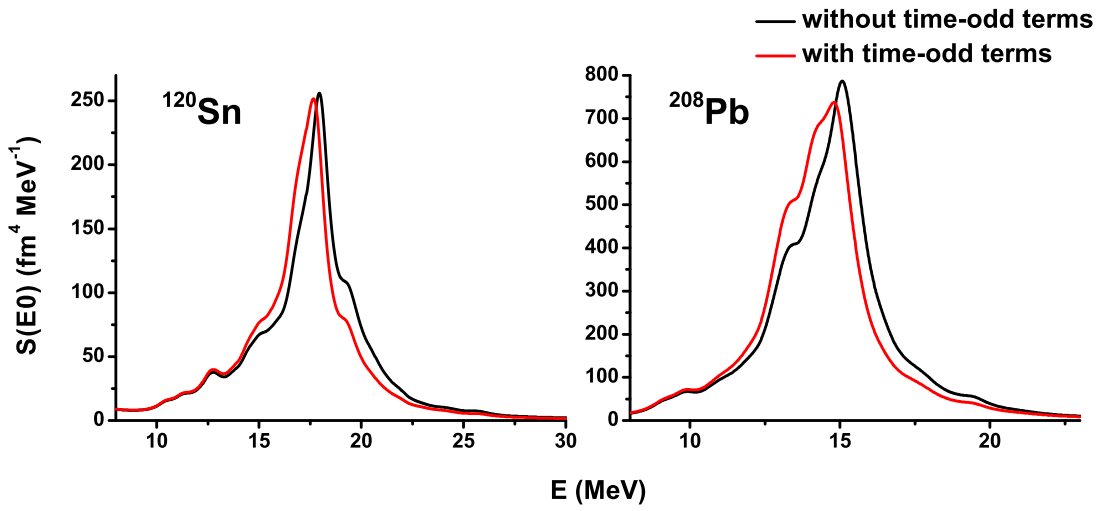

Figure 3.8: GMR results for ^{208}Pb and ^{120}Sn for SV-bas parametrization with or without including the time-odd terms in Skyrme functional. The input operators in both cases were $\sum r^2 Y_{00}$, $\sum r^4 Y_{00}$, $\sum j_0(0.4z) Y_{00}$, $\sum j_0(0.6z) Y_{00}$. The Lorentz averaging interval is $\Delta = 1$ MeV.

3.2.6 Skyrme time-odd densities and currents

The Skyrme functional in its most general form includes terms with both time-even and time-odd densities (see (1.13) and the Table 1.7) . The terms with time-odd densities and currents, however, are added by hand following symmetry

arguments, because they do not have any effect on the ground state properties, ground state itself being time-even, and Skyrme parametrizations are fitted for the main part from the ground state properties. In this subsection we have a brief look at how time-odd terms actually influence systems with excited states. In the figure Fig. 3.8 we see GMR strength functions for ^{208}Pb and ^{120}Sn for SV-bas parametrization with/without including time-odd terms in Skyrme functional. We can see, that the effect of the time-odd terms is discernible but not very significant. The inclusion of the terms with time-odd densities and currents shifts the strength function towards smaller energies and this improves the agreement with experimental data a little bit but the effect is very small.

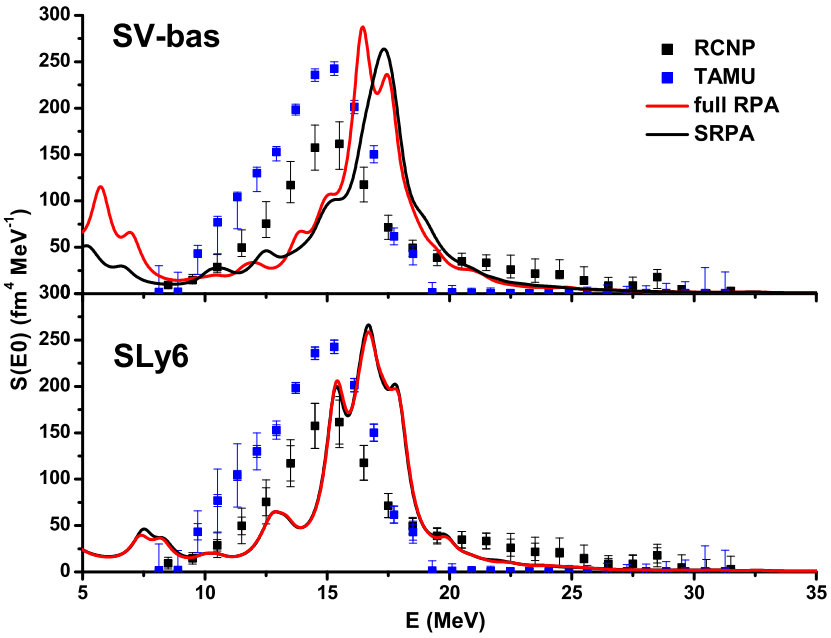

Figure 3.9: Comparison of SRPA and full RPA GMR strength functions for ^{124}Sn for the parametrizations SV-bas and SLy6. The Lorentz averaging interval in SRPA calculations is $\Delta = 1$ MeV. Excitation input operators used in SRPA calculations are: $\sum r^2 Y_{00}$, $\sum r^4 Y_{00}$, $\sum j_0(0.4z) Y_{00}$, $\sum j_0(0.6z) Y_{00}$. Experimental data are taken from RCNP[49] and TAMU[13].

3.2.7 SRPA vs RPA

In order to show the relevancy of the SRPA method, in this subsection we compare the results obtained for SRPA using the parameters which were fine tuned in the previous subsections with results obtained from the full (standard) RPA. In our group we developed the full RPA code for spherical nuclei therefore the comparison of the GMR obtained by the SRPA are compared with one obtained by the full RPA is done for spherical nuclei only. Some preliminary comparison of the SRPA GMR with the full RPA GMR shows that we would get a similar dis/agreement also for axially deformed nuclei. This will serve as a basis for considering correctness of SRPA approximation as compared to RPA.

In the graph Fig. 3.9 we can see a comparison between a SRPA calculation and a full RPA calculation for ^{124}Sn. We can see, that in the resonance region

there is a very good agreement between the two approaches. And even for SV-bas, where the agreement is worse, it is far below the difference between two different Skyrme parametrizations, calculated within the same approach. We conclude, that if done properly, the SRPA method, which is more effective from technical point of view, is a good replacement for full RPA method for GMR numerical calculations.

4. Results

In this chapter the results of BCS+SRPA calculations of the GMR are discussed and compared with available experimental data for spherical as well as deformed nuclei. However, as it was mentioned in the Section 2.2, in this comparison one should have in mind that available experimental GMR data come from two experimental groups, TAMU and RCNP groups, and in some cases (mainly for deformed nuclei) the data from both these groups differ considerably.

In the first section of this chapter some criticism of up to date theoretical analyses of the GMR based only on the GMR centroids is given. Then, in the Section 4.2, we focus on the comparison of calculated GMR with experimental values for spherical nuclei, namely for the chains of lead, tin, zirconium isotopes and ^{144}Sm nucleus. Unlike other theoretical groups we compare mainly strength functions because we believe that these functions offer more relevant information for the comparison with experiments than only energy centroids of the GMR. From this point of view the data of both experimental groups mentioned above are mutually compared as well.

Finally in the Section 4.3 we analyze the GMR in deformed nuclei, namely in the chains of molybdenum, cadmium and samarium isotopes. As it was already mentioned in the Introduction, our study of the GMR in deformed nuclei represents the first analysis of deformation effects of the GMR performed in the framework of a microscopic self-consistent approach. It is clearly shown that these deformation effects are connected with the coupling of E0 and E2 modes in deformed nuclei.

4.1 Energy centroids and sum rules

Up to now theoretical analyses of the GMR have been reduced to the GMR centroids only and only in spherical nuclei. Practically in all theoretical papers concerning the GMR, the centroids are calculated using the expr. (1.76), $E_{ISGMR} = m_1(E0)/m_0(E0)$, where moments $m_0(E0)$ and $m_1(E0)$ are given by (1.73). To be more precise, in practice in the literature, the integral in (1.73) is not taken in the limits (bounds) from 0 to ∞ but the integration goes over a finite energy interval containing the GMR, usually energies from the lowest particle emission threshold (8-10 MeV) up to 20-30 MeV (see e.g. [7]). In order to compare the calculated GMR centroid with experimental data the experimental GMR centroid is calculated from the experimental E0 energy distribution again using exprs. (1.76) and (1.73). According to the experimental papers (see e.g. [17]) one should be careful and take the same energy interval for integrals in (1.73) for both the experimental and theoretical determination of the GMR centroid energy. However this can give some misleadings as it is discussed below.

In RCNP and TAMU (see the Section 2.2) experiments the experimental GMR centroids were determined using different upper integration limits in (1.73). This can be seen from the experimental data presented for both experimental groups in the Fig. 2.1. The RCNP GMR data for spherical nuclei involved in the Fig. 2.1 show the high-energy tail going up to 30-35 MeV. In the TAMU data such tail is not observed and experimental values of $S(E0)$ are almost zero above the energies

20-25 MeV. Nevertheless in the GMR analyses presented in practically all papers (see e.g. [7, 16]) the energy integration interval for the calculation of the GMR centroid was reduced to 10.5-20.5 MeV for both RCNP and TAMU experimental groups and for all theoretical calculations (in spite of the fact that theoretical E0 strength functions are usually nonzero above the energy 20.5 MeV). So the limits for the integration in (1.73) are questionable for both the experiment and theory.

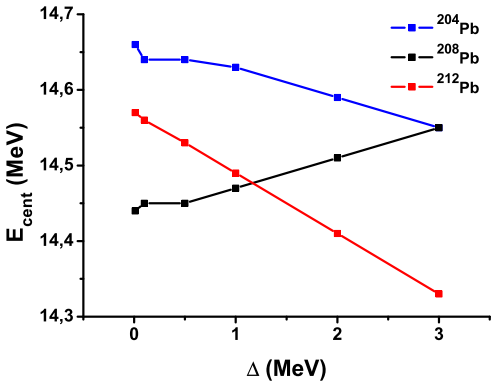

Figure 4.1: Dependence of the energy centroid on the Lorentz averaging interval Δ for lead isotopes. The energy centroids are calculated from the strength function as m_1/m_0 on the interval 10-55 MeV.

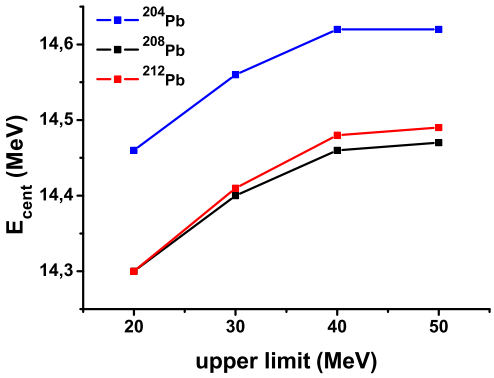

Figure 4.2: Dependence of the energy centroid on the upper limit of the interval 10-X MeV, over which is calculated the energy centroid as a fraction of the strength function moments m_1/m_0. The Lorentz averaging interval is $\Delta = 1$ MeV.

The other question connected with the determination of the GMR centroid is the Lorentz averaging energy interval Δ (see (1.66)) used for the strength function $S_k(E0;\ E)$ involved in the expression (1.73) for moments $m_1(E0)$ and $m_1(E0)$.

Lorentz averaging interval Δ and the choice of the integration interval, over which the the strength function moments $m_k(E0)$ are calculated, influence the value of the energy centroid as it can be seen in the Figs. 4.1 and 4.2 where the GMR centroids are shown in the dependence on Δ and on the upper limit of the integral in (1.73). The choice of Δ moves the E0 energy centroid for lead isotopes in the range of 100-200 KeV. The choice of the energy interval in the integral (1.73) has similar effect with the GMR centroid shift of the order 200-300 KeV if the upper integration limit changes from 20 MeV to 50 MeV.

The difference of 200-300 KeV of the GMR centroid energies, if we change Lorentz parameter Δ and upper integration limit in (1.73) in quite big intervals, seems to be not very big. However, one should realize that the GMR peak for lead isotopes (which are treated in Figs. 4.1 and 4.3) is well centered in the energy interval 10-20 MeV, as we will see later. We can expect this difference to be bigger for nuclei with broader peaks, like tin isotopes, or for the GMR strength functions with the tail in higher energies, like the experimental strength functions obtained by the RCNP experiment (see Fig. 2.1). In the RCNP experiment papers it is always pointed out that it is crucial in the comparison of the experimental centroid energies with theoretically calculated one to keep the same integration energy interval in (1.73) for the determination of the centroid energy interval in (1.73) for the determination of the centroid energy (see e.g. [17]).

However, we cannot agree with this statement. If we compare experimental and calculated energy centroids for lighter nuclei, like Sn, or Cd isotopes, for which the theoretical strength function is shifted to higher energies, and if we use the same interval as experimentalists than we inevitably cut off high energy tails of our strength function and distort results. For this reason we argue that analyses of the GMR only on the base of the comparison of experimental and calculated energy centroids are not sufficient and are misleading. The respectable analysis should involve mainly the comparison of the whole GMR energy distributions (the GMR shape). It is even more important in the case of deformed nuclei.

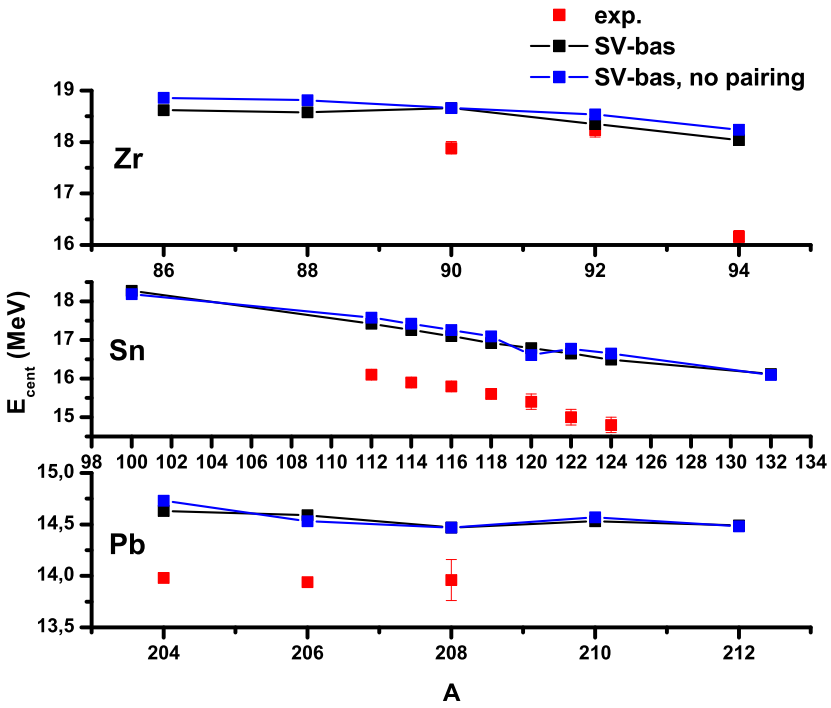

Figure 4.3: Energy centroid results for three chains of spherical nuclei - Zr, Sn, Pb. Comparison between theoretical results with/without pairing and experimental results. Skyrme parametrization used: SV-bas, the Lorentz averaging interval $\Delta = 1$ MeV. The energy ranges for the energy centroids calculation were chosen in accordance with the experimental data (Zr - 9.8-36 MeV, Sn - 8.5-31.5 MeV, Pb - 10-55 MeV). The experimental data were taken from Zr[51], Sn[49] and Pb[7].

In the Fig. 4.3 we demonstrate values of energy GMR centroids calculated using (1.76) for the chains of isotopes Zr, Sn and Pb with the SV-bas Skyrme interaction parametrization and with the surface pairing or without any pairing. In the Table 4.1 we add the information about the exhaustion of the GMR EWSR, that means the percentage of the EWSR value given by exp. (2.5) exhausted by the moment $m_1(E0)$ determined by (see (1.75) and (1.72)):

$$m_1(E0) = \int dE S_1(E0;\, E)\, E \tag{4.1}$$

for different Pb-, Sn- and Zr-nuclei. The percentage of the exhaustion of the EWSR for giant resonances serves as a test if the used configuration space is

sufficient for the analysis of the given giant resonance. From the Table 4.1 one can see that in our calculation of the GMR we exhaust more than 90% of the corresponding EWSR. This means sufficiently big configuration space. Another independent test of the size of the configuration space is the convergence of the strength function with the increasing size of the configuration space which was already discussed in the Subsection 3.2.2.

Pb	EWSR %	Sn	EWSR %	Zr	EWSR %
204	95 ± 5	100	93 ± 5	86	95 ± 5
206	95 ± 5	112	95 ± 5	88	95 ± 5
208	93 ± 5	114	95 ± 5	90	95 ± 5
210	93 ± 5	116	95 ± 5	92	95 ± 5
212	91 ± 5	118	95 ± 5	94	95 ± 5
		120	95 ± 5		
		122	95 ± 5		
		124	95 ± 5		
		134	93 ± 5		

Table 4.1: Exhaustion of the EWSR by our calculations for the chains Pb, Sn and Zr. The EWSR was calculated using the mean value $< r^2 >$ calculated using the HF-BCS ground state determined by Skyax program.

From the graph of centroids given in the Fig. 4.3 we can see, as it is expected, that for double-magic nuclei the inclusion of the pairing has not any influence on the position of the GMR centroid. In the case of nuclei farther from the double-magic region the inclusion of the pairing tends to push the centroid a little bit lower in the energy in most cases (with respect to experimental data), but, as it was already discussed in the Subsection 3.2.4 and it was also found in the [7], the effect of the pairing inclusion on the GMR is almost negligible.

4.2 Spherical nuclei

In this section the GMR in spherical nuclei is analyzed. For this aim we use a relatively new set of the Skyrme interaction parametrization, so called SV parametrization set, which was introduced in [36]. Individual parametrizations in the set were obtained by the fitting procedure where, in addition to standard properties of double-magic nuclei (bind energy, radius), other nuclear matter properties were taken into account, namely the incompressibility modulus K_∞ of the infinite nuclear matter, isoscalar effective mass m^*, the symmetry energy a_{sym}, and Thomas-Reiche-Kuhn classical energy weighted sum rule EWSR κ. The basic parametrization is SV-bas with the parameters obtained by usual fitting on the bulk properties. Then the subset of parametrizations SV-K, SV-mas, SV-sym, SV-kap are obtained from the basic SV-bas parametrization by the additional fitting in order to have the particular value of the corresponding nuclear matter property, K_∞, m^*, a_{sym}, and κ, respectively - see [36] for details. In the Table 4.2 the list of SV parametrizations is given together with corresponding values of the incompressibility K_∞, effective mass ratios m^*/m and the symmetry energy a_{sym} for each parametrization.

force	K_∞	m*/m	a_{sym}
SV-bas	234	0.9	30
SV-K218	218	0.9	30
SV-K226	226	0.9	30
SV-K241	241	0.9	30
SV-mas07	234	0.7	30
SV-mas08	234	0.8	30
SV-mas10	234	1.0	30
SV-sym28	234	0.9	28
SV-sym32	234	0.9	32
SV-sym34	234	0.9	34

Table 4.2: Table of SV parametrizations with the corresponding fitted nuclear properties: incompressibility modulus K_∞ (in MeV), isoscalar effective mass (relatively to the nucleon mass), and symmetry energy a_{sym} (in MeV).

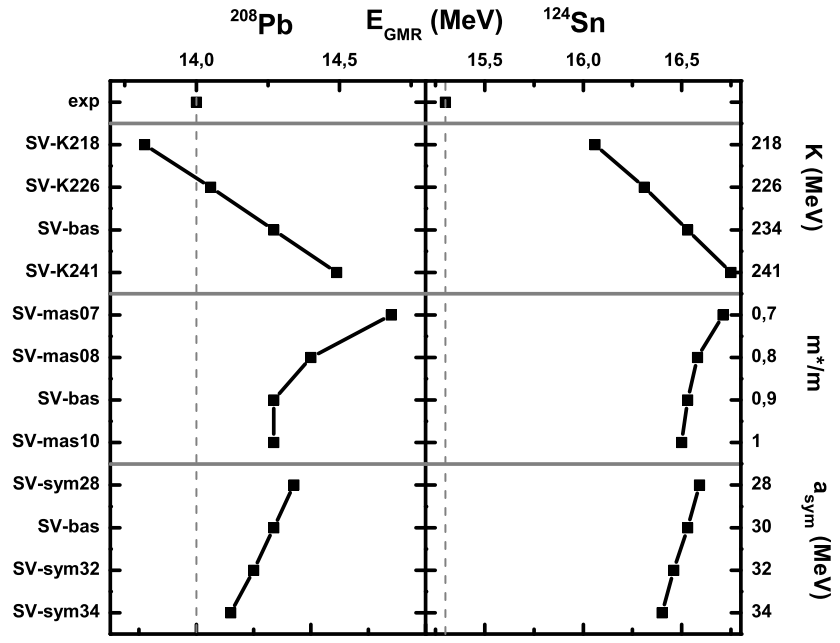

Figure 4.4: Comparison and trends of GMR energy centroids for parametrizations from Skyrme SV set.

In the Fig. 4.4 we compare GMR energy for SV parametrizations, always grouped into three row panels according to three properties (K_∞, a_{sym} and m^*/m) which given parametrizations were fitted to. The calculations were done for ^{208}Pb and ^{124}Sn. From this figure it is clear that the most important nuclear property, on which the position of the GMR centroid is most dependent, is the incompressibility mudulus. Particularly, the decreasing of K_∞ leads to the shift of the E0 centroid to the lower energies. The changing of other quantities, isoscalar effective mass ratio m^*/m or symmetry energy a_{sym}, does not give substantial change of the position of the GMR centroid.

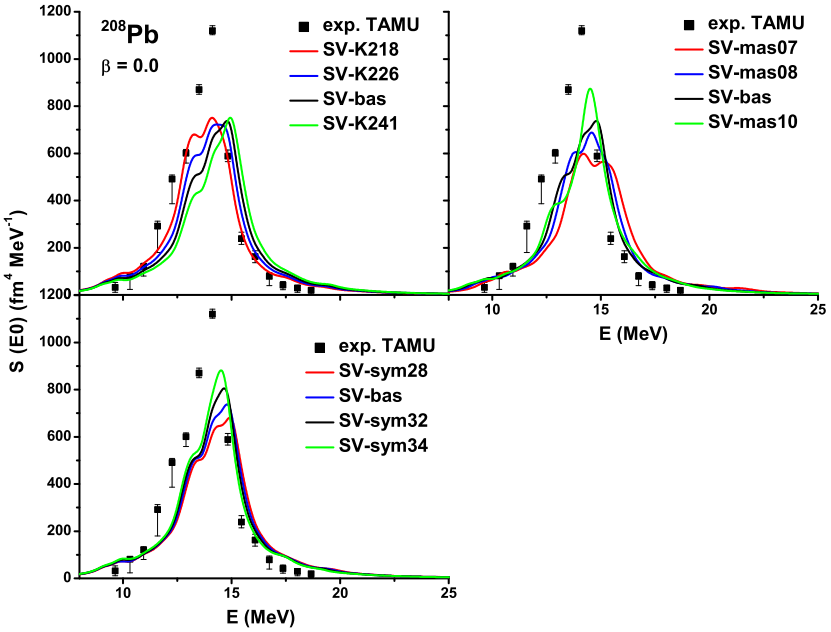

Figure 4.5: Comparison of GMR strength functions for ^{208}Pb for Skyrme parametrizations from SV parametrization set. The input operators used in the SRPA calculations are $\sum r^2 Y_{00}$, $\sum r^4 Y_{00}$, $\sum j_0(0.4z) Y_{00}$, $\sum j_0(0.6z) Y_{00}$. The Lorentz averaging interval is $\Delta = 1$ MeV. The experimental data are taken from TAMU[52].

In the next figures Fig. 4.5 and Fig. 4.6 we compare the GMR energy distribution for ^{208}Pb and ^{124}Sn isotopes calculated with the parametrization sets SV-K (with K_∞ = 218, 226, 234, and 241 MeV), SV-mas (with m^*/m = 0.7, 0.8, 0.8, *and* 1.0), and SV-sym (with a_{sym} = 28, 30, 32, *and* 34) with the experimental GMR distributions taken from the TAMU [52, 13] and RCNP [49] experiments. Again we can see that changing the incompressibility from $K_\infty = 241$ MeV to 218 MeV causes the decrease in the GMR maximum energy from 15 MeV to 13.5 MeV in ^{208}Pb and from 17.5 MeV to 16.5 MeV in ^{124}Sn. On the other side the changing of the effective mass m^* and of the symmetry energy a_{sym} do not change the position of the GMR maximum in both analyzed nuclei.

Figs. 4.4, 4.5 and 4.6 demonstrate also the fact that SV-K parametrizations, especially the SV-bas, give relatively good description of the GMR centroid position and partly also of the shape of the GMR for ^{208}Pb while in the case of ^{124}Sn these parametrizations overestimate in energy the position of the GMR. Taking into account the trend of the GMR position in the dependence on K_∞ shown in

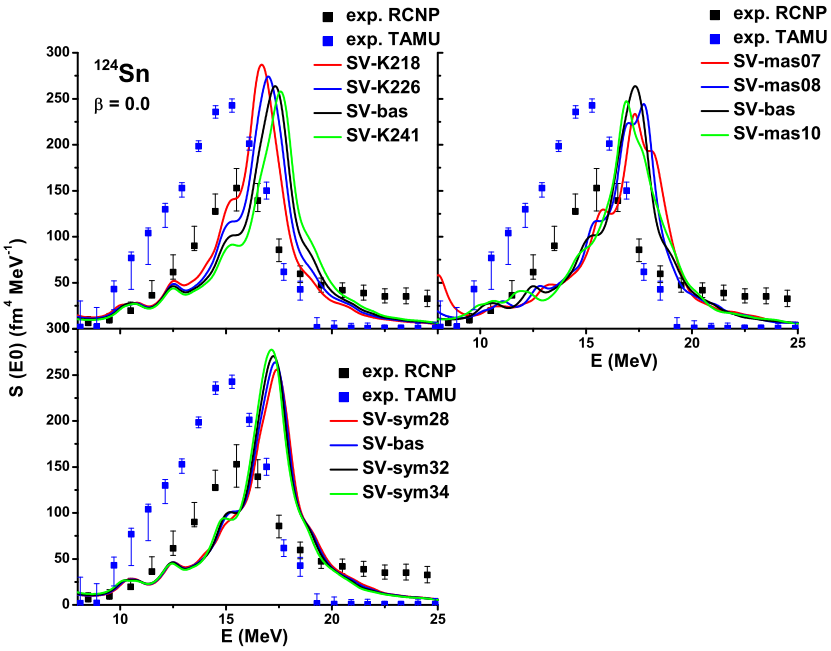

Figure 4.6: Comparison of GMR strength functions for ^{124}Sn for Skyrme parametrizations from SV parametrization set. The input operators used in the SRPA calculations are $\sum r^2 Y_{00}$, $\sum r^4 Y_{00}$, $\sum j_0(0.4z) Y_{00}$, $\sum j_0(0.6z) Y_{00}$. The Lorentz averaging interval is $\Delta = 1$ MeV. The experimental data are taken from TAMU[13] and RCNP[49].

the upper panels of the Fig. 4.4 (decreasing of K_∞ tends to decrease the energy of the GMR) one can expect that the lighter nuclei, like ^{124}Sn, demand the parametrizations with a lower value of K_∞ (around 200 MeV) than $K_\infty = 218$ MeV (the parametrization SV-K218 with the lowest K_∞ in the Figs. 4.4-4.6). This will be discussed also in the next section in the connection with deformed nuclei.

Further we compare E0 strength functions calculated with the BCS+SRPA approach with the available experimental values for other spherical Pb, Sn, and Zr isotopes. At first, for each isotope chain we check if the given isotopes are really spherical. This is done by plotting the total BCS energy as a function of the quadrupole deformation parameter β and the equilibrium deformation corresponds to the position of the minimum of this plot. Then the BCS single-quasiparticle states corresponding to the equilibrium deformation are used for the subsequent SRPA calculation of the E0 strength function. The Skyrme interaction parametrization SV-bas or SLy6 (with the incompressibility modulus K_∞=234 MeV and 230 MeV, respectively) are used for these calculations. Simultaneously we look at the changes of the E0 strength function caused by switching on the surface pairing.

From the Fig. 4.7 we see that all analyzed $^{204-212}$Pb isotopes are spherical for both the SLy6 and SV-bas parametrizations. Since all these Pb isotopes are close to the double-magic ^{208}Pb nucleus, for which the binding energy was used for the fitting of Skyrme interaction parameters, the values of the BCS total energies are relatively close to the experimental values of the binding energy (red dashed horizontal line in the figure).

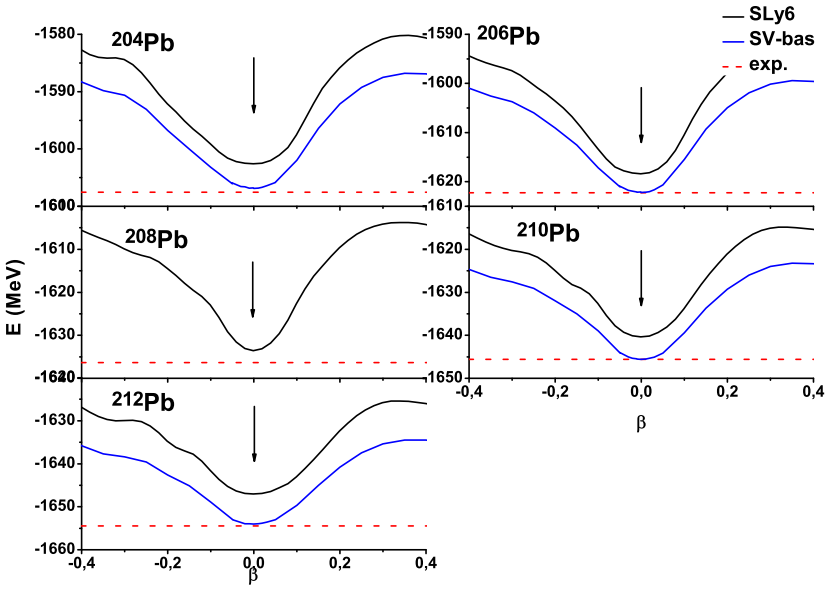

Figure 4.7: Total BCS binding energy as a function of the quadrupole deformation β for SV-bas and SLy6 Skyrme parametrizations. The red horizontal line corresponds to the experimental binding energy obtained from the nucleus mass measurements (taken from [60]). Positions of the minima of the total BCS energies for all studied Pb isotopes correspond to the spherical symmetry ($\beta = 0$) for all these isotopes.

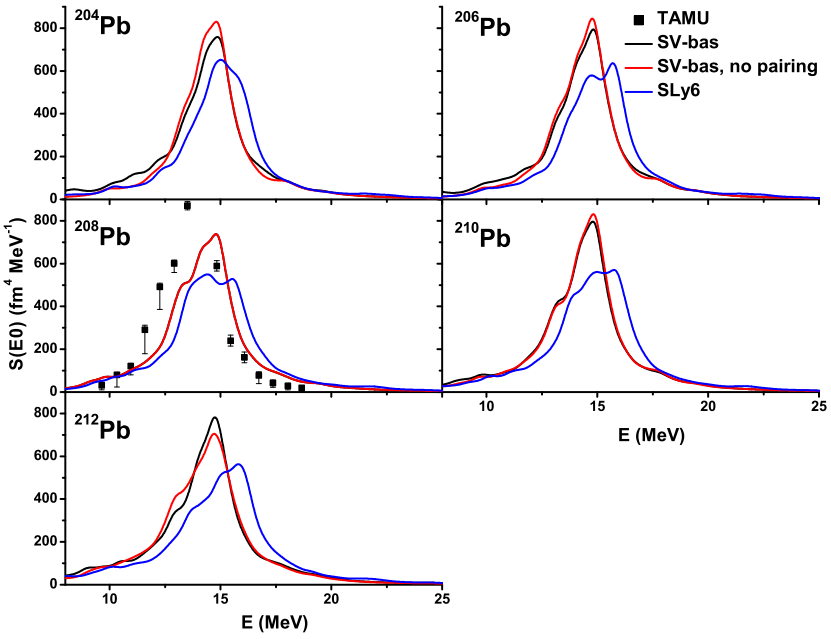

Figure 4.8: GMR strength functions for lead isotopes, for SV-bas parametrization, with/without pairing and SLy6 parametrization.Comparison to the experimental data, which were taken form RCNP[49] and TAMU([13] and [22]) experiments. Deformation for all nuclei was $\beta = 0$, and the Lorentz averaging interval was $\Delta = 1$ MeV. The input operators are $\sum r^2 \mathrm{Y}_{00}$, $\sum r^4 \mathrm{Y}_{00}$, $\sum \mathrm{j}_0(0.4z)\mathrm{Y}_{00}$, $\sum \mathrm{j}_0(0.6z)\mathrm{Y}_{00}$.

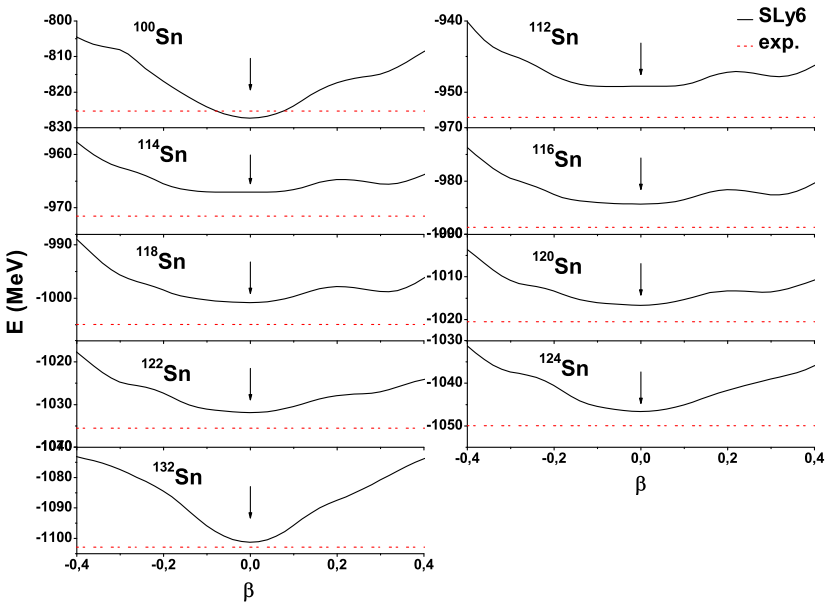

Figure 4.9: The same as in the Fig. 4.7 but for tin isotopes and for the SV-bas parametrization. Experimental data (red dashed lines) of the binding energies was taken from [60]

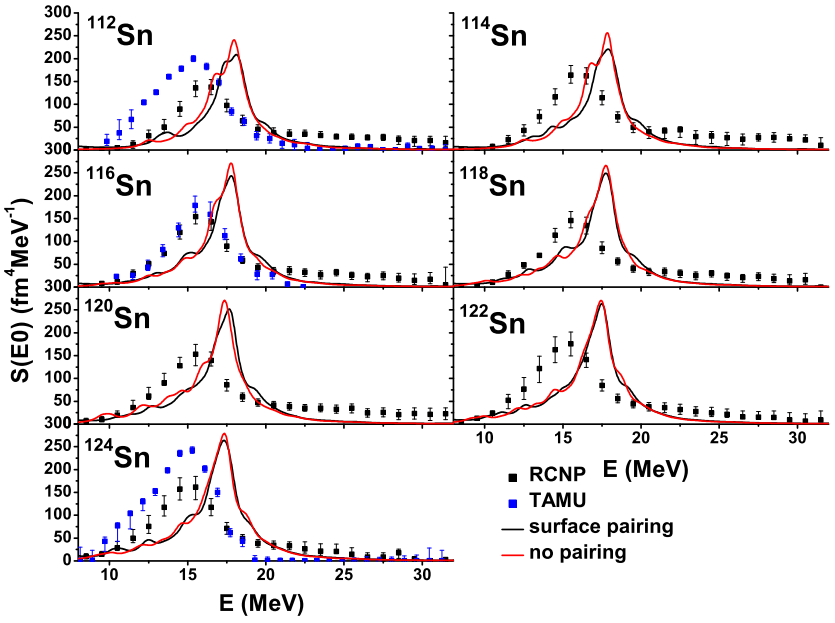

Figure 4.10: The same as in the Fig. 4.8 but for tin isotopes and for the SV-bas parametrization only. Experimental data was taken from RCNP [49] and TAMU [13] and [22] experiments.

Fig. 4.8 shows the E0 strength functions for the chain of the Pb isotopes. The only experimental data are available for ^{208}Pb. The theoretical GMRs slightly overestimate in energy the experimental values but the agreement is quite good. The difference of E0 strength functions calculated with and without the paring is very small.

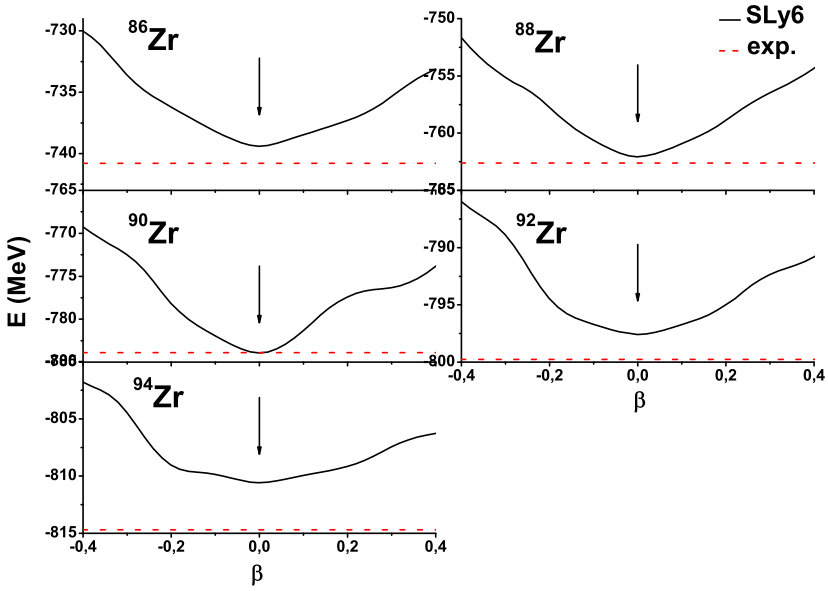

Figure 4.11: Zirconium isotopes, determination of the equilibrium deformation for the SLy6 parametrization, from the binding energy. Comparison with the experimental binding energy[60].

Similar results as those for Pb isotopes were obtained for the chain of Sn isotopes $^{100,-,132}$Sn isotopes as it can be seen from Figs. 4.9 and 4.10. All these isotopes are spherical with $\beta = 0$, as it follows from the Fig. 4.9. However, in some cases the minimum of the total BCS function is quite shallow which indicates the softness of the corresponding isotope. Fig. 4.10 shows the comparison of calculated E0 strength functions with the corresponding experimental TAMU and RCNP data. Unlike the Pb isotope case in the Fig. 4.8, the agreement of calculated E0 strength with the experimental one is worse for Sn isotopes. As it can be seen from the Fig. 4.10 an overestimation of the theoretical GMR with respect to the experimental one in energy is much bigger than in the case of the Pb isotopes. This is in accordance with the trend shown in the Fig. 4.4 that the Skyrme parametrizations with $K_\infty \approx 220 - 230$ MeV do not suit lighter nuclei as Sn isotopes.

Figs. 4.11 and 4.12 show the similar analysis for Zr isotopes. As it can be seen from the Fig. 4.11 all $^{86-94}$Zr isotopes are spherical but there is a shallow minimum of the total BCS energy for ^{94}Zr. The Fig. 4.12 demonstrates E0 strength functions in Zr isotopes. Similarly as in the case of the Sn isotopes one can see quite big overestimation in the energy of the calculated E0 strength function with respect to the experimental ones in ^{90,92,94}Zr isotopes for which only TAMU experimental data exist.

In the Fig. 4.13 there is a comparison of the E0 strength in the spherical ^{144}Sm calculated in the framework of the SRPA and full RPA approaches with

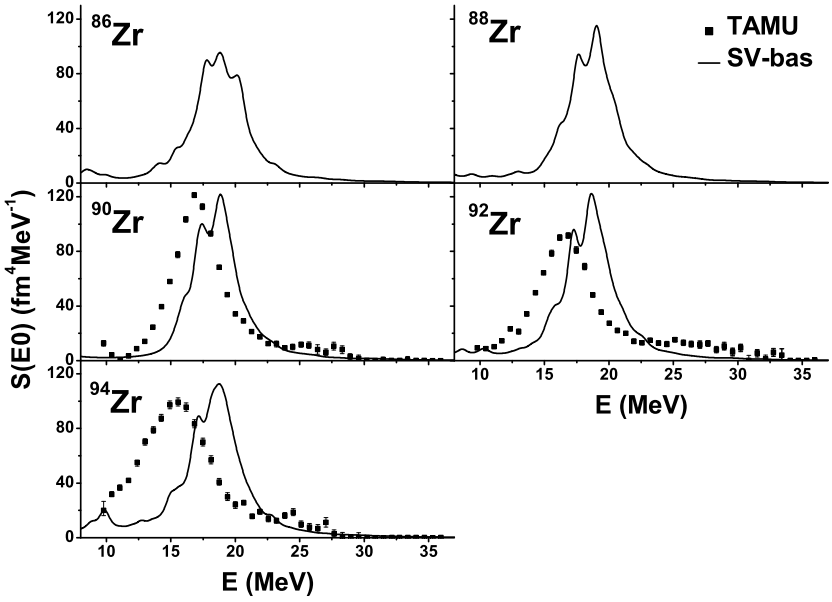

Figure 4.12: Zirconium isotopes, E0 strength function for SV-bas parametrization. Comparison to the available experimental data, which were taken form TAMU[51]. Deformation for all nuclei was $\beta = 0$, and the Lorentz averaging interval was $\Delta = 1$ MeV. The input operators are $\sum r^2 Y_{00}$, $\sum r^4 Y_{00}$, $\sum j_0(0.4z) Y_{00}$, $\sum j_0(0.6z) Y_{00}$

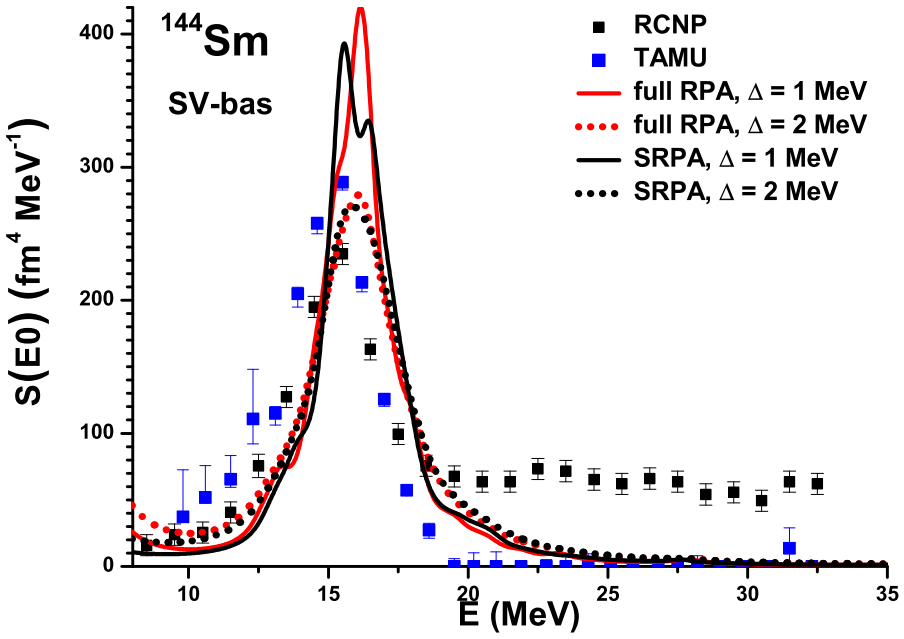

Figure 4.13: E0 strengths for ^{144}Sm for SV-bas parametrization, with surface pairing. Comparison between full RPA and SRPA calculation, and two value of the Lorentz averaging interval $\Delta = 1$ MeV and $\Delta = 2$ MeV. Excitation input operators used in SRPA calculation are: $\sum r^2 Y_{00}$, $\sum r^4 Y_{00}$, $\sum r^2 Y_{20}$, $\sum j_0(0.4z) Y_{00}$, $\sum j_0(0.6z) Y_{00}$. Experimental data are taken from RCNP[12] and TAMU[22].

the corresponding RCNP and TAMU experimental data. The calculation was done with the SV-bas parametrization. The comparison of results obtained with the Lorentz averaging interval $\Delta = 1$ and 2 MeV is done as well. One can see that the SV-bas parametrization gives better agreement of the calculated GMR with the experimental one than in the case of Sn and Zr isotopes. It is again in accordance with the trend given in the Fig. 4.4 that from the point of view of the GMR the Skyrme parametrizations with $K_\infty \approx 220 - 230$ MeV are good for heavier nuclei (like Pb or Sm isotopes). This is contrary to lighter nuclei (like Sn and Zr isotopes) for which parametrizations with the lower values of K_∞ are better.

4.3 Deformed nuclei

In the analysis of the GMR in deformed nuclei we restrict ourselves to three isotope chains: ^{92,96,98,100}Mo, $^{106,-,116}$Cd, and ^{11,148,150,154}Sm. The Mo and Sm chains involve isotopes going from the spherical shape (^{92}Mo and ^{144}Sm) to the well-deformed shape (100Mo and ^{154}Sm). The equilibrium quadrupole deformation β for all above mentioned isotopes was obtained by looking for the minimum of the total BCS energy taken as a function of β for each isotope.

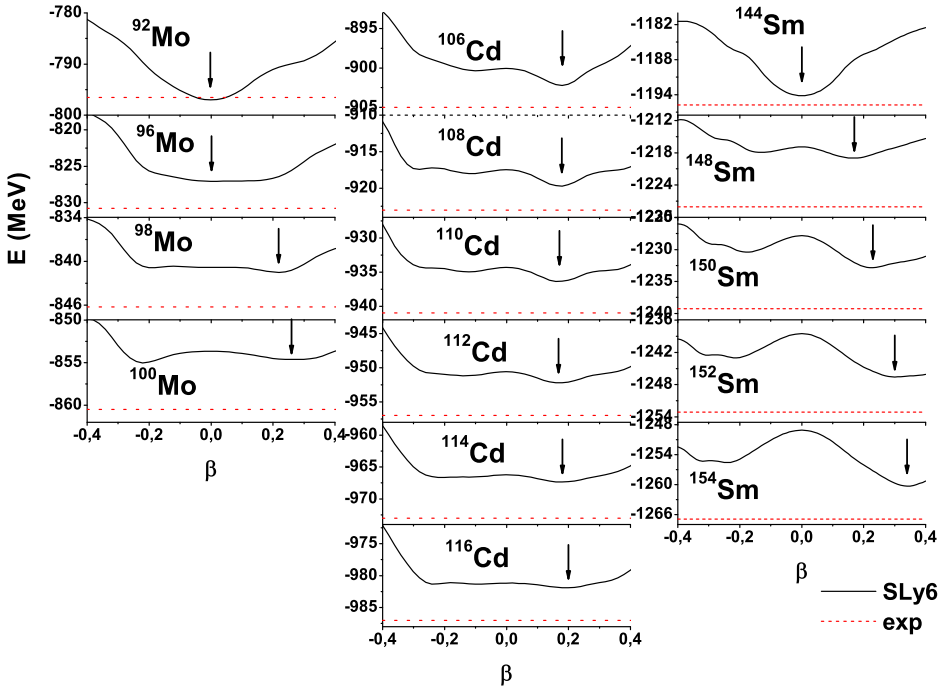

Figure 4.14: Molybdenum, cadmium and samarium isotopes, determination of the equilibrium deformation for the SLy6 parametrization, from the binding energy. Comparison with the experimental binding energy[60].

In the Fig. 4.14 there are dependencies of the total BCS energies on the deformation β for all nuclei involved in the Mo-, Cd-, and Sm- chains, respectively. From this figure one can see for spherical nuclei (^{92}Mo and ^{144}Sm) calculated equilibrium BCS binding energy (the value of the minimum) agrees with the experimental value (corresponding to the red dashed horizontal line). In the case of the nuclei with the nonzero β the agreement is not perfect but we should realize that the Skyrme interaction parameters were obtained by the fitting to binding energies (besides other quantities) of the selected spherical double-magic nuclei. In this fitting procedure no deformed nuclei were involved. Obtained equilibrium deformations were used in the subsequent SRPA calculations for all isotopes mentioned above.

The GMR energy distribution, discussed in the previous section and devoted to the spherical nuclei, was characterized by a one-peak character (in the both theoretical and experimental cases). From theoretical point of view it is well-known that the spherical mean field corresponds to the preserving of the angular momentum for nuclear states. As a result there is not any coupling between excitations with different multipolarities (for instance between E2 and E0 modes).

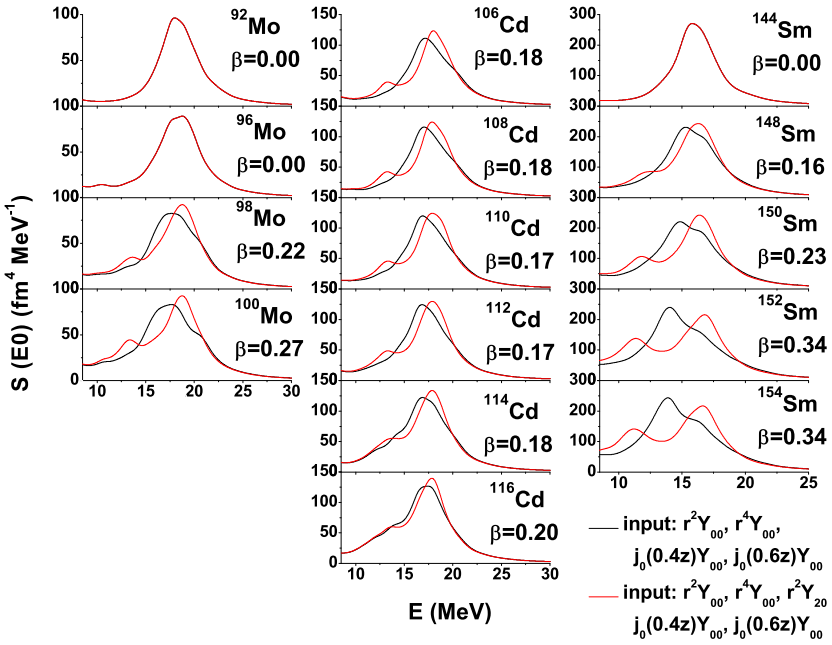

Figure 4.15: Comparison of E0 strength functions for deformed nuclei with or without inclusion of quadrupole input term $\sum r^2 Y_{20}$. The parametrization used was SV-bas, surface pairing, Lorentz averaging interval $\Delta = 2$ MeV.

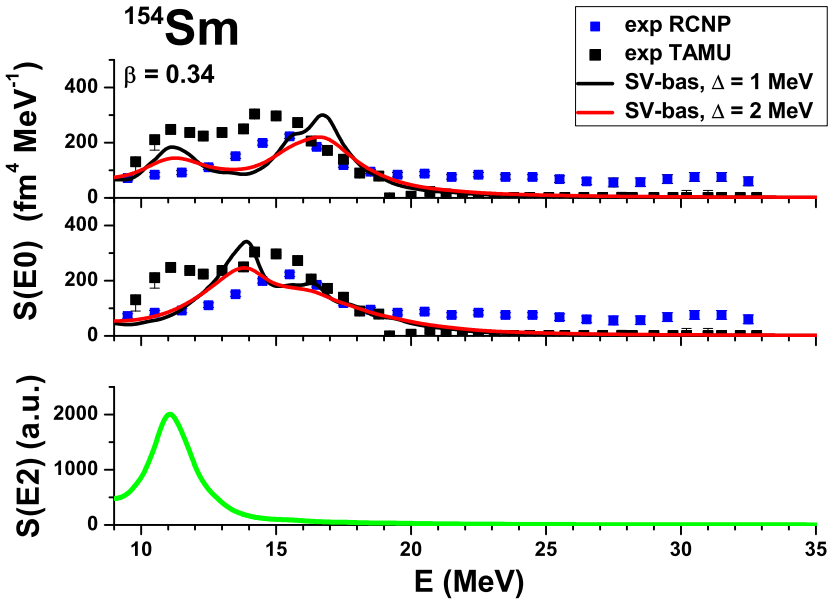

Figure 4.16: Isoscalar E0 (two upper panels) and E2 (bottom panel) strength functions in deformed ^{154}Sm calculated within SRPA for the sets of input operators specified in the panels. The force SV-bas and surface pairing are used. The E0 strength is determined with (upper panel)and without (middle panel) coupling to the quadrupole excitations. The results obtained with the volume and surface pairing as well as with two values of the averaging parameter, Δ=1 and 2 MeV, are compared. The RCNP [12] and TAMU [22] experimental data are shown.

In the case of the axially deformed mean field the intrinsic angular momentum is not a good quantum number for intrinsic nuclear state, only its projection to the symmetry axis is preserved and therefore only the projection is a good quantum number for each intrinsic state. In this case the intrinsic total angular momenta are mixed and it allows to have a coupling between E0 and E2 modes. Since the E0 and E2 isoscalar resonances in the spherical nuclei occur for different energies one can expect that their mixing due to nonzero deformation in deformed nuclei can cause a double peak structure of the GMR (or at least its substantial broadening). This idea was suggested in the paper [29] for the first time but only qualitatively. Further this idea is checked by our SRPA calculations.

The advantage of the special form of the SRPA approach in comparison with the full RPA method is not only in its short computing time but also in our ability to do the analysis of the coupling between different modes (E0 and E2 in our case). We can analyze the influence of the E0-E2 coupling on the GMR simply by the switching on and off the quadrupole operator $\sum r^2 Y_{20}$ in the set of the exciting (input) operators in the SRPA.

In the Fig. 4.15 the effect of the exclusion or inclusion of the quadrupole operator $\sum r^2 Y_{20}$ into the set of the input operators is demonstrated for all above mentioned isotopic chains (for Mo, Cd, and Sm isotopes). In all panels in this figure the black curve corresponds to the situation when the set of the input operators involves only the monopole type operators: $\sum r^2 \mathrm{Y}_{00}$, $\sum r^4 \mathrm{Y}_{00}$, $\sum \mathrm{j}_0(0.4r)\mathrm{Y}_{00}$, $\sum \mathrm{j}_0(0.6r)\mathrm{Y}_{00}$ without any quadrupole type operator. The red curve is connected with the set of input operators involving besides the monopole operators also quadrupole one : $\sum r^2 Y_{20}$. In such a way the red curve corresponds to the case when the E0-E2 coupling is switched on while for the black curve this coupling is switched off. The double peak structure of the red curve is formed more sharply with the increasing deformation. In the spherical case (^{92}Mo and ^{144}Sm) there is only one peak in the GMR structure.

The mechanism of the E0-E2 coupling can be seen well from the Fig. 4.16. In the upper and middle panels the E0 strength function calculated with the SV-bas parametrization for ^{154}Sm is compared with the experimental RCNP and TAMU E0 strength distributions. The red solid curves correspond to the Lorentz averaging parameter $\Delta = 2$ MeV and red dashed curves to $\Delta = 1$ MeV, both (solid and dashed) red curves are connected with the volume pairing, while analogous black lines corresponds to surface pairing. The curves in the upper panel were obtain by the SRPA calculation with five input operators: $\sum r^2 \mathrm{Y}_{00}$, $\sum r^4 \mathrm{Y}_{00}$, $\sum \mathrm{j}_0(0.4r)\mathrm{Y}_{00}$, $\sum \mathrm{j}_0(0.6r)\mathrm{Y}_{00}$, $\sum r^2 \mathrm{j}_{20}$ while for curves in the middle panel only four monopole input operators (without the quadrupole one) were used. The lower panel involves the isoscalar quadrupole E2 strength function with the quadrupole multipolarity projection $K = 0$ obtained by the SRPA calculations with five input operators involving the quadrupole one (the same input operator set as in the upper panel) and with the volume pairing. The double peak structure of the calculated E0 strength can be clearly seen in the upper panel (involving the E0-E2 coupling) while in the middle panel (where the E0-E2 coupling is switched off) one peak character of the E0 strength was obtained. The calculated double peak structure of the E0 strength is in the agreement with the TAMU experiment while the RCNP data provide only one peak. The important fact is that the position of the first peak in the E0 distribution agrees very well

with the position of the E2 (K=0) strength function peak shown in the lower panel. The Fig. 4.16 demonstrates again the negligible effect of the choice of the pairing type (volume or surface) on the calculated E0 strength function.

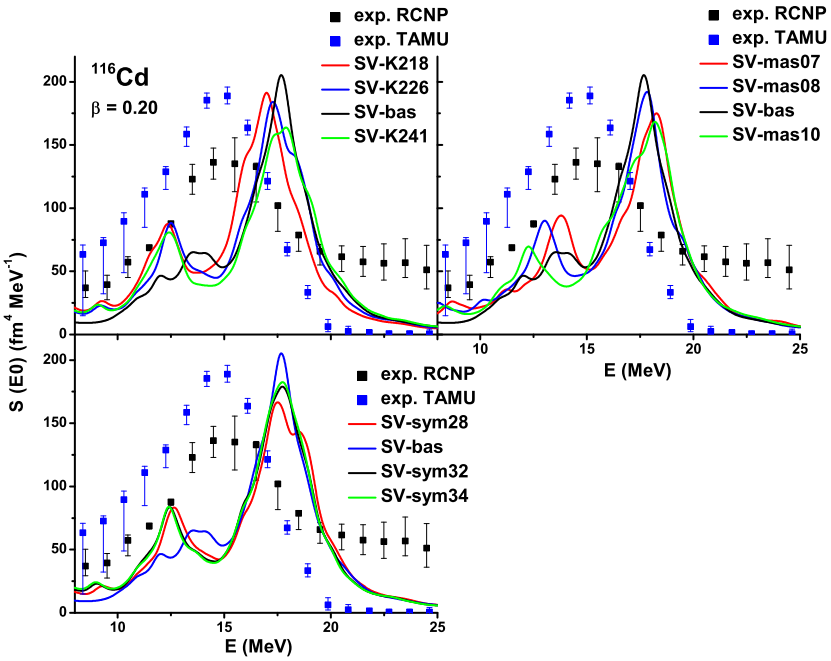

Figure 4.17: Comparison of GMR strength functions for ^{116}Cd for Skyrme parametrizations from SV parametrization set. The input operators used in the SRPA calculations are $\sum r^2 Y_{00}$, $\sum r^4 Y_{00}$, $\sum r^2 Y_{20}$, $\sum j_0(0.4z) Y_{00}$, $\sum j_0(0.6z) Y_{00}$. The Lorentz averaging interval is $\Delta = 1$ MeV. The experimental data are taken from TAMU[50] and RCNP[17].

In the Figs. 4.17 and 4.18 the GMR energy distribution for deformed ^{116}Cd and ^{154}Sm nuclei calculated with the parametrization sets SV-K (with K_∞ = 218, 226, 234, and 241 MeV), SV-mas (with m^*/m = 0.7, 0.8, 0.8, *and* 1.0), and SV-sym (with a_{sym} = 28, 30, 32, *and* 34) are compared with the TAMU and RCNP experimental E0 strength functions. As for the agreement with the experimental values, all theoretical E0 strength functions are shifted to higher energies in the comparison with experimental ones. One can notice a small dependence of the position of the second peak on the incompressibility modulus K_∞ in ^{116}Cd: decreasing of K_∞ from 241 MeV to 218 MeV gives the shift of the position of the second GMR maximum of about 1 MeV to lower energies. However it is not sufficient to reach the position of the experimental E0 strength function maximum. In the heavier ^{154}Sm such dependence on K_∞ is not observed. The position of the first (smaller) E0 strength peak depends on the effective mass in the both ^{116}Cd and ^{154}Sm nuclei: decreasing of m^*/m from 1.0 to 0.7 gives the shift to higher energies by about 1.5 MeV. This is connected with the similar shift of the isoscalar E2 (K=0) strength function because, as we saw in the Fig. 4.16, the position of the first GMR peak is connected with the isoscalar E2 (K=0) peak.

If we compare Figs. 4.17 and 4.18 for deformed nuclei with analogous Figs. 4.5 and 4.6 for spherical nuclei the different trend can be seen. For spherical nuclei the trend is that GMR for heavier nuclei is better reproduced by the Skyrme interaction parametrizations with the higher K_∞ while for lighter nuclei these

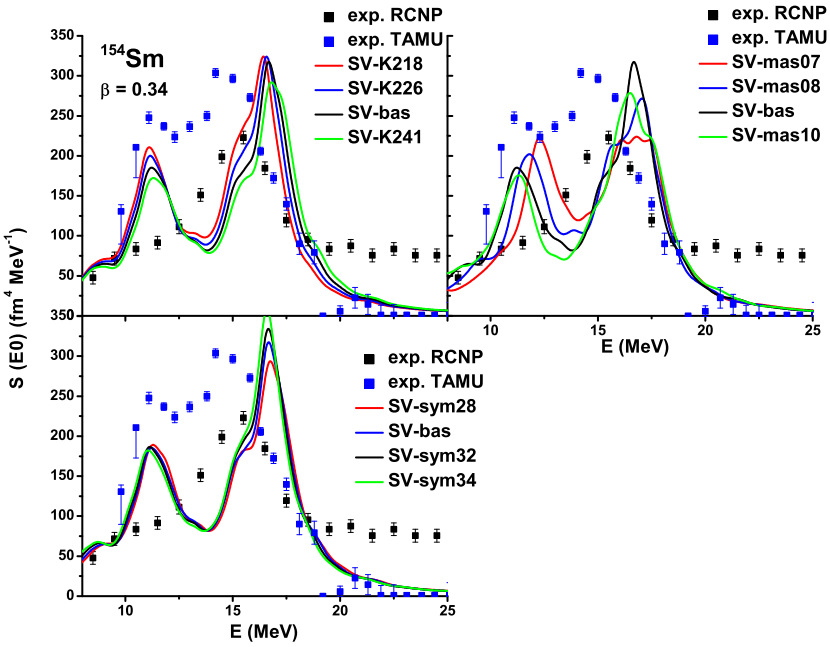

Figure 4.18: Comparison of GMR strength functions for ^{154}Sm for Skyrme parametrizations from SV parametrization set. The input operators used in the SRPA calculations are $\sum r^2 Y_{00}$, $\sum r^4 Y_{00}$, $\sum r^2 Y_{20}$, $\sum j_0(0.4z) Y_{00}$, $\sum j_0(0.6z) Y_{00}$. The Lorentz averaging interval is $\Delta = 1$ MeV. The experimental data are taken from TAMU[22] and RCNP[12].

parametrizations overestimate the peak position. In the deformed nucleus case all SV parametrizations overestimate GMR positions both for heavier and lighter nuclei.

In the figure Fig. 4.19, the results obtained with the force SV-bas are compared with TAMU [22] and RCNP [12] data for the set of Sm isotopes. The equilibrium quadrupole deformations β were determined from the minimum of the nuclear energy (see Fig. 4.14) and show that only ^{144}Sm is spherical while the other isotopes are soft (^{148}Sm) or well deformed ($^{150-154}$Sm. The E0 strength is calculated within the SRPA method with 4 (black curves) or 5 input operators involving the quadrupole one (red curves). It is seen that our calculations clearly demonstrate the broadening of the GMR due to the quadrupole input operator $\sum r^2 Y_{20}$ and the onset of the GMR two-peak structure in going from the spherical ^{144}Sm to the deformed ^{154}Sm. The latter effect is caused by the coupling of E0 and E2 modes in deformed nuclei explained in the Fig. 4.16. Note that the two-peak structure in ^{154} is observed in TAMU [22] but not in RCNP [12] experiments, which once more signals on the essential discrepancy between the two experiments. Further, in contrast to our predictions, the RNCP data do not show any double-peak structure in deformed ^{150,152}Sm. Taking into account the RCNP/TAMU disagreement for ^{154}Sm, the corroboration of the RNCP data for ^{150,152}Sm is desirable.

In the Fig. 4.20 the GMR energy distribution calculated with the Skyrme parametrization SV-bas for Mo isotope chain going from the spherical ^{92}Mo to well deformed ^{100}Mo is compared with the TAMU experimental E0 strength function. Two calculation for Lorentz averaging interval ($\Delta = 1$ and 2 MeV) were done

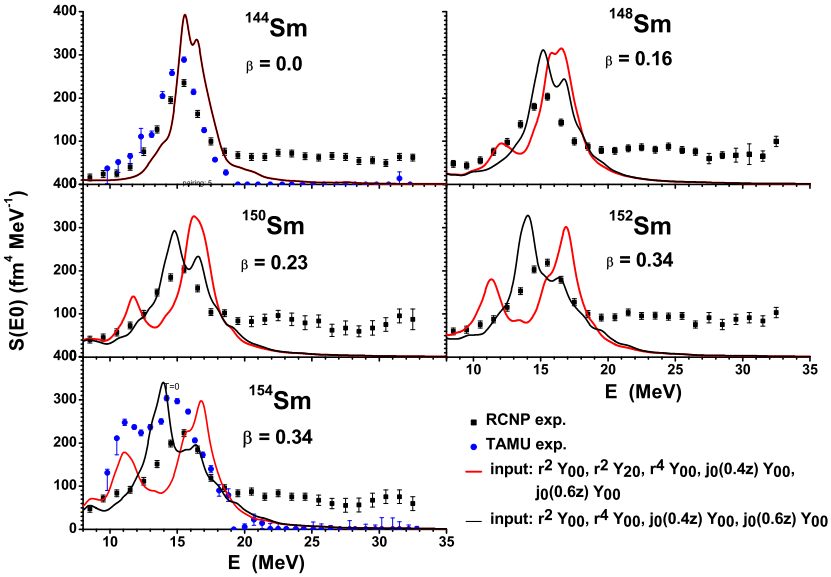

Figure 4.19: E0 strengths for samarium isotopes for SV-bas parametrization. The Lorentz averaging interval is $\Delta = 1$ MeV. Comparison for two sets of input operators: with or without the quadrupole operator $\sum r^2 Y_{20}$. Experimental data are taken from RCNP[12] and TAMU[22].

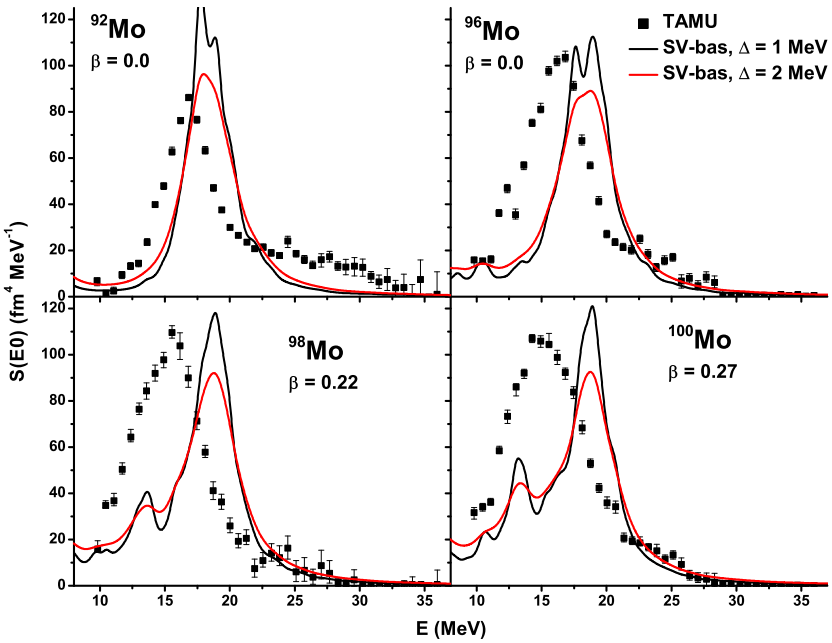

Figure 4.20: E0 strengths for molybdenum isotopes for SV-bas parametrization. Comparison between different values of the Lorentz averaging interval $\Delta = 1$ MeV and $\Delta = 2$ MeV. Excitation input operators used are: $\sum r^2 \mathrm{Y}_{00}$, $\sum r^4 \mathrm{Y}_{00}$, $\sum r^2 \mathrm{Y}_{20}$, $\sum \mathrm{j}_0(0.4z)\mathrm{Y}_{00}$, $\sum \mathrm{j}_0(0.6z)\mathrm{Y}_{00}$. The Lorentz averaging interval is $\Delta = 1$ MeV. Experimental data are taken from TAMU[51].

for each nucleus. In the well deformed ^{100}Mo the double peak structure obtained in the theoretical calculation is not observed in the experiment. Nevertheless one can see the broadening of the experimental GMR in the deformed ^{100}Mo with respect to the spherical ^{92}Mo. In the case of the Mo chain one should bear in mind also the known fact that nuclei ^{96,98}Mo are transitional soft nuclei with a possible quadrupole triaxiality γ (see [61]) and their description by one axial quadrupole deformation β is only an approximation.

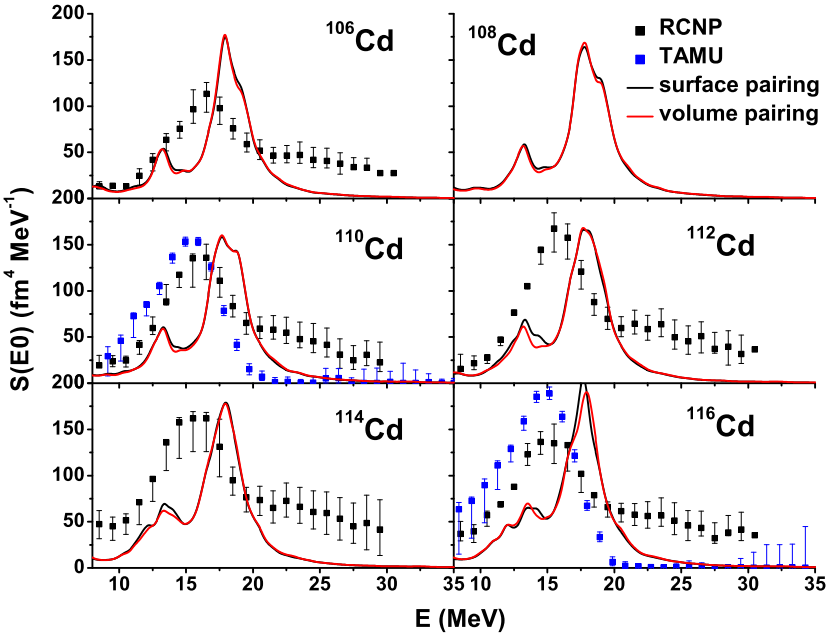

Figure 4.21: E0 strengths for cadmium isotopes for SV-bas parametrization, with volume or surface pairing. Excitation input operators used are: $\sum r^2 Y_{00}$, $\sum r^4 Y_{00}$, $\sum r^2 Y_{20}$, $\sum j_0(0.4z) Y_{00}$, $\sum j_0(0.6z) Y_{00}$. The Lorentz averaging interval is $\Delta = 1$ MeV. Experimental data are taken from RCNP[17] and TAMU[50].

Chain of cadmium ^{106}Cd – ^{116}Cd offers other axially symmetric nuclei. The comparison of E0 strength functions with available TAMU[50] and RCNP[17] data are in the Fig. 4.21. We can see that cadmium isotopes, like tin isotopes, are softer than lead. Although cadmium nuclei are deformed, and in our strength function we can observe typical double-peak structure of the resonance, in the experimental results from both experiments, there is present only slight widening of the main peak.

Conclusion

The systematic study of the isoscalar giant monopole resonances (GMR) in spherical and deformed nuclei has been performed within the self-consistent separable Skyrme RPA (SRPA) approach. The analysis was based not only on the comparison of calculated and experimental GMR centroids, as it was performed practically in all up to date papers, but the shape of the GMR (its energy distribution) was involved in our analysis as well.

The main result of this thesis concerns the double peak structure of the GMR in deformed nuclei. The prediction of it, given in the eighties in the paper [29], was based only on the simple phenomenological considerations. In contrast, we analyzed the GMR using the microscopic model. The self-consistent SRPA approach, used in the thesis, gives an especially good possibility to demonstrate the mechanism of the formation of the double peak structure of the GMR as we go from the spherical to deformed nuclei simply by the switching on (or switching off) the E0-E2 coupling as a result of the inclusion (or not inclusion) of the quadrupole E2 operator into the set of the external exciting operators (see Figs. 4.15, 4.16). It was shown in this way that the double peak structure of the GMR in deformed nuclei is a deformation effect connected with the coupling of electric monopole E0 and quadrupole E2 modes which is allowed only in the deformed systems.

For both spherical and deformed nuclei analyzed in this thesis the Skyrme interaction parametrizations with smaller value of the incompressibility modulus K_∞ give a lower position of the GMR in the spectrum (see Fig. 4.4). In the heavier spherical nuclei, like ^{208}Pb (see Fig. 4.8) or ^{144}Sm (see Fig. 4.13), the Skyrme parametrizations with $K_\infty \approx 230$ MeV (e.g. SV-bas or SLy6) give more or less a good position of the calculated GMR in the comparison with experiments and the parametrizations with a lower value of K_∞ give a very small GMR shift in the energy. In the case of lighter spherical nuclei, like Sn (see Fig. 4.6) or Zr (see Fig. 4.12) isotopes, the calculated GMRs are shifted by ≈ 3 MeV to the higher energies with respect to the experimental values and the use of parametrizations with lower values of K_∞ (e.g. SV-mass218 with $K_\infty = 118$ MeV or SkP$^\delta$ with $K_\infty = 202$ MeV) does not help to obtain an agreement with experiments. In the case of deformed nuclei the situation is more complicated because available experimental data from TAMU and RCNP experiments do not agree with each other (see Fig. 4.19 for ^{154}Sm). Therefore, not only theoretical GMR but also experimental data are under the question. The TAMU experimental energy GMR distribution shows a clear double peak structure which is confirmed by our calculation (see Fig. 4.19 for ^{154}Sm). However, such a clear double peak structure is not observed in either ^{154}Sm or other deformed nuclei in RCNP experiments and we can in the data recognize only broadening of the single GMR peak. Our calculations give double peak structure of GMR in all deformed nuclei with deformations $\beta > 0.2$ (see Fig. 4.15) and substantial broadening of GMR peak for $\beta > 0.1$. In this sense our calculations are in the qualitative agreement with the shape of GMR in available experiments. However, the calculated GMR for all Skyrme parametrizations overestimate GMR energies in the comparison with experimental data by about 2-3 MeV in deformed nuclei (see Figs. 4.16-4.20).

In order to do more reliable comparison with experimental data more experiments providing information on GMR in spherical and particularly in deformed nuclei are desirable. From the point of view of the theory it is a question if the Skyrme effective interaction with all its nowadays parametrizations can give more precise agreement with all details of experimental data on GMR in spherical and deformed nuclei. Analyses of the GMR with other effective nucleon-nucleon interactions are desirable as well.

Bibliography

[1] Nesterenko, V. O., Kvasil, J., Reinhard, P.-G., *Phys. Rev. C66*, 044307 (2002).

[2] Nesterenko, V. O., Kleinig, W., Kvasil, J., Veselý, P., Reinhard, P.-G., *Phys. Rev. C74*, 064306 (2006).

[3] Veselý, P., Kvasil, J., Nesterenko, V. O., Kleinig, W., Reinhard, P.-G., Ponomarev, V. Yu., *Phys. Rev. C80*, 313012 (2009).

[4] Repko, A., Reinhard, P.-G., Nesterenko, V.O., Kvasil, J., *Phys. Rev. C87*, 024305 (2013).

[5] Kvasil, J., Nesterenko, V. O., Kleinig, W., Božík, D., Reinhard, P.-G., Ponoamrev, V. Yu., *Eur. Phys. J. A49*, 119 (2013).

[6] Colo, G., *Phys. Part. Nucl. 39*, 286 (2008).

[7] Avogadro, P., Bertulani, C. A., *Phys. Rev. C88*, 044319 (2013).

[8] Uchida, M., et al., *Phys. Rev. C69*, 051301(R) (2004).

[9] Blaizot, J. P., *Phys. Rep. 64*, 171 (1980).

[10] Niksic, T., Vretenar, D., Ring, P., *Phys. Rev. C78*, 034318 (2008).

[11] Youngblood, D. H., Clark, H. L., Lui, Y.-W., *Phys. Rev. Letters 82(4)*, 691 (1999).

[12] Itoh, M., et al., *Phys. Rev. C68*, 064602 (2003).

[13] Lui, Y.-W., Youngblood, D. H., Tokimoto, Y.,Clark, H. L., John, B. *Phys. Rev. C70*, 014307 (2004).

[14] Li, M., et al., *Phys. Rev. letters 99*, 162503 (2007).

[15] Li, M., et al., *Phys. Rev. letters 81*, 034309 (2010).

[16] Li, M., et al., *Phys. Rev. letters 99*, 162503 (2012).

[17] Patel, A., et al., *Phys. Let. B718*, 447-450 (2012).

[18] Li-Gang Cao, Sagawa, H., Colo, G. *Phys. Rev. C86*, 054313 (2012).

[19] Veselý, P., Toivanen, J., Carlsson, B. C.,Dobaczewski, J., Michel, M., Pastore, D., *Phys. Rev. C86*, 024303 (2012).

[20] Colo, G., Giai, N.V., Meyer, J.,Bennaceur, K., Bonche, P., *Phys. Rev. C70*, 024307 (2004).

[21] Khan, E., *Phys. Rev. C80*, 011307(R) (2009).

[22] Youngblood, D. H., et al., *Phys. Rev. C69*, 034315 (2004).

[23] Kvasil, J.,Bozik, D., Repko, A., Nesterenko, V. O., Reinhard, P.-G., Nesterenko, V.O., arXiv: 1407.3108[nucl-th] (2014), accepted in Physica Scripta.

[24] Youngblood, D. H., et al., *Phys. Rev. C88*, 051301(R) (2013).

[25] Kishimoto, T., et al., *Phys. Rev. Lett. 35*, 552 (1975).

[26] Zawischa, D., Speth, J., Pal, D., *Nucl. Phys. A311*, 445 (1978).

[27] Abgrall, Y., Morand, B., Caurier, E., Grammaticos, N., *Nucl. Phys. A346*, 731 (1980).

[28] Buender, T., et al., *Phys. Rev. Lett. 45*, 1667 (1980).

[29] Garg, U., et al., *Phys. Rev. C29*, 93 (1984).

[30] Ring, P., Schuck, P., *The Nuclear Many-Body Problem*, Springer-Verlag New York (1980).

[31] Skyrme, T. H. R., *Nucl. Phys. 9*, 615 (1959).

[32] Vautherin, D., Brink, D. M., *Phys. Rev. C5*, 626 (1972).

[33] Decharge, J., Gogny, D., *Phys. Rev. C21*, 1640 (1970).

[34] Vretenar, D., Afanasjev, A. V., Salazissis, G. A., Ring, P., *Phys. Rep. 409,* 101 (2005).

[35] Stone, J. R., Reinhard, P.-G., *Progr. Part. Nuc. Phys. 58*, 587 (2007).

[36] Kl upfel, P., Reinhard, P.-G., Burvenich, T.J., Maruhn, J., *Phys. Rev. C79*, 034310 (2009).

[37] Dobaczewski, J., Flocard, H., Treiner, J., *Nucl. Phys. A 422*, 103 (1984).

[38] Hohenberg, P., Kohn, W., *Phys. Rev. 136*, B864 (1964).

[39] Kohn, W., Sham, L. J., *Phys. Rev. 140*, A1133 (1965).

[40] Lipparini, E., Stringari, S., *Nucl. Phys. A371*, 430 (1981).

[41] Kvasil, J., LoIudice, N., Nesterenko, V. O., Kopal, M. *Phys. Rev. C58*, 209 (1998).

[42] Vesely, P., *Doctoral thesis*, Faculty of Mathematics and Physics, Charles University (2009).

[43] Lipparini, E., Stringari, S., *Phys. Rep. 175* No3+4, 103 (1989).

[44] Bohigas, O., Lane, A. M., Martonell, J., *Phys. Rep. 51*, 267 (1979).

[45] Kvasil, J.,Nesterenko, V. O., Repko, A., Bozik, D., Kleinig, W., Reinhard, P.-G., *Journal of Physics: Conference Series 580*, 012053 (2015).

[46] Kvasil, J.,Bozik, D., Nesterenko, V.O., Reinhard, P.-G., Kleinig, W., submitted to Phys. Rev.

[47] Weintz, C.,Uberall, H., *Phys. Rev. 149*, 762 (1966).

[48] Harakeh, M. N., van der Woude, A., *Giant Resonances*, Clarendon Press Oxford (2001).

[49] Li, T., Garg, U., *Phys. Rev. C81*, 034309 (2010).

[50] Lui, Y.-W., Youngblood, D. H., *Phys. Rev. C69*, 034611 (2004).

[51] Youngblood, D. H., et al., *Phys. Rev. C88*, 021301 (2013).

[52] Youngblood, D. H., Lui, Y.-W., *Phys. Rev. C69*, 034315 (2004).

[53] Soloviev, V.G., Theory of Atomic Nuclei; Quasiparticle and Phonons, Institute of Physics, Bristol, (1992)

[54] Kvasil, J., Nesterenko, V.O., Kleinig, W., Bozik, D., Reinhard, P.-G., *Int. Journal of Mod. Phys. E 20*, 281 (2011).

[55] Nguyen van Giai, Sagawa, H., *Physics Letters 106B*, 379-382 (1981).

[56] Reinhard, P.-G., Flocard, H., *Nuclear Physics A584*, 467-488 (1995).

[57] Bartel, J., Quentin, P., *Nuclear Physics A386*, 79-100 (1982).

[58] Tondeur, F., Brack, M., *Nuclear Physics A420*, 297-319 (1984).

[59] Chabanat, E., Bonche, P., *Nuclear Physics A635*, 231-256 (1998).

[60] National Nuclear Data Center, accessed throughout 2014, available from: http://www.nndc.bnl.gov/.

[61] Rusev, U., et al., *Phys. Rev. C 73*, 044308 (2006).